CERN-THESIS-2006-141

University of Neuchâtel
Physics Department

# Study of $\nu$ interactions and background estimation in the OPERA Emulsion Film Detector

Thesis by
József Janicskó-Csáthy

Thesis Presented in Partial Fullfilement of the
Requirements for the Degree of
Doctor és Sciences

In presence of a jury composed by:
Prof. J.-L. Vuilleumier, thesis advisor, Neuchâtel
Prof. J.P. Derendinger, Neuchâtel
Prof. D. Twerenbold, Neuchâtel
Prof. A. Ereditato, Berne
Dr. F. Juget, Neuchâtel

Neuchâtel, June 2006

Université de Neuchâtel

# IMPRIMATUR POUR LA THESE

# Study of ν interactions and background estimation in the OPERA emulsion film detector


## Jozsef JANICSKO-CSATHY

UNIVERSITE DE NEUCHATEL

FACULTE DES SCIENCES


La Faculté des sciences de l'Université de Neuchâtel,
sur le rapport des membres du jury

MM. J.-L. Vuilleumier (directeur de thèse), J.-P. Derendinger,
D. Twerenbold, A. Eredidato (Berne)
et F. Juget

autorise l'impression de la présente thèse.

Neuchâtel, le 24 août 2006

UNIVERSITE DE NEUCHATEL
FACULTE DES SCIENCES
Secrétariat-décanat de la faculté
Rue Emile-Argand 11 - CP 158
CH-2009 Neuchâtel

Le doyen :

J.-P. Derendinger


■ Faculté des Sciences
■ Rue Emile-Argand 11 ■ CP 158 ■ CH-2009 Neuchâtel
■ Téléphone : +41 32 718 21 00 ■ Fax : +41 32 718 21 03 ■ E-mail : secretariat.sciences@unine.ch ■ www.unine.ch

# Contents

# Introduction

During the 20th century mankind achieved more than ever before in understanding the laws and mastering the forces of nature. One of the still open questions that continue to push forward the frontiers of the science, is the nature of an elusive particle called neutrino.

In the last decade neutrino physics made an impressive progress, important experimental results were published and theories seem to be confirmed. Today, we think that neutrinos are massive particles and they can oscillate from one flavor to another. The theory of neutrino oscillations seems to be proven, with only a few parameters missing. One of the important experiments that hopefully will provide the still missing parameters is the OPERA experiment.

Following the results published by the Super Kamiokande collaboration, became clear that $\nu_\mu$ neutrinos oscillate into some other flavor. The aim of the OPERA experiment is to provide direct evidence of the $\nu_\mu \rightarrow \nu_\tau$ oscillation.

OPERA is a hybrid detector, comprising electronic detectors and nuclear emulsions with an impressive target mass of 1.8 kt. Located at the Gran Sasso Underground Laboratory, will start taking data during the year 2006. It will detect $\nu_\tau$ neutrinos in the $\nu_\mu$ beam produced at CERN, 732 km away from the detector.

The detection of $\nu_\tau$ is based on the observation of the decay of the $\tau$ lepton. The fine grained structure of nuclear emulsions offers the possibility to directly observe such a decay and by the means of kinematical analysis can be clearly separated from background events. Nuclear emulsions will be produced and processed in industrial quantities and the readout will be done with automatized optical microscopes.

In this work are presented some of the analysis tools needed for the data analysis starting with the raw data produced by the scanning stations. An estimation of the background for the $\tau \rightarrow \mu + \nu_\mu + \nu_\tau$ and $\tau \rightarrow h + \nu_\tau$ decay channels and an estimate of detection efficiency for the hadronic decay channels are given. In the last chapter experimental results from test-beam data are presented.

# Chapter 1

# The Physics of Neutrinos

## 1.1 History

The history of neutrino physics starts with the first investigations on the structure of the atomic nucleus dating back in the early 20th century. A detailed history is given in many monographs and introductory particle physics books ([1, 2]). Here I will give only a short summary of the most important developments.

The discovery of the continuous spectrum beta rays by Chadwick (1914) posed serious interpretation problems. After considering all explanations, even theories involving the violation of the energy conservation principle, finally, it was Wolfgang Pauli who suggested the existence of a new neutral particle which he called "neutron". Pauli assumed that the new particle should be a spin 1/2, light (about 1 electron mass) and neutral. After the discovery of the neutron in 1932 by Chadwick the name "neutrino" was suggested by Fermi for Pauli's particle.

However, the direct detection of neutrinos was still not possible for a long time. The first direct detection of free neutrinos was performed in 1956 by Reines and Cowan at the Savannah River nuclear reactor.

In the 1960's the question of different neutrino flavors was raised and the first neutrino-beam experiment at Brookhaven (1962) showed that electron neutrinos and muon neutrinos are different. The $\tau$ lepton was discovered at SLAC in 1978 and it was straightforward to assume the existence of a third neutrino, namely the $\tau$ neutrino. While reactor, solar neutrino and neutrino beam experiments successfully detected a high number of $\nu_e$, $\nu_\mu$ interactions, the observation of the $\tau$ neutrino is less obvious. Until now the DONUT experiment found only 4 $\nu_\tau$ candidates ([13]).

For a while, neutrinos were supposed to be massless and they were successfully added to the Standard Model of Particle Physics as massless particles. Direct measurements of the neutrino mass have not find positive evidence (except one) of a finite mass, they only set upper limits, limit that today is acceptedly a few electron-Volt. However the first solar neutrino experiment in the Homestake mine (U.S.) showed a deficit in the number of neutrinos detected, which was confirmed by many other ex-

periments. This gave birth to the theory of neutrino oscillations (Pontecorvo) which implies a nonzero neutrino mass. At the beginning of the 21st century important milestones were achieved: the results of Super-Kamiokande and SNO experiments were published, two important experiments that can help to solve the puzzle.

Super-Kamiokande showed that there is a difference in the number of atmospheric neutrinos coming from above and from the opposite side of the globe, the most plausible explanation being that they appear as some other flavor neutrinos which are not detected in the experiment. In 2002 the results of the SNO experiment showed that the missing electron neutrinos coming from the sun appear as a different flavor since the total number of neutrino interactions is close to the expected one.

The fact that neutrinos oscillate implies nonzero mass. Therefore neutrino physics points beyond the Standard Model which makes neutrinos a hot topic even today, with a great discovery potential.

## 1.2 Helicity, Standard Model

Neutrinos were postulated as spin 1/2 particles to satisfy angular momentum conservation in beta decay. If they are fermions, they can be described with a 4-component Dirac-spinor which satisfies the Dirac equation:

$$(i\gamma^\mu \partial_\mu - m)\psi = 0$$

The solution of the equation is of the form: $\psi(x^\mu) = u(\vec{p})e^{-ipx}$. In Weyl representation (see for example [5]) we write the $u(\vec{p})$ as two 2-component spinor.

$$u(\vec{p}) = \begin{pmatrix} \phi \\ \chi \end{pmatrix}$$

The Dirac equation becomes:

$$\begin{aligned} (\gamma^0 p_0 + \gamma^k p_k - m)u(\vec{p}) &= 0 \\ \begin{pmatrix} -m & p_0 - \vec{\sigma}\vec{p} \\ p_0 + \vec{\sigma}\vec{p} & -m \end{pmatrix} \begin{pmatrix} \phi \\ \chi \end{pmatrix} &= 0 \end{aligned}$$

or:

$$\begin{cases} -m\phi + (p_0 - \vec{\sigma}\vec{p})\chi = 0 \\ (p_0 + \vec{\sigma}\vec{p})\phi - m\chi = 0 \end{cases}$$

If neutrinos are massless ($m = 0$) these two equations decouple: (or in the ultra-relativistic case $m \ll E$)

$$\begin{cases} (p_0 - \vec{\sigma}\vec{p})\chi = 0 \\ (p_0 + \vec{\sigma}\vec{p})\phi = 0 \end{cases}$$

$$\begin{cases} \chi = \left(+\frac{\vec{\sigma}\vec{p}}{p_0}\right)\chi \\ \phi = \left(-\frac{\vec{\sigma}\vec{p}}{p_0}\right)\phi \end{cases}$$

We recognize in these equations the helicity operator:

$$h \equiv \frac{\vec{\Sigma}\vec{p}}{|\vec{p}|} = \begin{pmatrix} \frac{\vec{\sigma}\vec{p}}{|\vec{p}|} & 0 \\ 0 & \frac{\vec{\sigma}\vec{p}}{|\vec{p}|} \end{pmatrix}$$

We distinguish two cases:

1. When $p_0 > 0$:
$$\phi = \left(-\frac{\vec{\sigma}\vec{p}}{p_0}\right)\phi = -\left(\frac{\vec{\sigma}\vec{p}}{|\vec{p}|}\right)\phi$$
$\phi$ describes a left handed neutrino

2. When $p_0 < 0$:
$$\phi = \left(-\frac{\vec{\sigma}\vec{p}}{p_0}\right)\phi = +\left(\frac{\vec{\sigma}\vec{p}}{|\vec{p}|}\right)\phi$$
since the energy is negative, $\phi$ describes the antiparticle of the neutrino and it is right-handed.

Similarly for $\chi$ we get a right-handed neutrino and a left-handed antineutrino. We can conclude that if neutrinos are massless we find two types of states decoupled from each other which describe:

1. left handed neutrino $\nu_L$ and right handed antineutrino $\bar{\nu}_R$
2. right handed neutrino $\nu_R$ and left handed antineutrino $\bar{\nu}_L$

Here we introduced the notation $\nu_{L,R}$ which are the eigenstates of the chirality operator $P_{L,R} = \frac{1}{2}(1 \mp \gamma_5)$. Chirality and helicity eigenstates are the same if the mass is zero.

If the neutrino has a nonzero mass (but small with respect to $E$) the situation is slightly different: both states will contain left- and right-handed components:

$$\phi = \begin{cases} \nu_L + \mathcal{O}\left(\frac{m}{E}\right)\nu_R & (E > 0) \\ \bar{\nu}_R + \mathcal{O}\left(\frac{m}{E}\right)\bar{\nu}_L & (E < 0) \end{cases}$$

One can see that the right-handed component is largely suppressed by the smallness of the $m/E$ ratio. So, even if neutrinos have very small, but nonzero mass, detecting a right-handed neutrino in an experiment is very unlikely. Indeed, experiments showed that parity is not conserved in $\beta$ decay. Wu in 1957 showed that in $\beta$ decay of $^{60}$Co either left-handed electrons or right-handed positrons are emitted. In an other experiment Goldhaber (1958) showed that neutrinos emitted after $^{152}$Eu electron capture are left-handed.

## 1.3 Neutrino masses

In the Standard Model neutrinos are massless. Also in the previous section, we assumed that neutrinos have no mass. However, since the first solar neutrino experiments we suspect that something is wrong with this model. Since then more evidence of nonzero mass was collected. Neutrino masses are consistent with flavor oscillations which we will discus in the next section.

### 1.3.1 Dirac mass term

In the Standard Model the Higgs mechanism generates the Dirac mass term:

$$\mathcal{L}^D = -m_D \bar{\nu}\nu = -m_D(\bar{\nu}_R\nu_L + \bar{\nu}_L\nu_R) \tag{1.1}$$

with $m_D = \lambda v/\sqrt{2}$, where $\lambda$ is the dimensionless Yukawa coupling coefficient and $v/\sqrt{2}$ is the vacuum expectation value of the Higgs field. $\nu_L$ and $\nu_R$ are the chiral left- and right-handed components of the neutrino field.

One can notice that the addition of the Dirac mass term is not compatible with the assumption that right-handed neutrinos do not exist. A nonzero mass automatically involves the existence of both right- and left-handed neutrinos.

The generation of Dirac neutrino masses through the Higgs mechanism is not able to explain why the neutrinos are five order of magnitude lighter than the electron.

### 1.3.2 Majorana mass term

According to Majorana (1937) a massive neutral fermion like the neutrino can be described by a spinor with only two independent components imposing the so-called Majorana condition:

$$\psi = \psi^c \tag{1.2}$$

In other words there is no difference between the particle and its own anti-particle. Decomposing the field in right- and left-handed projections we can write:

$$\psi_L + \psi_R = \psi_L^c + \psi_R^c$$

Acting with the projection operator $P_R$ on both sides of the equation we have:

$$\psi_R = \psi_L^c \tag{1.3}$$

which shows that the right handed component of the Majorana field is not independent from the left-handed one, but one can obtain one from the other with charge conjugation. The Majorana field can be written as:

$$\psi = \psi_L + \psi_L^c$$

This field depends only on the two independent components of $\psi_L$. Similar to the Dirac mass term we can construct the Majorana mass term simply substituting 1.3 into 1.1:

$$\mathcal{L}^M = -\frac{1}{2} m_M (\bar{\psi_L^c}\psi_L + \bar{\psi_L}\psi_L^c) \tag{1.4}$$

### 1.3.3 Dirac-Majorana mass term

If both left-handed and right-handed fields exist and are independent, also the Majorana mass terms for $\nu_L$ and $\nu_R$ are allowed, in addition to the Dirac mass term:

$$\mathcal{L}_L^M = -\frac{1}{2} m_L (\overline{\nu_L^c}\nu_L + \overline{\nu_L}\nu_L^c), \quad \mathcal{L}_R^M = -\frac{1}{2} m_R (\overline{\nu_R^c}\nu_R + \overline{\nu_R}\nu_R^c)$$

The total Dirac + Majorana mass term

$$\mathcal{L}^{D+M} = \mathcal{L}^D + \mathcal{L}_L^M + \mathcal{L}_R^M$$

can be written as:

$$\begin{aligned} \mathcal{L}^{D+M} &= -\frac{1}{2} \begin{pmatrix} \overline{\nu_L^c} & \overline{\nu_R} \end{pmatrix} \begin{pmatrix} m_L & m_D \\ m_D & m_R \end{pmatrix} \begin{pmatrix} \nu_L \\ \nu_R^c \end{pmatrix} + H.c. \\ &= \frac{1}{2} \overline{N_L^c} M N_L + H.c. \end{aligned}$$

with the matrices

$$M = \begin{pmatrix} m_L & m_D \\ m_D & m_R \end{pmatrix}, \qquad N_L = \begin{pmatrix} \nu_L \\ \nu_R^c \end{pmatrix}$$

The column matrix $N_L$ is left-handed because it contains only left-handed fields. We introduce the notation:

$$N_L = U n_L, \qquad n_L = \begin{pmatrix} \nu_{1L} \\ \nu_{2L} \end{pmatrix}$$

where $U$ is the unitary mixing matrix and $n_L$ is the column matrix of left handed components of the massive neutrino fields. Then the Dirac-Majorana mass term is diagonal

$$U^T M U = \begin{pmatrix} m_1 & 0 \\ 0 & m_2 \end{pmatrix}$$

$$U = \mathcal{O}\rho$$

$$\mathcal{O} = \begin{pmatrix} \cos\vartheta & \sin\vartheta \\ -\sin\vartheta & \cos\vartheta \end{pmatrix}, \qquad \rho = \begin{pmatrix} \rho_1 & 0 \\ 0 & \rho_2 \end{pmatrix}, \quad |\rho_k|^2 = 1$$

The orthogonal matrix is chosen in order to have

$$\mathcal{O}^T M \mathcal{O} = \begin{pmatrix} m_1^{'} & 0 \\ 0 & m_2^{'} \end{pmatrix}$$

leading to:

$$\tan 2\vartheta = \frac{2m_D}{m_R - m_L}, \qquad m_{1,2}^{'} = \frac{1}{2}\left(m_L + m_R \pm \sqrt{(m_L - m_R)^2 + 4m_D^2}\right) \quad (1.5)$$

$m_L$ and $m_R$ are positive , $m_2^{'}$ is always positive but $m_1^{'}$ is negative if $m_D^2 > m_L m_R$. Since

$$U^T M U = \rho^T \mathcal{O}^T M \mathcal{O} \rho = \begin{pmatrix} \rho_1^2 m_1^{'} & 0 \\ 0 & \rho_2^2 m_2^{'} \end{pmatrix}$$

$\rho_2^2 = 1$ always, and $\rho_1^2 = 1$, if $m_1^{'} \geq 0$ or $\rho_1^2 = -1$, if $m_1^{'} < 0$.

The diagonalized Dirac-Majorana term:

$$\mathcal{L}^{D+M} = \frac{1}{2} \sum_{k=1,2} m_k \overline{\nu_{kL}^c} \nu_{kL} + H.c.$$

is a sum of Majorana mass terms for the massive Majorana neutrino fields

$$\nu_k = \nu_{kL} + \nu_{kL}^c, \qquad (k = 1, 2)$$

Therefore, the two massive neutrinos are Majorana particles.

### 1.3.4 The see-saw mechanism

Trying to explain why we don't see right handed neutrinos and why the neutrinos we detect are so light, the most plausible is to assume that $m_L = 0$ and $|m_D| \ll m_R$. In this case

$$m_1 \simeq \frac{(m_D)^2}{m_R} \ll |m_D|, \quad m_2 \simeq m_R, \quad \tan\vartheta \simeq \frac{m_D}{m_R} \ll 1, \quad \rho_1^2 = -1$$

$m_1$ is much smaller than $m_D$, $m_2$ is in the order of magnitude of $m_R$, a very heavy $\nu_2$ corresponds to a very light $\nu_1$. $m_D$ is the Dirac mass generated with the standard Higgs mechanism, its value is expected to be of the same order of magnitude as the masses of quarks and leptons. The see-saw mechanism gives a small $m_1$ compared to $m_D$ and provides an explanation of the smallness of neutrino masses.

A small mixing angle $\theta$ implies that $\nu_{1L} \simeq \nu_L$ and $\nu_{2L} \simeq \nu_R^c$. Which means that the neutrino participating to weak interactions practically coincides with the light neutrino $\nu_1$, whereas the heavy $\nu_2$ is practically decoupled from interactions with matter.

The basic assumption of the see-saw mechanism is that $m_L = 0$. Its plausibility follows from the fact that $\nu_L$ belongs to a weak isodoublet of the Standard Model:

$$L_L = \begin{pmatrix} \nu_L \\ l_L \end{pmatrix}$$

Since $\nu_L$ has a third component of the weak isospin $I_3 = 1/2$, the combination $\overline{\nu_L^c}\nu_L = -\nu_L^T \mathcal{C}^\dagger \nu_L$ in the Majorana mass term has $I_3 = 1$ and belongs to a triplet. Since in the Standard Model there is no Higgs triplet that could couple to $\overline{\nu_L^c}\nu_L$ in order to form a Lagrangian term invariant under a SU(2)$_L$ transformation of the gauge group, a Majorana mass term for $\nu_L$ is forbidden. In other words, the gauge symmetries of the Standard Model imply $m_L = 0$, as needed for the see-saw mechanism. On the other hand $m_D$ is allowed (generated through the Higgs mechanism) and $m_R$ is also allowed since $\nu_R$ and $\overline{\nu_R^c}\nu_R$ are singlets of the Standard Model gauge symmetries. The only assumption which remains unexplained is the heaviness of $m_R$ with respect to $m_D$.

## 1.4 Oscillation

Why should neutrinos change flavor? The theory of neutrino oscillation at the first glance looks like trying to explain some problematic experiments. Until recently only disappearance experiments were done and before the publication of the SNO results [26], there was no hard evidence of neutrinos appearing in some other flavor. The answer is in the SM himself.

Flavor changes occur in the quark sector: weak eigenstates are linear combinations of flavor eigenstates. The Cabibbo-Kobayashi-Maskawa (CKM) mixing matrix $U_q$ is a 3x3 unitary matrix and describes the relation between the weak and flavor basis:

$$\begin{pmatrix} d' \\ s' \\ b' \end{pmatrix} = U_q \begin{pmatrix} d \\ s \\ b \end{pmatrix}$$

The expression of quark weak charged current has the form:

$$\begin{pmatrix} \bar{u} & \bar{c} & \bar{t} \end{pmatrix}_L \gamma^\mu U_q \begin{pmatrix} d \\ s \\ b \end{pmatrix}$$

In the Standard Model we have 3 lepton families $(e, \nu_e)$, $(\mu, \nu_\mu)$, $(\tau, \nu_\tau)$, quite similar to the quark sector, except that for a long time, neutrinos were thought to be massless. We assume that both quark and lepton sectors should posses similar structures. As an analogy of the weak charged current we write the lepton weak charged current in the form:

$$\begin{pmatrix} \bar{e} & \bar{\mu} & \bar{\tau} \end{pmatrix}_L \gamma^\mu U_l \begin{pmatrix} \nu_1 \\ \nu_2 \\ \nu_3 \end{pmatrix}$$

The weak eigenstates are related to the mass eigenstates by:

$$\begin{pmatrix} \nu_e \\ \nu_\mu \\ \nu_\tau \end{pmatrix} \equiv U_l \begin{pmatrix} \nu_1 \\ \nu_2 \\ \nu_3 \end{pmatrix}$$

were $U_l$ is the lepton mixing matrix. If neutrinos are massless or the masses are equal, it is always possible to rotate the mass eigenstates such that the mixing matrix is the identity matrix, so flavor and mass eigenstates are the same. In this case (contrary to the quark sector) no mixing is possible, as all neutrinos will propagate precisely at the same speed, and the mass eigenstates can never get out of phase. An electron neutrino born will never change its composition, as all parts will move at the same speed, and so the neutrino can never be detected as any other flavor. The interesting case occurs when mass eigenstates are not degenerate.

On the other hand, flavor change of charged leptons have never been seen: $\mu^{\pm} \rightarrow e^{\pm}+\gamma$ violates the lepton number conservation. Muons always decay via the slow weak decay: $\mu^{-} \rightarrow e^{-} + \nu_\mu + \bar{\nu}_e$. This decay conserves lepton number. As a consequence, flavor mixing, if there is any, is possible only between neutrinos.

The above mentioned facts and the Solar Neutrino Problem lead B. Pontecorvo (around 1969) to introduce the idea of neutrino oscillations. He supposed if a neutrino born in the Sun as $\nu_e$ might reach the Earth as $\nu_\mu$, for example, and be undetectable for the early neutrino experiments which were only able to detect $\nu_e$'s . This would be explain why only a fraction of the calculated solar neutrino flux was detected.

### 1.4.1 Two neutrino approximation

If neutrinos have nonzero and different masses we can assume that neutrinos travel as mass eigenstates which have distinct velocities. Assuming two neutrino flavors $\nu_\alpha$ and $\nu_\beta$ and two mass eigenstates $m_1, m_2$, the flavor eigenstates are related to the mass eigenstates by a unitary matrix:

$$\begin{pmatrix} \nu_\alpha \\ \nu_\beta \end{pmatrix} = U \begin{pmatrix} \nu_1 \\ \nu_2 \end{pmatrix} = \begin{pmatrix} \cos\theta & -\sin\theta \\ \sin\theta & \cos\theta \end{pmatrix} \begin{pmatrix} \nu_1 \\ \nu_2 \end{pmatrix}$$

Where $U$ is written as a rotation matrix with parameter $\theta$, the "mixing angle". The probability that a neutrino of one flavor is detected as another after a time $t$ is given by:

$$\mathcal{P}_{\alpha\rightarrow\beta} = \left| < \nu_\beta \left| e^{-i\mathcal{H}t} \right| \nu_\alpha > \right|^2$$

assuming that the neutrino is ultra relativistic ($m \ll p$), the Hamiltonian can be simplified:

$$\mathcal{H} = \sqrt{p_\nu^2 + m^2} \simeq p_\nu + \frac{m^2}{2p_\nu} \simeq p_\nu + \frac{m^2}{2E_\nu}$$

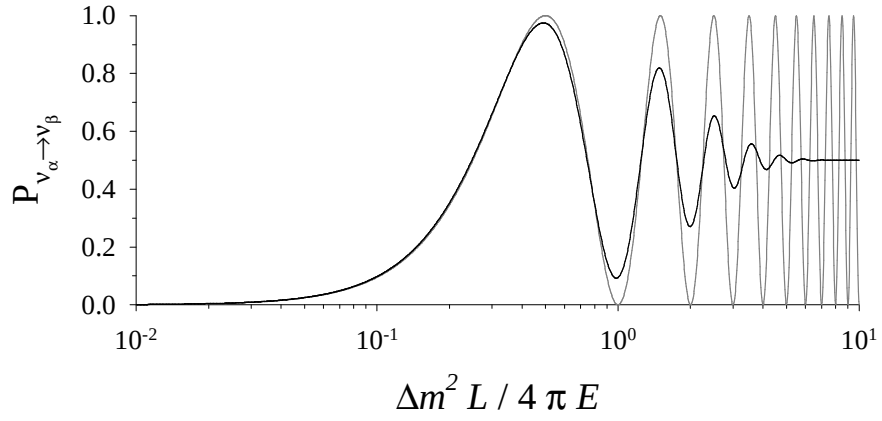


Figure 1.1: Transition probability for $\sin^2 2\theta = 1$ as a function of $\Delta m^2/4\pi E = L/\lambda_{osc}$ The grey line represents the transition probability and the black line the transition probability averaged over a Gaussian spectrum with mean value E and standard deviation $\sigma = E/10$

Substituting this expression in the formula above and using the flavor states expressed in terms of mass eigenstates we get the oscillation probability:

$$\mathcal{P}_{\alpha\to\beta} = \sin^2 2\theta \sin^2\left(\frac{\Delta m^2_{12} L}{2E_\nu}\right) \tag{1.6}$$

where $\Delta m^2_{12} = m^2_2 - m^2_1$ and $L$ is the distance travelled by the neutrino.

The first term of eq. 1.6 describes the transition probability from weak eigenstate $\alpha$ into $\beta$ via all possible mass eigenstates whereas the second term contains the phase information leading to L and E dependence of the transition probability. Thus the transition probability is a periodic function of $L/E$.

The oscillation wave-length in space is given by:

$$\frac{\Delta m^2 \lambda_{osc}}{2E_\nu} = 2\pi \qquad \Rightarrow \qquad \lambda_{osc} = \frac{4\pi E}{\Delta m^2}$$

In useful units the oscillation parameter can be expressed as:

$$\frac{\Delta m^2_{12} L}{2E} \cong 1.27\, \frac{\Delta m^2(eV^2)\ L(km)}{E(GeV)}$$

While a more realistic formalism of course has to deal with 3 neutrino mixing, the 2 neutrino formalism still can be used for calculating the oscillation probabilities in certain experiments. For experiments measuring $\mathcal{P}(\alpha \to \alpha)$ the relation $\mathcal{P}(\alpha \to \beta) = 1 - \mathcal{P}(\alpha \to \alpha)$ is still valid in two neutrino approximation. Results of neutrino experiments are represented in a two-parameter space of $\sin^2 2\theta$ and $\Delta m^2$ like in the example given on fig 1.2 where one can see how the experiment-related parameters are correlated:

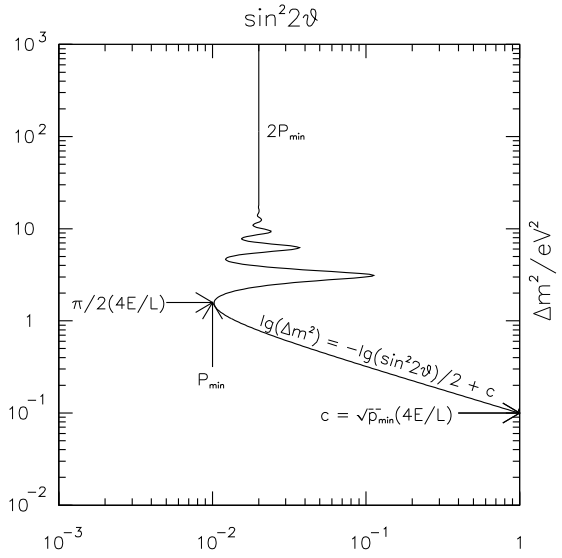


Figure 1.2: Sensitivity of a typical neutrino oscillation experiment: minimal transition probability 1%, mean value of 4E/L = 1 $eV^2$, width of the L/E distribution 10% of the mean value, from reference [5]

- For small $\Delta m^2$, corresponding to $\lambda_{osc} \gg L$ the phase term $\sin^2(\pi L/\lambda_{osc})$ can be approximated by $(\pi L/\lambda_{osc})^2$. This results in a straight line of an experiment -independent slope in a double-logarithmic plot

- The value of $\Delta m^2$, for which the sensitivity in $\sin^2 2\theta$ is maximal, is reached for $L = \lambda_{osc}/2$, independent of $P_{min}$.

- For large $\Delta m^2$, corresponding to small oscillation length, the phase information is lost due to the necessary convolution with the $L/E$ distribution. The averaged transition probability remains:

$$\mathcal{P}_{\alpha\to\beta} = \frac{1}{2}\sin^2 2\theta \qquad (\alpha \neq \beta)$$

In case of a negative result (no signal observed) the parameter region on the right side of the curve in Fig. 1.2 would be excluded. Observation of an oscillation signal would instead result in a preferred parameter region within a band along this curve.

### 1.4.2 Three neutrino mixing

In the general case, mixing should be described by a 3x3 matrix involving all neutrino flavors, the oscillation pattern may be complicated and introduce a combination of

transitions to $\nu_e, \nu_\mu$ and $\nu_\tau$. $U$ the 3x3 unitary matrix can be parameterized in analogy to the quark sector:

$$U = \begin{pmatrix} U_{e1} & U_{e2} & U_{e3} \\ U_{\mu 1} & U_{\mu 2} & U_{\mu 3} \\ U_{\tau 1} & U_{\tau 2} & U_{\tau 3} \end{pmatrix}$$

The mixing matrix, also called Pontecorvo-Maki-Nakagawa-Sakahata matrix, can be expressed in terms of 3 independent angles and 1 complex phase $\delta$ and can be written as the product of three independent rotations with an additional phase. In the case of Majorana neutrinos there are two additional phases that are not observable in neutrino oscillations we therefore ignore them here.

$$U = \begin{pmatrix} 1 & 0 & 0 \\ 0 & c_{23} & s_{23} \\ 0 & -s_{23} & c_{23} \end{pmatrix} \begin{pmatrix} c_{13} & 0 & s_{13}e^{-i\delta} \\ 0 & 1 & 0 \\ -s_{13}e^{-i\delta} & 0 & c_{13} \end{pmatrix} \begin{pmatrix} c_{12} & s_{12} & 0 \\ -s_{12} & c_{12} & 0 \\ 0 & 0 & 1 \end{pmatrix}$$

where $s_{ij} = \sin\theta_{ij}$, $c_{ij} = \cos\theta_{ij}$, which gives:

$$U = \begin{pmatrix} c_{12}c_{13} & s_{12}c_{13} & s_{13}e^{-i\delta} \\ -s_{12}c_{23} - c_{12}s_{13}s_{23}e^{-i\delta} & c_{12}c_{23} - s_{12}s_{13}s_{23}e^{-i\delta} & c_{13}s_{23} \\ s_{12}s_{23} - c_{12}s_{13}c_{23}e^{-i\delta} & -c_{12}s_{23} - s_{12}s_{13}c_{23}e^{-i\delta} & c_{13}c_{23} \end{pmatrix}$$

By symmetry with the quark sector, it is natural to expect CP violation at some level, so the phase $\delta$ must be non-vanishing. For discussion, we assume that the mixing matrix $U$ is real for simplicity. Then the oscillation probability:

$$\mathcal{P}(\nu_\alpha \to \nu_\beta, E, L) = \delta_{\alpha\beta} - 4\sum_{j>k} J_{\alpha\beta jk} \sin^2\left(\frac{\Delta m^2_{jk} L}{4E}\right)$$

were: $J_{\alpha\beta jk} = U_{\beta j}U^*_{\beta k}U^*_{\alpha j}U_{\alpha k}$. Hence there are three independent oscillations with oscillating terms given by:

$$\sin^2\left(\frac{\Delta m^2_{21} L}{4E}\right), \quad \sin^2\left(\frac{\Delta m^2_{31} L}{4E}\right), \quad \sin^2\left(\frac{\Delta m^2_{32} L}{4E}\right)$$

In the light of current experimental results on solar and atmospheric neutrinos, we can consider the approximation that only one mass scale is relevant. In the one mass scale approximation we assume that the neutrino mass pattern is such that:

$$\left|\Delta m^2_{21}\right| \ll \left|\Delta m^2_{31}\right| \approx \left|\Delta m^2_{32}\right| \equiv \left|\Delta M^2\right|$$

For example if we interpret the solar and atmospheric neutrino experiments, we find:

$$\left|\Delta m^2_{21}\right| \approx 10^{-5}\ eV^2, \qquad \left|\Delta m^2_{32}\right| \approx 10^{-3}\ eV^2$$

The three family oscillation driven by the largest $\Delta M^2$ parameter is described by only three parameters: the mass difference $\Delta M^2$ and the two mixing angles $\theta_{13}$ and $\theta_{23}$. The dependence on the $\theta_{12}$ angle is not observable in this approximation.

We can write the oscillation probabilities in the following form:

$$\begin{aligned}
\mathcal{P}(\nu_e \to \nu_e) &\approx 1 - \sin^2(2\theta_{13}) \sin^2\left(\frac{\Delta M^2 L}{4E}\right) \\
\mathcal{P}(\nu_e \to \nu_\mu) &= \mathcal{P}(\nu_\mu \to \nu_e) \approx \sin^2(2\theta_{13}) \sin^2(\theta_{23}) \sin^2\left(\frac{\Delta M^2 L}{4E}\right) \\
\mathcal{P}(\nu_e \to \nu_\tau) &\approx \sin^2(2\theta_{13}) \cos^2(\theta_{23}) \sin^2\left(\frac{\Delta M^2 L}{4E}\right) \\
\mathcal{P}(\nu_\mu \to \nu_\tau) &\approx \sin^2(2\theta_{23}) \cos^4(\theta_{13}) \sin^2\left(\frac{\Delta M^2 L}{4E}\right)
\end{aligned}$$

### 1.4.3 Matter effects

When neutrinos propagate in matter instead of vacuum, the oscillation probabilities can be different because of the interactions with the electrons, protons and neutrons. Neutrinos interact with matter via neutral-current interactions, regardless to their flavor. This interaction creates a phase factor which has no physical effect on oscillations. On the contrary charged-current interactions which have effect only on $\nu_e$'s do play a role. For the scattering process $\nu + e \to \nu + e$ the refractive index will be different for electron neutrinos and other flavors due to the additional contribution of $W$-boson exchange in the scattering process. This difference in neutrino refraction indices will introduce an additional phase shift which can change the oscillation probability.

Neutrino oscillations in the matter were first investigated by Wolfenstein [10] and later by Mikheyev and Smirnov who pointed out the appearance of a resonance region: at a given neutrino energy, the probability for oscillation will be enhanced to large values, even when the mixing angles in vacuum are small. This mechanism is called the MSW (Mikheyev-Smirnov-Wolfenstein) effect.

The evolution equation describing neutrino oscillations in matter in the case of three flavors, in flavor basis:

$$i\frac{d\vec{\nu}}{dt} = \frac{1}{2E}\left[U \begin{pmatrix} m_1^2 & 0 & 0 \\ 0 & m_2^2 & 0 \\ 0 & 0 & m_3^2 \end{pmatrix} U^\dagger + \begin{pmatrix} 2\sqrt{2}G_F N_e E & 0 & 0 \\ 0 & 0 & 0 \\ 0 & 0 & 0 \end{pmatrix}\right] \vec{\nu}$$

where the potential due to the coherent scattering with electrons has been added. Here $N_e$ is the electron density and with $Y_e \approx 0.5$ the number of electron per nuclei we have:

$$2\sqrt{2}G_F N_e \ (eV^2) = 7.6 \times 10^{-14}\, Y_e\, \rho \left(\frac{g}{cm^3}\right) \simeq 3.8 \times 10^{-14}\, \rho \left(\frac{g}{cm^3}\right)$$

To simplify the discussion we restrict ourselves to only two flavor oscillations, for example between $\nu_e$ and $\nu_\mu$. The evolution equation can be brought to the form:

$$i\frac{d\vec{\nu}}{dt} = \frac{1}{2E}\begin{pmatrix} A + (m_1^2 - m_2^2)\cos 2\theta & (m_2^2 - m_1^2)\sin 2\theta \\ (m_2^2 - m_1^2)\sin 2\theta & -(m_1^2 - m_2^2)\cos 2\theta \end{pmatrix} \vec{\nu}$$

where $A = 2\sqrt{2}G_F N_e$. After diagonalization the mass eigenstates in matter $\nu_{1m}$ and $\nu_{2m}$ have the following eigenvalues:

$$m_{1,2m} = \frac{1}{2}\left[(m_1^2 + m_2^2) + A \mp \sqrt{(A - \Delta m^2 \cos 2\theta)^2 + (\Delta m^2)^2 \sin^2 2\theta}\right],$$

$$\left(\Delta m^2 = m_2^2 - m_1^2\right)$$

Since matter effects appear through the interaction with electrons in matter (and not positrons), the effect for anti-neutrinos will be opposite to that of neutrinos and one should replace $A \to -A$ for anti neutrinos. For the sake off simplicity, it is useful to keep the expressions of the oscillation probability in vacuum and replace the mixing angle with an effective mixing angle as well $\Delta m^2$ with an effective $\Delta M^2_{\pm}$

$$\begin{pmatrix} \nu_e \\ \nu_\mu \end{pmatrix} = \begin{pmatrix} \cos\theta_m & \sin\theta_m \\ -\sin\theta_m & \cos\theta_m \end{pmatrix} \begin{pmatrix} \nu_{1m} \\ \nu_{2m} \end{pmatrix}$$

where the effective angle $\theta_m$is given by:

$$\sin^2 2\theta_m^{\mp} = \frac{\sin^2 2\theta}{\sin^2 2\theta + (x \mp \cos 2\theta)^2}$$

where the minus sign applies to neutrinos and the plus to anti-neutrinos.

$$x = \frac{A}{\Delta m^2} \approx 0.38 \times 10^{-4} \frac{\rho\left(\frac{g}{cm^3}\right) E\,(GeV)}{\Delta m^2\,(eV^2)}$$

Because of matter effects the transition probabilities for neutrinos and anti-neutrinos will be different:

$$\begin{aligned} \mathcal{P}(\nu_e \to \nu_\mu) &= \sin^2(2\theta_m^-)\sin^2\left(\frac{\Delta M^2_- L}{4E}\right) \\ \mathcal{P}(\bar{\nu}_e \to \bar{\nu}_\mu) &= \sin^2(2\theta_m^+)\sin^2\left(\frac{\Delta M^2_+ L}{4E}\right) \end{aligned}$$

where the effective mass difference squared in matter is

$$\Delta M^2_{\pm} = \Delta m^2 \sqrt{\sin^2 2\theta + (x \pm \cos 2\theta)^2}$$

The sign of $\Delta m^2$ is (unlike in vacuum) relevant for oscillations in matter. For $\Delta m^2 > 0$ and neutrinos, a resonance condition will be met when $x(E, \Delta m^2, \rho) \approx \cos 2\theta$ and the oscillation amplitude will reach the maximum:

$$A \approx \Delta m^2 \cos 2\theta \quad \Rightarrow \quad \sin^2 2\theta_m = 1$$

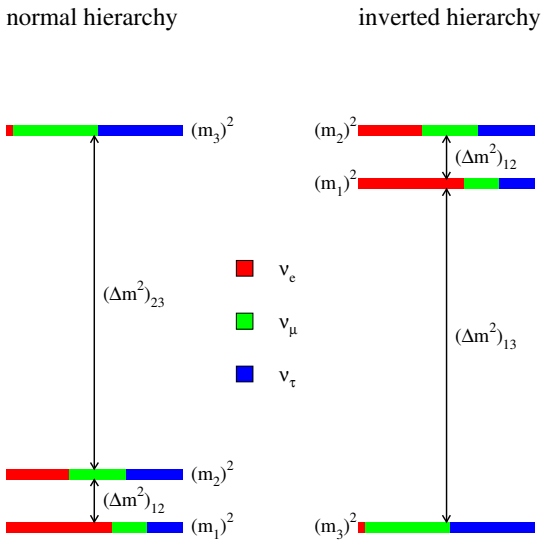


Figure 1.3: Neutrino mass scales

i.e. the mixing angle in matter is essentially maximal, independently on how small it is in vacuum. This is the resonance effect in the transition probability. We also note that suppression occurs when

$$A > 2\Delta m^2 \cos 2\theta \quad \Rightarrow \quad \sin^2 2\theta_m < \sin^2 2\theta$$

and the mixing angle is smaller than in vacuum.

While the oscillation probability is enhanced at the resonance energy, it is suppressed for anti-neutrinos since $A$ has to be replaced with $-A$. For $\Delta m^2 < 0$ the situation is reversed. As a consequence we can use matter effects to determine the sign of $\Delta m^2$ and that would help us to disentangle the two possible mass hierarchies that can not be separated by oscillations in vacuum. On Fig. 1.3 we can see the two possible mass hierarchies and allowed regions by different experiments.

Neutrinos emitted from the sun are created in the core of the sun where the electron density is the highest, matter effects could modify the oscillation parameters and have to be taken into account. Similarly, when atmospheric neutrinos travel through the Earth, a resonance will occur, but at much higher energies as for solar neutrinos. For $\Delta m^2 \approx 10^{-3}$ the resonance energy is about 4 GeV which is within the energy range accessible for accelerator experiments so it has to taken into account at long baseline experiments as well. As a consequence, the two different mass hierarchies from the point of view of the experiments can be interpreted in the following way:

- Normal hierarchy, $m_1 < m_2 < m_3$: solar neutrinos oscillate between the two light neutrinos and atmospheric neutrinos oscillate between the light neutrinos and the heaviest one.

- Inverted hierarchy, $m_3 < m_2 < m_1$: solar neutrinos oscillate between the two heaviest neutrinos, with absolute masses close to each other, and atmospheric neutrinos oscillate between the light neutrino and the heaviest one.

## 1.5 Beyond the Standard Model

Massive neutrinos imply the existence of right-handed neutrinos which in the SM are not needed. Right handed neutrinos are completely decoupled if m=0 but if they have a nonzero mass one can always apply a Lorentz-boost such that in the new reference frame they are left handed.

While the Dirac mass term (m=0) is lepton number conserving the Majorana mass term violates the lepton number by two units, since it transforms neutrino into antineutrino and vice-versa. The inclusion of right-handed neutrino states forces the existence of lepton number violating terms.

Neutrino masses are a strong evidence of physics beyond the Standard Model and so far the only one.

Dirac mass term is generated with the standard Higgs mechanism. For example for electron neutrinos:

$$\begin{aligned}\mathcal{L} &= -\lambda_\nu \left(\bar{L}\phi R + \bar{R}\phi^+ L\right) \\ &= -\lambda_\nu \left( \begin{pmatrix} \bar{\nu}_e & \bar{e}^- \end{pmatrix}_L \begin{pmatrix} \phi^+ \\ \phi^0 \end{pmatrix} \nu_{eR} + \bar{\nu_{eR}} \begin{pmatrix} (\phi^+)^* & (\phi^0)^* \end{pmatrix} \begin{pmatrix} \nu_e \\ e^- \end{pmatrix}_L \right)\end{aligned}$$

If:

$$\phi \equiv \frac{1}{\sqrt{2}} \begin{pmatrix} 0 \\ v \end{pmatrix}$$

one gets:

$$\begin{aligned}\mathcal{L} &= -\lambda_\nu \left( \begin{pmatrix} \bar{\nu}_e & \bar{e}^- \end{pmatrix}_L \frac{1}{\sqrt{2}} \begin{pmatrix} 0 \\ v \end{pmatrix} \nu_{eR} + \bar{\nu_{eR}} \frac{1}{\sqrt{2}} \begin{pmatrix} 0 & v \end{pmatrix} \begin{pmatrix} \nu_e \\ e^- \end{pmatrix}_L \right) \\ &= -\frac{\lambda_\nu}{\sqrt{2}} v (\bar{\nu_{eL}} \nu_{eR} + \bar{\nu_{eR}} \nu_{eL})\end{aligned}$$

which yields the Dirac mass term

$$m_D = \frac{\lambda_\nu v}{\sqrt{2}}$$

Hence the Dirac mass term can be generated by the standard Higgs mechanism. On the other hand Majorana mass terms cannot be accommodated within the standard Higgs mechanism.

Today we think that the SM is valid only below the energy range of the new physics. Below this energy the SM Lagrangian is an effective low energy theory like the Fermi

theory for weak interactions. Adding a dimension-5 operator gives a natural extension (but non re-normalizable) of the standard model and generates the Majorana mass term. The SM admits only dimension-4 operators: One can write formally an expansion in order of dimensionality of operators $\mathcal{O}_n$ suppressed by order of the new physics scale.

$$\mathcal{L} \rightarrow \mathcal{L}_{SM,free\,fields} + \mathcal{L}_{SM,interactions} + \mathcal{L}_{SM,Higgs} + \sum_{n>4} \frac{1}{\Lambda_{NP}^{n-4}} \mathcal{O}_n \tag{1.7}$$

All Lagrangian terms have dimension of $(\text{energy})^4$. The dimension-5 character of the operator (for n=5) in 1.7 refers to the power of energy of the dimension of the operator which is divided by $\Lambda_{NP}$ in order to obtain the Lagrangian term with correct dimension. $\Lambda_{NP}$ is the high energy scale at which the new theory breaks down to the Standard Model.

One can consider dimension-5 operators that generate Majorana neutrino masses as the result of the interaction with the same standard Higgs field used to generate the masses of other fermions. The non-renormalizable operator is of the type:

$$\frac{\lambda_\nu}{\Lambda_{NP}} \left(\bar{L}\phi\right)\left(\phi^+ L^c\right) + h.c. = \frac{\lambda_\nu}{\Lambda_{NP}} \left(\bar{\nu}_e\ \bar{e}^-\right)_L \begin{pmatrix} \phi^+ \\ \phi^0 \end{pmatrix} \left(\left(\phi^+\right)^*\ \left(\phi^0\right)^*\right) \begin{pmatrix} \nu_e^c \\ e^+ \end{pmatrix}_L + h.c.$$

which after spontaneous symmetry breaking induces the following neutrino mass term:

$$\frac{\lambda_\nu}{\Lambda_{NP}} \begin{pmatrix} \bar{\nu}_e & \bar{e}^- \end{pmatrix}_L \frac{1}{\sqrt{2}} \begin{pmatrix} v \\ 0 \end{pmatrix} \frac{1}{\sqrt{2}} \begin{pmatrix} v & 0 \end{pmatrix} \begin{pmatrix} \nu_e^c \\ e^+ \end{pmatrix}_L + h.c. \;=\; \frac{1}{2}\frac{\lambda_\nu v^2}{\Lambda_{NP}} \bar{\nu}_e \nu_e^c + h.c.$$

This is precisely the Majorana mass term. It is naturally suppressed by the scale of the new physics $\Lambda_{NP}$. The resulting mass term is of the form:

$$m_L = \frac{\lambda_\nu v^2}{\Lambda_{NP}} \tag{1.8}$$

this relation shows that the Majorana mass $m_L$ is suppressed with respect to $v$ by the small ratio $v/\Lambda_{NP}$. In other words, since the Dirac mass term $m_D$ is equal to $v/\sqrt{2}$ times the Yukawa coupling coefficient, the relation 1.8 has a see-saw form. Therefore the effect of the dimension-5 operator does not spoil the natural suppression of the light neutrino mass provided by the see-saw mechanism. Indeed, considering $m_L \sim m_D^2/m_R$ and taking into account $m_1 = \left|m_1^{'}\right|$, from 1.5 we obtain:

$$m_1 \simeq \left| m_L - \frac{(m_D)^2}{m_R} \right|$$

This shows that the see-saw mechanism is operating even if $m_L$ is not zero, but is generated by the dimension-5 operator. On the other hand, if the chiral right-handed neutrino field $\nu_R$ does not exist, the standard see-saw mechanism cannot be implemented, but a Majorana neutrino mass $m_L$ can be generated by a dimension-5 operator and eq. 1.8 shows that the suppression of the light neutrino mass is natural and of see-saw type.

# Chapter 2

# Experimental facts

To understand the current status of neutrino physics one should be familiar with the actual values of neutrino masses and oscillation parameters. Below I will try to give a review of the most important experiments that lead to the current understanding of neutrino physics with a special regard to the still missing parameters that give the main motivation for the OPERA experiment.

## 2.1 Neutrino mass measurements

The study of decays with neutrinos involved gives a model independent way of measuring neutrino masses. In case of non-zero neutrino mass, the mass could be calculated reconstructing the kinematics of the decay. The current values of neutrino masses and oscillation parameters are taken from the Particle Data Group's Review of Particle Physics ([9]), unless otherwise mentioned.

- $\nu_e$ mass
  The mass of the electron-antineutrino has been investigated using the $\beta$-decay of tritium:
  $$^3_1\mathrm{H} \rightarrow {}^3_2\mathrm{He} + e^- + \bar{\nu}_e$$
  The advantage of using tritium is the small transition energy (18 keV) and the absence of screening effects by additional electrons. The current limit:
  $$m_{\bar{\nu}_e} < 3\,\mathrm{eV}$$

- $\nu_\mu$ mass
  The best limits for the mass of the $\nu_\mu$ come from the study of the decay
  $$\pi^+ \rightarrow \mu^+ + \nu_\mu$$
  with the pion at rest. The best limit is:
  $$m_{\nu_\mu} < 170\,\mathrm{keV}$$

- $\nu_\tau$ mass
  Limits for the $\nu_\tau$ mass have been derived from the study of the decays

$$\begin{aligned} \tau &\rightarrow 5\pi(\pi^0) + \nu_\tau \\ \tau &\rightarrow 3\pi(\pi^0) + \nu_\tau \end{aligned}$$

  The current best limit is:

$$m_{\nu_\tau} < 18.2\,\text{MeV}$$

### 2.1.1 Other mass measurement methods

If the neutrino is a Majorana particle, the mass can be determined measuring the half-life of the neutrino-less double-beta decay. The best limit was obtained by the Heidelberg-Moscow experiment [30]. Assuming that neutrinos are Majorana particles they obtain a positive result:

$$m_\nu < 0.4\,\text{eV}$$

We have to mention here the WMAP (cosmic background) experiment [31] that measured subtle temperature fluctuations within the oldest light in the universe. Combined with large scale structure studies a new bound on the sums of the neutrino masses is obtained $\sum m_\nu < 1.8\,\text{eV}$.

## 2.2 Oscillation experiments

### 2.2.1 Solar neutrino experiments

Solar neutrinos are produced by the nuclear fusion processes in the core of the Sun. The most important processes supplying neutrinos are generated in the so-called pp-cycle:

$$\begin{array}{lcll} p + p & \rightarrow & {}^2_1D + e^+ + \nu_e & 0.42\,\text{MeV} \\ p + p + e^- & \rightarrow & {}^2_1D + \nu_e & 1.44\,\text{MeV} \\ {}^7_4Be + e^- & \rightarrow & {}^7_3Li + \gamma + \nu_e & 0.86\,\text{MeV} \\ {}^8_5B & \rightarrow & 2\alpha + e^+ + \nu_e & 14.6\,\text{MeV} \end{array}$$

The given energies are the neutrino energies for the electron capture reactions and the maximal neutrino energies for the $\beta$ decay reactions. All reactions in the Sun produce electron neutrinos which can be summarized looking at the net reaction of the pp-cycle:

$$2e^- + 4p \rightarrow {}^4He + 2\nu_e$$

The neutrino spectra of the Sun is shown on Fig. 2.1 including neutrinos from the less significant CNO cycle as well. The fundamental pp reaction is closely related to the overall luminosity of the Sun and can be precisely predicted.

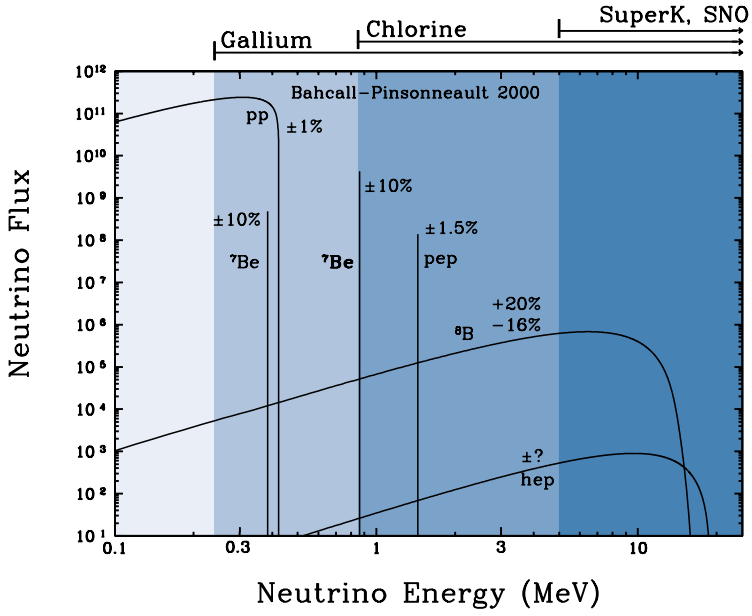


Figure 2.1: Solar neutrino spectra

The first observation of solar neutrinos was performed by Davis and his collaborators ([12]) in the pioneering Homestake experiment. It was a radiochemical experiment using 615 tons of tetrachlorethylene ($C_2Cl_4$) measuring the production rate of $^{37}Ar$ in the reaction

$$\nu_e + {}^{37}Cl \rightarrow {}^{37}Ar + e^-$$

With a threshold of 814 keV, the reaction is not sensitive to the dominant pp component of the neutrino flux, but probes the rare $^7Be$ and $^8B$ neutrinos.

The result from the Homestake experiment indicated that only about 1/3 of the expected solar neutrino flux was observed. This observation is known as the solar neutrino deficit.

The solar neutrino problem was confirmed by the next generation experiments. Both Kamiokande (water Cerenkov [21]) and GALLEX (Gallium [17]) experiments found only about half of the predicted flux. The importance of this discovery is underlined by the fact that Ray Davis (Homestake) and Mastoshi Koshiba (Kamiokande) shared the Nobel Prize in physics in 2002.

The most recent and maybe the most important contribution to solve the solar neutrino puzzle comes from the Sudbury Neutrino Observatory (SNO) experiment ([26]) showing that approximately two-thirds of the solar neutrinos oscillate into other flavors before reaching the Earth.

The idea behind the SNO detector is to have multiple detection channels which could help to distinguish between different flavors of neutrinos. The SNO detector is

basically a water Cerenkov detector with heavy water ($D_2O$) instead of normal water. The charged-current channel (CC) is sensitive only to electron neutrinos

$$\nu_e + d \rightarrow p + p + e^-$$

The electron carries off most of the neutrino energy, its detection allows the experimentalist to determine the spectrum of solar $\nu_e$'s, not just the flux. A second reaction, the neutral-current (NC) breakup of deuterium, gives the total flux, independent of flavor (the $\nu_e, \nu_\mu$ and $\nu_\tau$cross-sections are identical)

$$\nu_x + d \rightarrow n + p + \nu_x$$

The only signal for this reaction in a water Cerenkov detector is the neutron, which can be observed as it captures via the (n,$\gamma$) reaction.

The detector also provided a third channel, neutrino elastic scattering (ES) off electrons which is sensitive to $\nu_e$'s and with a reduced sensitivity to $\nu_\mu$'s and $\nu_\tau$'s. The ES reaction provides a direct cross-check against SuperKamiokande. Assuming no oscillation the SNO detection rate is equivalent to a $\nu_e$ flux of

$$\Phi_{SNO}^{ES} = 2.39 \pm 0.24 \pm 0.12 \ \times 10^6 \text{cm}^2\text{s}^{-1}$$

(see [26]) a result in excellent agreement with that of SuperKamiokande [19],

$$\Phi_{SK}^{ES} = 2.35 \pm 0.02 \pm 0.08 \ \times 10^6 \text{cm}^2\text{s}^{-1}$$

The new information provided by SNO comes from the two reactions on deuterium. The CC channel only sensitive to $\nu_e$'s and assuming an undistorted $^8$B flux gives:

$$\Phi_{SNO}^{CC}(\nu_e) = 1.76 \pm 0.06 \pm 0.09 \ \times 10^6 \text{cm}^2\text{s}^{-1}$$

The CC flux is less than that deduced from the ES rate, indicating that $\nu_\mu$'s and $\nu_\tau$'s must contribute to the latter. The NC channel gives the total flux

$$\Phi_{SNO}^{NC}(\nu_x) = 6.42 \pm 1.57 \pm 0.58 \ \times 10^6 \text{cm}^2\text{s}^{-1}$$

Combining with the CC signal yields

$$\begin{aligned} \Phi_{SNO}(\nu_e) &= 1.76 \pm 0.05 \pm 0.09 \ \times 10^6 \text{cm}^2\text{s}^{-1} \\ \Phi_{SNO}(\nu_\mu/\nu_\tau) &= 3.41 \pm 0.45 \pm 0.46 \ \times 10^6 \text{cm}^2\text{s}^{-1} \end{aligned}$$

The presence of heavy-flavor solar neutrinos and thus neutrino oscillations is confirmed at the 5.3 $\sigma$ level. Furthermore the total flux is in excellent agreement with the predictions of the Standard Solar Model (SSM).

After the first results published, SNO is continued operating with salt (NaCl) added to the water. The Cl in the salt is an excellent (n,$\gamma$) target, producing about 8 MeV in $\gamma$'s. The increased neutron capture efficiency improved significantly the precision of the NC interaction measurements. The published results from the salt phase [27], are in agreement with the first results.

### 2.2.2 Reactor experiments

Nuclear reactors are an intense source of $\bar{\nu}_e$. Unsurprisingly, the first detection of a free neutrino was performed at a nuclear reactor by Reines and Cowan [11]. The source of neutrinos are $\beta$-decays of the neutron rich fragments in the fission of $^{235}U$ and $^{239}Pu$. Reactors produce exclusively $\bar{\nu}_e$, related to the net reaction $n \rightarrow p + e^- + \bar{\nu}_e$, which is necessary to create stable, light nuclei with a lower neutron excess. In average we expect 6.1 $\bar{\nu}_e$ emitted per fission. We also know that the thermal energy released in the fission process is about 200 MeV. Monitoring the thermal output of a reactor, we can estimate the neutrino flux with a precision of ∼1-2%. It is a consequence, that the neutrino oscillation experiments at reactors are "disappearance" experiments, where the measured $\bar{\nu}_e$ flux is compared to the expected one.

From the point of view of oscillation parameters the most important contribution comes from the CHOOZ experiment [16]. The CHOOZ detector was located in an underground laboratory at a distance of about 1 km from the power plant in the village of the same name in the north of France. The 1 km baseline and the energy of about ∼3 MeV gives an average value of $L/E$ ∼300 which classifies CHOOZ as a long baseline experiment.

The sensitive part of the detector consists of 5 tons of liquid scintillator loaded with 0.09% of gadolinium. The detection of neutrinos is based on the inverse $\beta$-decay

$$\bar{\nu}_e + p \rightarrow e^+ + n$$

Like in the first neutrino detection experiment, photomultipliers detect the two gammas emitted after the annihilation of the positron in coincidence with the gamma emitted by the gadolinium after neutron capture.

The neutrino signal was clearly visible and it's correlation with the reactor power was spectacular. However, the experiment gave negative results in the sense that $\nu_e \rightarrow \nu_x$ oscillations were practically excluded. The measured versus expected ratio, averaged over the energy spectrum is close to one:

$$R = 1.01 \pm 2.8\% \pm 2.7\%$$

This translates into $\Delta m^2 \leqslant 8 \cdot 10^{-4}\text{eV}^2$ at full mixing and $\sin^2 2\theta \leqslant 0.17$ at large $\Delta m^2$ values.

Another important reactor experiment is KamLAND [29]. KamLAND uses as detector the old Kamioka Liquid Scintillator and the source of $\bar{\nu}_e$'s are all the nuclear reactors in a ~200 km radius around the detector. The results of KamLAND are complementary to the results of CHOOZ (see Fig. 2.2). Since the distance between the source and the detector is much longer, KamLAND probes the same region as solar neutrino experiments: $\nu_e \rightarrow \nu_\mu$ oscillations (assuming CPT invariance), while CHOOZ was probing rather $\nu_e \rightarrow \nu_\tau$. The number of detected $\bar{\nu}_e$'s is consistent with the Large Mixing Angle (LMA) hypothesis of neutrino oscillations. The ratio of the measured over the expected flux is:

$$R = 0.61 \pm 0.085 \pm 0.041$$

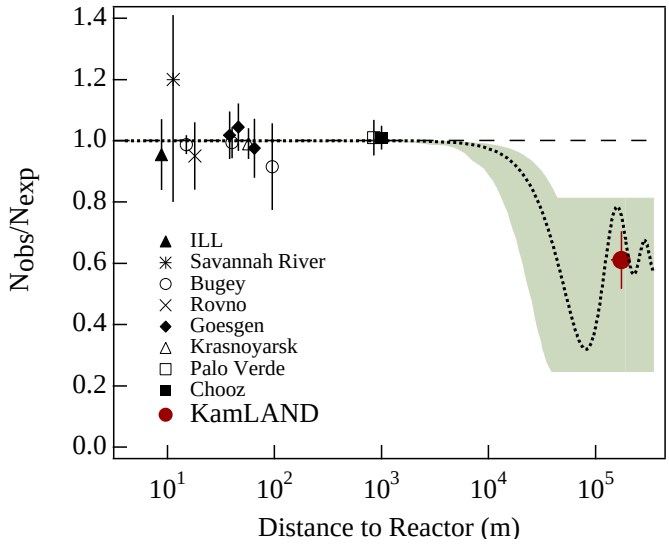


Figure 2.2: The ratio of the expected and measured neutrino flux in function of the distance between the source and the detector. The shaded region corresponds to the flux predictions from solar neutrino data and KamLAND is situated in this region. Source: [28].

The two neutrino oscillation analysis of the KamLAND data gives $\Delta m^2 = 7.9^{+0.6}_{-0.5} \times 10^{-5}$ eV$^2$. The parameter region excluded by the KamLAND and CHOOZ experiments is shown on Fig. 2.3.

### 2.2.3 Atmospheric neutrino experiments

Atmospheric neutrinos are produced when high energy cosmic-ray particles, mainly protons, hit the upper part of the atmosphere inducing hadronic showers that contain a large fraction of pions

$$p + N \rightarrow \pi + X$$

Due to the low density of the atmosphere, most of the pions decay before interacting

$$\pi \rightarrow \mu + \bar{\nu}_\mu(\nu_\mu)$$

and a large fraction of muons decays as well before reaching the ground

$$\mu \rightarrow e + \bar{\nu}_\mu(\nu_\mu) + \nu_e(\bar{\nu}_e)$$

Since the initial cosmic-ray spectrum is not very well known, atmospheric neutrino experiments measure the ratio between $\nu_\mu$ and $\nu_e$. The results are usually given in the form of the double ratio

$$R = \frac{(N(\nu_\mu)/N(\nu_e))_{data}}{(N(\nu_\mu)/N(\nu_e))_{simu}}$$

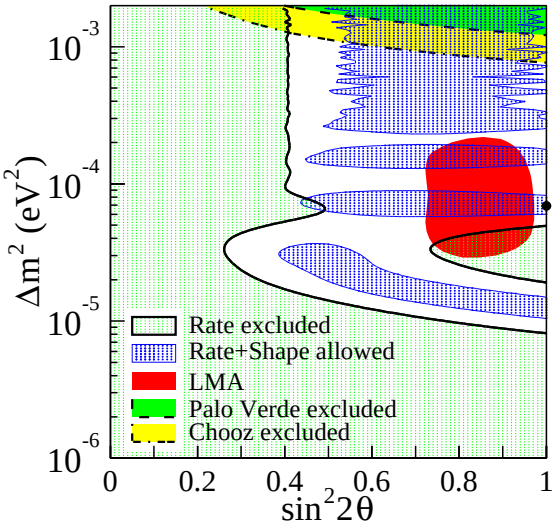


Figure 2.3: Excluded parameter region obtained by the KamLAND experiment, compared to the region excluded by the CHOOZ experiment and the allowed region of the LMA solution

The energy range probed by these measurements covers the range from 100 MeV up to 10 GeV.

Nusex [23] in the Mont-Blanc tunnel and the Frejus experiment [22] at the Frejus tunnel have obtained good agreement with the expectations. However, starting with the IMB experiment [24] all experiments measured a deficit of neutrinos. Kamiokande was the first experiment [18] to report convincing result concerning possible anomalies in the flux of atmospheric neutrinos:

$$\begin{aligned} R_{K,SubGeV} &= 0.60 \pm 0.05 \\ R_{K,MultiGeV} &= 0.57 \pm 0.07 \end{aligned}$$

An anomalous effect in both sub-GeV and multi-GeV samples was observed. The multi-GeV result provided a stronger evidence since at lower energies the direction of the outgoing lepton is smeared by the Fermi motion. Since the Kamiokande numbers were in contradiction with the IMB results, it was important that they were confirmed by the Sudan-II experiment [25] which found

$$R_{Sudan-II} = 0.68 \pm 0.11 \pm 0.06$$

The most important contribution to the field is given by the Super-Kamiokande experiment [20]. The Super-Kamiokande is a 50 kton water Cerenkov detector which consists off an inner detector with $\sim$1100 20-inch photomultipliers and an outer veto. The pulse height and timing information recorded by the inner detector PMT's are used to reconstruct the kinematics of the neutrino events. The outer veto detector surrounds

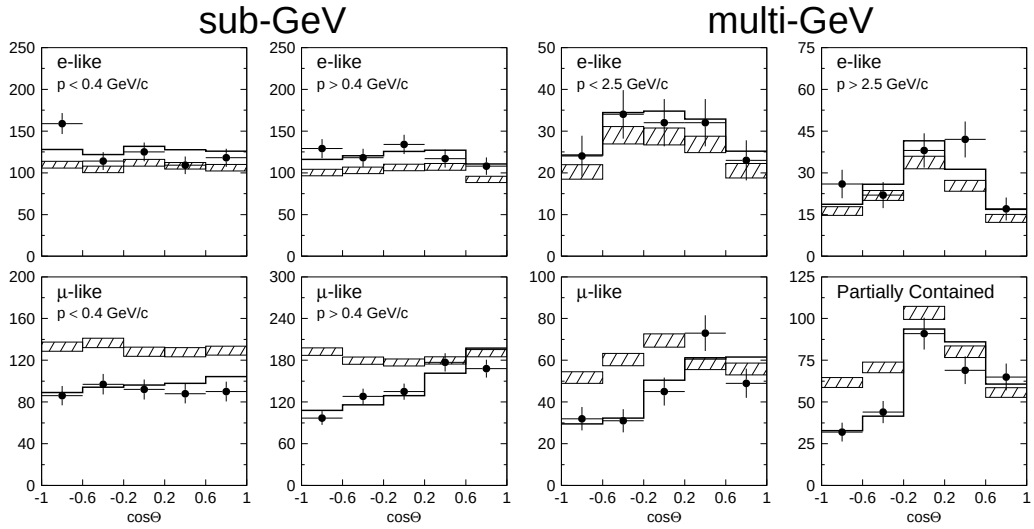


Figure 2.4: Zenith angle distribution of electron and muon-like events in SuperK

the inner detector completely, it is useful to identify incoming cosmic-ray muons and exiting particles produced in neutrino events which occur in the inner detector. During an exposure equivalent of 70 kton$\times$year, Super-Kamiokande collected enough statistics to confirm the findings of the previous experiments:

$$\begin{aligned} R_{SK,SubGeV} &= 0.658 \pm 0.016 \pm 0.035 \\ R_{SK,MultiGeV} &= 0.702 \pm 0.032 \pm 0.101 \end{aligned}$$

The double-ratio however does not give any information about the origin of the anomaly. We don't know if the $\nu_e$'s are too many or $\nu_\mu$'s are too few. At this point Super-Kamiokande was able to provide new information, measuring the zenith angle distribution of the incoming neutrinos. The zenith angle is a direct measure of the flight path between the source and the detector. For downward neutrino the average path length is about 15 km, while for upward going neutrinos produced on the opposite side of the Earth this distance is about 12'000 km. At higher energies (>400 MeV), the direction of the charged lepton is strongly correlated with that of the incoming neutrino therefore the effect is best seen above this threshold.

The plots shown on Fig. 2.4 indicate that there are less upward going $\nu_\mu$'s than expected. The most plausible explanation is that $\nu_\mu$'s oscillate into some other flavor. Since in the previous section we have seen that the CHOOZ experiment practically excluded the $\nu_\mu \rightarrow \nu_e$ transition, it remains to consider $\nu_\mu \rightarrow \nu_\tau$ oscillations, even though the $\nu_\tau$ appearance has not been detected so far. The results of Super-Kamiokande are consistent with full mixing ($\sin^2 2\theta = 1$) and $\Delta m^2 = 3.2 \times 10^{-3}\, eV^2$ (see Fig. 2.5 ).

To compleat the experimental evidences of neutrino oscillations, one should prove that disappearing $\nu_\mu$'s in the Super-Kamiokande experiment appear as $\nu_\tau$'s. The only experiment forseen in the near future to detect $\nu_\tau$ appearance is OPERA. The goal of

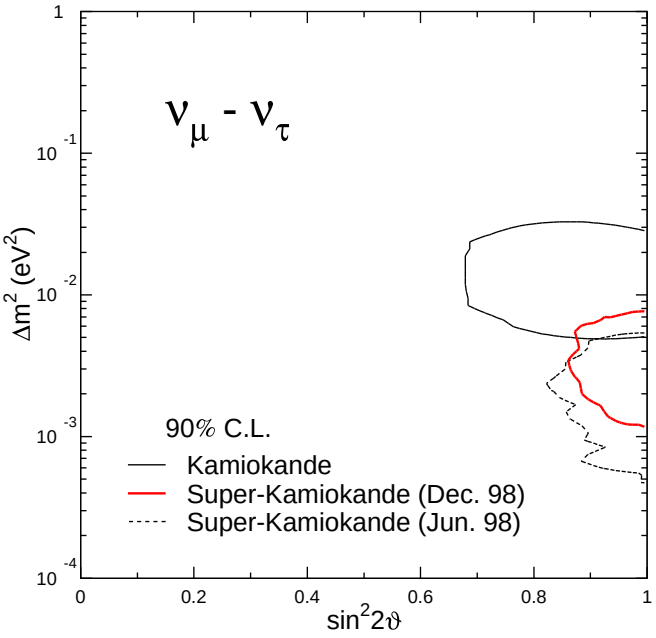


Figure 2.5: Parameter region allowed by the Super-Kamiokande experiment

OPERA will be to measure $\nu_\mu \rightarrow \nu_\tau$ oscillations in the parameter range indicated by Super-Kamiokande. Further emphasizes the importance of the OPERA experiment, the possibility to measure $\theta_{13}$ below the limit set up by the CHOOZ experiment.

In the next chapter we give a short description of the OPERA detector with the projected physics performance of the experiment.

# Chapter 3

# The OPERA detector

The OPERA (Oscillation Project with Emulsion tRacking Apparatus ) experiment or CNGS1 was approved in 2001 by CERN and presently is under construction. Data-taking is expected to start in 2006. The detector itself is located at 120 km from Rome in the INFN-LNGS underground laboratory in the Gran Sasso road tunnel.

OPERA is a hybrid detector comprising a number of electronic detectors and a specially designed nuclear emulsion stack interlaced with lead plates. The total target mass of the detector will be about 1.8 kt. This impressive mass needed for neutrino detection is combined with an even more impressive spatial resolution of about a $\mu m$, characteristic of the nuclear emulsion technique.

## 3.1 CNGS

CNGS stands for "CERN Neutrino beam to Gran Sasso". A neutrino beam produced at CERN is directed towards the LNGS underground laboratory, 720 km away.

On Fig. 3.1 we can see the schematic view of the apparatus necessary to produce such a beam. A 400 GeV proton beam coming from the Super Proton Synchrotron (SPS) hits a target of 2 m long graphite rods and produces secondary pions and kaons. To keep the secondary particles in the beam-line magnetic lenses are needed. These are the "Horn" and "Reflector" seen on figure 3.1. The pions and kaons will enter a 1 km long decay tube where the $\pi^+$ and $K^+$ decay producing $\mu^+$ and $\nu_\mu$ .

At the end of the decay tunnel the remaining hadrons hit a huge block of carbon and iron, which absorbs everything except the neutrinos and muons. The deposited energy is so high that a closed-circuit water cooling system is needed to prevent a meltdown.

The neutrinos continue their way towards Gran Sasso, while the remaining muons are completely absorbed by the earth's crust within a kilometer. The muons provide an easy way to measure the angle and position of the beam. For that two muon detection stations are installed, one right after the beam-stop, the other one 67 meters downstream in the beam. These muon detectors provide indirectly the only information about the neutrino beam before it reaches the Gran Sasso tunnel in Italy.

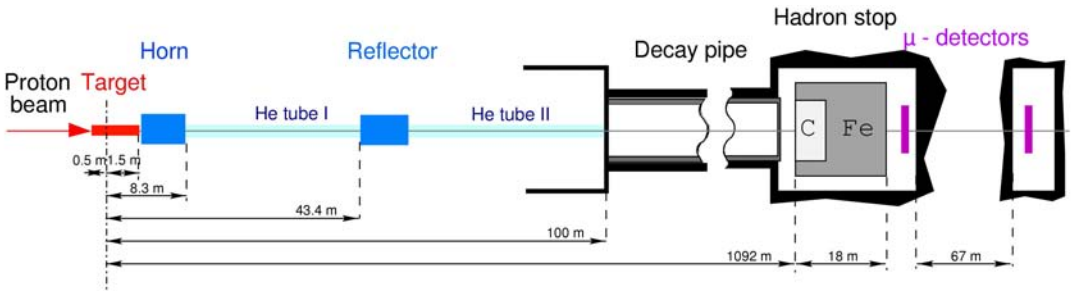


Figure 3.1: General layout of the CNGS beam

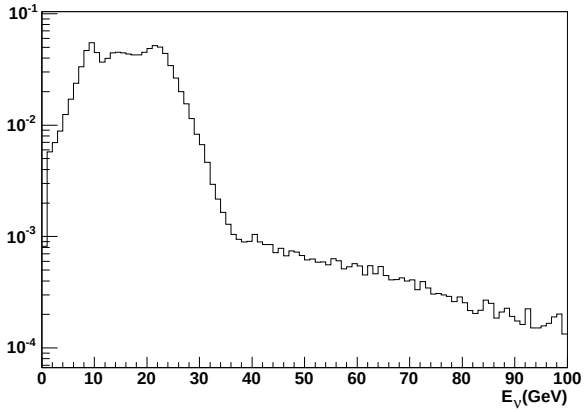


Figure 3.2: Energy distribution of $\nu_\mu$'s in the CNGS beam, the mean energy is 17 GeV

The CNGS beam contains mainly muon neutrinos but a small contamination of other neutrino flavors can not be avoided. The ratio of $\bar{\nu_\mu}$'s will be about 2% and the contribution of electron- and anti-electron neutrinos will be less than 1%. The intensity of the beam with $4.5 \times 10^{19}$ protons on target per year is expected to be $7.45 \times 10^{-9}/m^2/pot$ or $3.5 \times 10^{11}\ \nu/m^2/year$ with the mean energy of 17 GeV well above the $\tau$ production threshold. In terms of neutrino interactions in the OPERA detector at Gran Sasso this means about 30 events per day. The number of $\tau$ neutrinos detected depends strongly on the oscillation parameters. Calculated with $\Delta m^2 = 2.4 \times 10^{-3} eV^2$ and full mixing ($\sin^2 2\theta = 1$) we expect about 15 $\nu_\tau$CC interactions detected during a five year run.

## 3.2 LNGS

The INFN-LNGS underground laboratory is located at 120 km from Rome in the Gran Sasso road tunnel on the free-way Roma-Terramo. This is the longest road tunnel with

two tubes in Europe with a length of 10 km. The laboratory is under a 1400 m rock overburden which reduces the cosmic muon flux to $10^{-6}\ /m^2/h$, making it an ideal place for low background experiments. The placement of the OPERA detector inside the underground laboratory is shown on Fig. 3.3.

The ground level facilities of the LNGS laboratory have an equally important role in the experiment. The ECC Bricks (see below) after being extracted will be exposed to cosmic rays in a specially designed pit and right after developed, in a building specially built for the OPERA experiment. Around ten scanning stations will be installed for Changeable Sheet scanning and the laboratory will host the database containing the data of the electronic detectors.

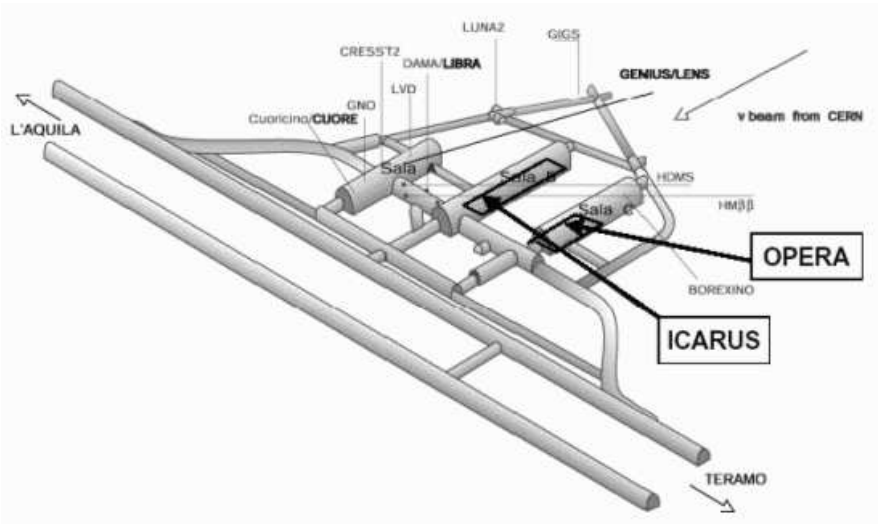


Figure 3.3: The experimental hall and the location of the OPERA detector in the Gran Sasso tunnel

## 3.3 The Detector

As we can see on Fig. 3.4 the detector consists of two identical “super-modules” each with a 900 t target mass. The basic unit of the detector is the so called Emulsion Cloud Chamber (ECC). 57 photographic emulsions interleaved with 1 $mm$ thick lead plates and are packed together in an ECC “Brick”. The Bricks are tightly and hermetically packed with aluminum-coated paper closed with thermo sealing. The Brick packing will be fully automatized, the so called Brick Assembly Machine (BAM) will produce perfectly aligned, controlled quality Bricks at a rate of 1000 per day, in the loading phase of the detector.

The Bricks are piled up in 31 walls in each of the two super-modules. In total 206336 Bricks are needed to fill the detector. Right behind each Brick-wall a so-called

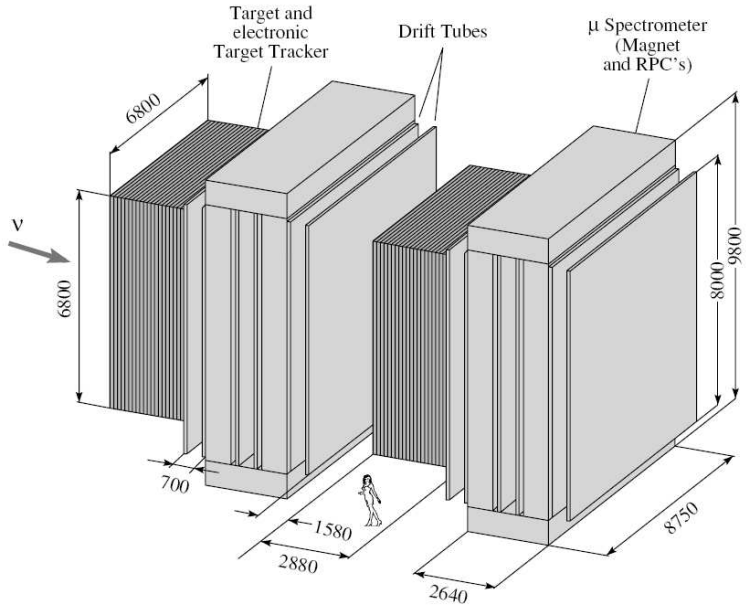


Figure 3.4: The OPERA detector

"Target-Tracker" wall is inserted. Each Target Tracker contains 4 x 64 scintillator strips placed vertically as well as horizontally (for details see [39]). At each end of the Target Tracker modules 64 channel photomultipliers collect the light providing information about the position of passing through charged particles.

Each super-module has a muon-spectrometer. They consist of dipolar magnets made of two iron walls interleaved by pairs of high resolution trackers. Each magnet is composed of 5 cm thick 2 x 12 iron slabs. A current of about 1.2 kA produces a magnetic field of 1.55 T in the iron. The 2 cm space between each slab is occupied by RPC detector planes.

## 3.4 Electronic detectors

The Target Trackers provide the x and y coordinates of each hit with about 1 cm resolution. The hits from the on-board electronics of each plane are collected via an Ethernet network to a central computer and events are reconstructed to determine the exact location of the interaction. A display of a simulated event is shown on Fig. 3.5. It is not easy to find out in which Brick exactly the interaction happened. Sophisticated Brick-finding algorithms are applied to extract the right Brick from the wall with about 90% efficiency.

High energy muons produced in neutrino interactions will cross the whole detector passing through the magnets of the muon-spectrometer. The RPC planes inside the magnets will provide the spatial resolution necessary to use Multiple Coulomb

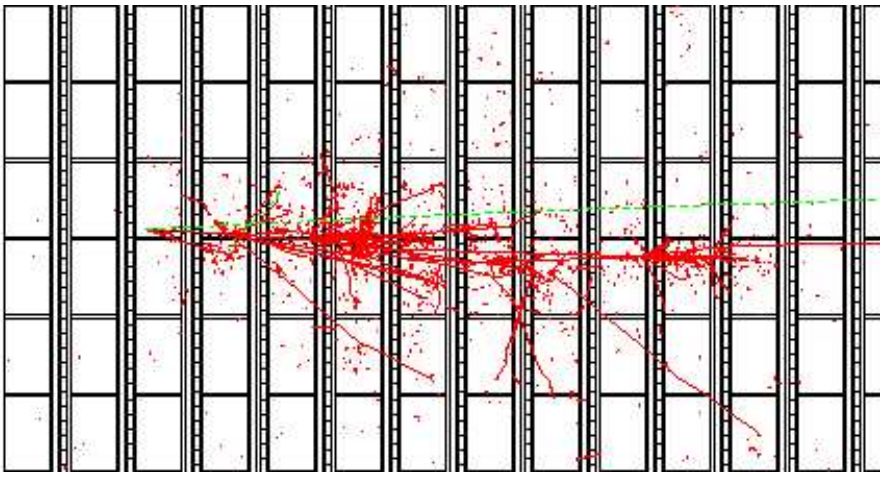

Figure 3.5: Simulated $\tau \rightarrow \mu$ event in the OPERA target. The beam comes from the left and the interaction occurs in the third Brick wall. The muon track corresponds to the longest track escaping on the right.

Scattering together with the bending of the track in the magnetic field to measure the momenta of the muon tracks with high precision. The deviation of the muon in the magnetic field will also define the charge of the particle. Figure 3.6 shows the cross-section of a spectrometer. On the two sides of the magnet precision trackers measure the coordinates of muon hits. Precision trackers are composed of 8 m long vertical drift-tubes surrounded by two layers of high precision RPC's. The spatial resolution of 0.5 mm of the precision tracker allows a momentum measurement with a resolution of about 25%.

## 3.5 The ECC Brick

The basic unit of the OPERA detector is the so-called Emulsion Cloud Chamber (ECC), a pile of photographic emulsions with lead plates in between. The sensitive part are the emulsions, which offer a spatial resolution of a few microns. The total area of emulsion films in the OPERA detector is about $\sim 176000\,\mathrm{m}^2$, which corresponds to $18\,\mathrm{m}^3$ of dried emulsion gel. Contrary to previous experiments like CHORUS and DONUT ([14, 15]) where the emulsions were poured by hand, the OPERA emulsions will be made by industrial methods, by commercial photographic film production lines. The detailed structure of an emulsion film is shown on Fig. 3.7. As we can see there is a 50 $\mu m$ emulsion layer on both sides of a plastic base. Thanks to the industrial methods the thickness of the emulsion is very well under control and after development, the thickness variation is within $\pm 2\,\mu m$, which is important for the precise track reconstruction.

The typical crystal diameter in the emulsions is about $0.02\,\mu$m which implies an

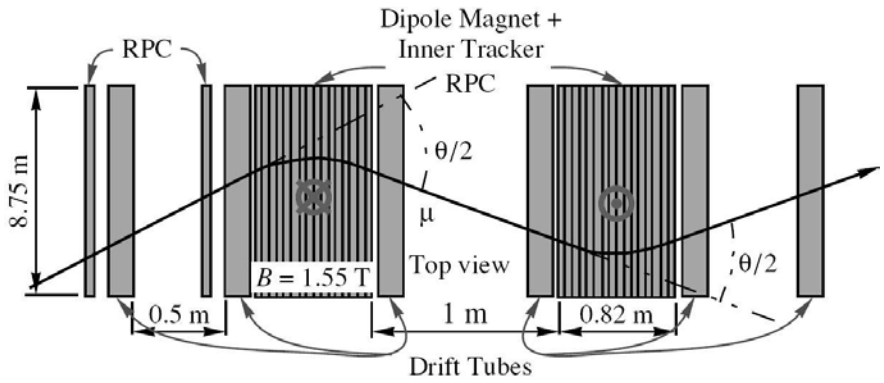


Figure 3.6: The OPERA muon-spectrometer

intrinsic resolution for the position of a passing through track as low as $0.06\,\mu$m.

57 emulsions with 56 lead plates are tightly packed together forming an ECC "Brick". The Bricks are hermetically closed to preserve the optimal humidity conditions for the emulsions. At the end of each Brick there are two additional emulsion sheets attached externally, in such a way that they can be removed without dismantling the Brick. The so-called Changeable Sheets (CS) will be developed underground and analyzed in the Gran Sasso laboratories. They will help to localize neutrino interactions reducing significantly the scanning load. If the Changeable Sheets confirm an interaction in a Brick, those Bricks will be moved at ground level where they are exposed to cosmic rays. High energy cosmic muons crossing the Brick provide straight tracks for inter-calibration of the emulsion plates. The required track density for precise alignment is $\sim 1$ per mm$^2$. The cosmic ray exposure will take place in a specially designed pit covered with 40 cm thick iron plates to reduce electron and low energy particle contamination. Then the Bricks will be dismantled and developed with the help of semi-automatic machines.

After the development, similar to normal photographic emulsions, they are sent to the scanning laboratories across Europe and Japan where they are scanned with automatized microscopes.

## 3.6 The European Scanning System

The European Scanning System (ESS) is based on commercially available hardware components. The optical tube of the microscopes contains standard optics produced by Nikon. They are equipped with a high resolution (Mega pixel) and fast (up to 500 fps) digital cameras. A high precision translator actuated by a stepping motor moves the optical tube up and down and the same type of translators move the target (the emulsion sheet) in the focal plane in the x and y directions. The camera is connected

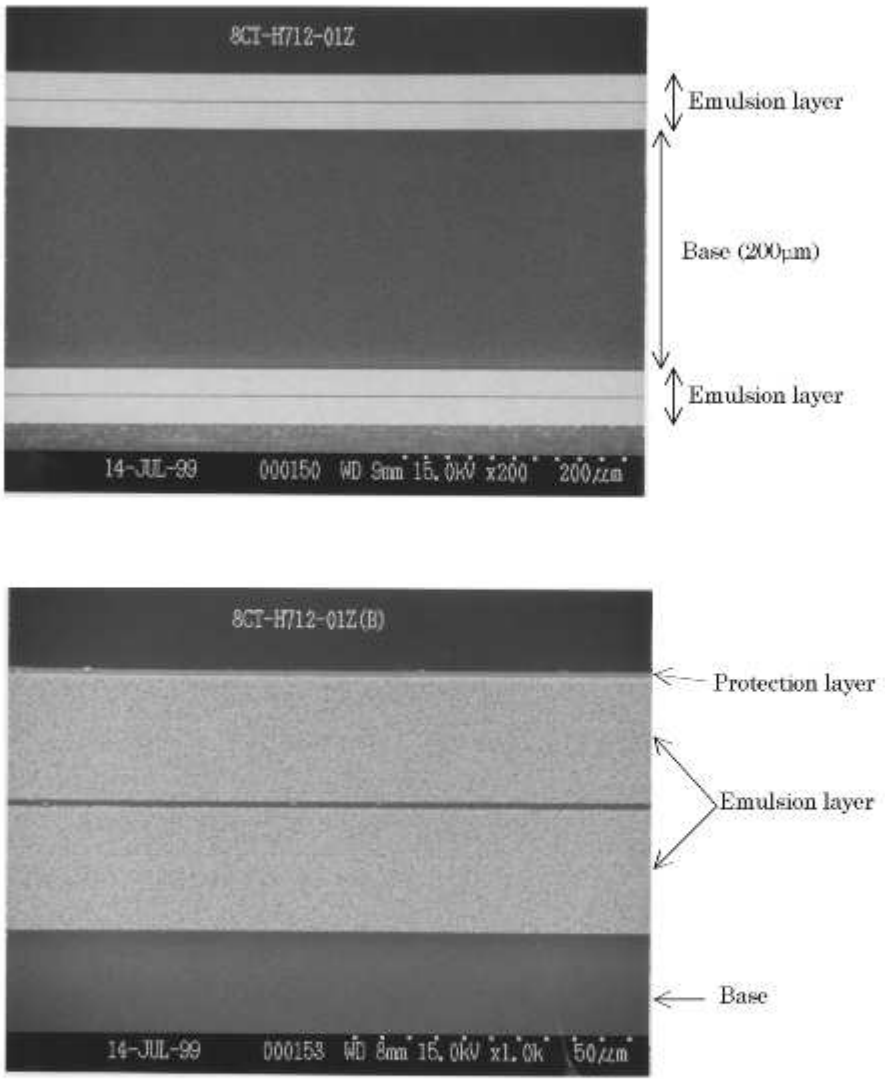


Figure 3.7: Cross section of an emulsion film

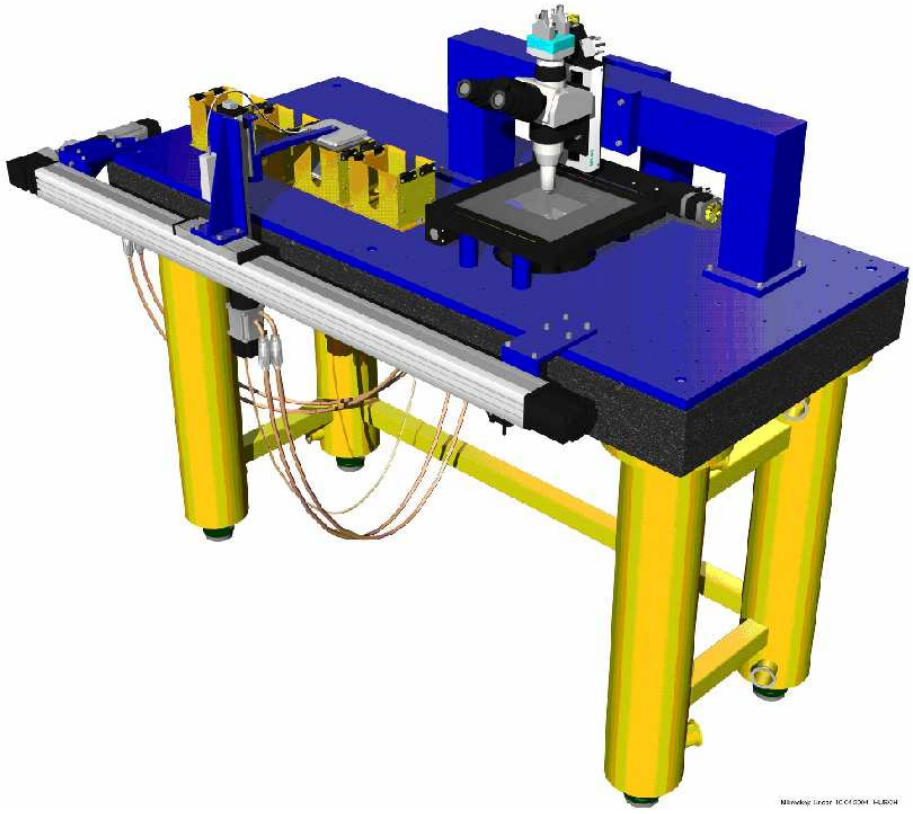

Figure 3.8: The microscope with the automatic plate changer

to a Matrox Odyssey image processor.

Gradually moving down the microscope, each emulsion layer is sliced in 16 tomographic layers defined by the focal depth of the microscope. The software running on the processor of the Matrox card selects the grains and passes their pixel wise coordinates to the main scanning software (SYSAL [38]) developed in Salerno. From the grains 3D micro-tracks are reconstructed as schematically shown on Fig. 4.1. The output of the scanning system are these micro-tracks. In the case of bulk "volume scan", from this point on the analysis is continued off-line. In order to deal with the large quantity of extracted Bricks, a scanning speed of 20 $cm^2$/h is needed. Several European laboratories already reported to have achieved this speed [41, 40]. Even with this speed, microscopes have to work continuously to deal with the large amount of extracted Bricks. To keep the microscope running around the clock, automatic plate changers are installed. Fig. 3.8 shows the microscope mounted on a scanning stage together with the plate changer developed in Bern. 4-5 of these systems are already fully operational.

## 3.7 Scanning strategies, data-storage

For the European Scanning System two different scanning strategies are forseen. The main strategy is called scan-back and consist in following the tracks upstream in the Brick, starting with the prediction based on the Changeable Sheet analysis. The advantage of this method is the high scanning speed, since only one view (~300 x 300 $\mu m$) per track per emulsion is scanned. For each track found, a prediction is made for the next plate and a base-track is searched for in one view around the indicated position. If the track is found it is followed until a stopping-point. A track came to a stopping-point if the predicted base tracks are not found in three consecutive plates. Every stopping-point is a vertex candidate. To find the other tracks probably belonging to a vertex, a larger volume is scanned around the stopping-point: 5 plates after and 4-5 plates before, with a surface of 25 $mm^2$. Unfortunately this method can not provide all the data needed for full event reconstruction. The other possible scanning strategy is the so-called volume-scan were a full volume inside the Brick is scanned. Volume-scan of a whole Brick (56 x 100 $cm^2$) with the current scanning speed would take about one month, which is obviously not feasible. In the moment of writing this document, the official scanning strategy is the scan-back method with a volume-scan in the region of the stopping-point, found by the scan-back. Another possibility would be a full on-line event reconstruction. This possibility is currently under investigation and experimental algorithms are tested.

To have a unified data format accessible for everybody in the collaboration, the data will be filled in an ORACLE database. The scanning software (SYSAL) interacts directly with the database and all the on-line and off-line analysis can be done with the database. The smallest unit of the data stored are micro-tracks, leaving the possibility for off-line reconstruction and search for interactions ($\tau$-decays) inside the plastic base.

## 3.8 Physics goals

The OPERA experiment is designated to the $\nu_\mu \rightarrow \nu_\tau$ oscillation search. It is an appearance experiment which will detect $\nu_\tau$ neutrinos appearing in a $\nu_\mu$ beam. The detection of $\tau$ neutrinos is not trivial since until now only four $\tau$ neutrinos were detected in the DONUT experiment [13].

The zenith angle dependence of the atmospheric neutrinos ($\nu_\mu$) observed in the Super-Kamiokande experiment indicates that $\nu_\mu$ oscillates into some other flavor. Since the CHOOZ experiment [16] set very tight limits on the $\nu_\mu \rightarrow \nu_e$ oscillation ($\theta_{13} < 10^o$), we expect to see $\nu_\tau$'s appearing in a $\nu_\mu$ beam. OPERA is supposed to measure the oscillation parameters around the region indicated by the Super-Kamiokande experiment (Fig. 3.9).

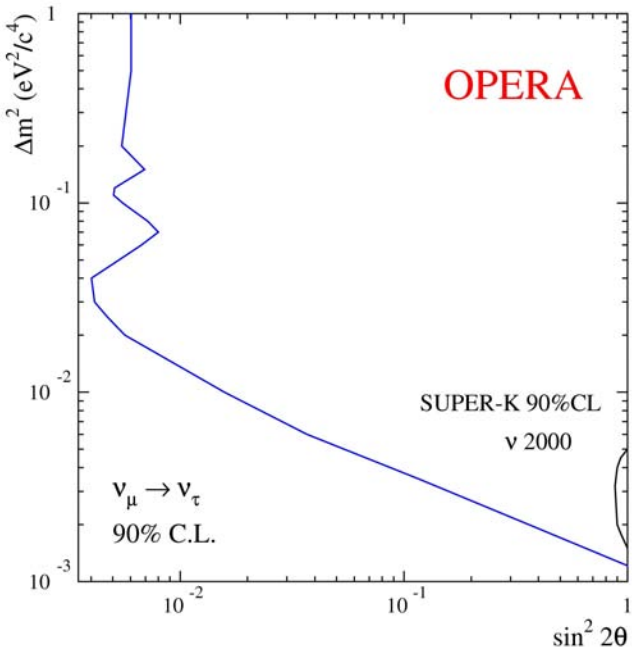


Figure 3.9: OPERA sensitivity for $\nu_\mu \rightarrow \nu_\tau$ oscillations. Exclusion plot in the absence of a signal.

### 3.8.1 $\nu_\mu \rightarrow \nu_\tau$ search

$\nu_\tau$ search is based on the observation of the decay of the $\tau$ lepton. Since neutrinos can take away a significant part of the momentum, the decay of a $\tau$ into a charged particle and neutrinos will appear in the ECC Brick as a "kink" (shown on Fig. 3.10). With the excellent spatial resolution of the emulsions, the kink will be visible and the daughter particles can be separated from the ones coming from the primary interaction. Since $\tau$'s are shortlived particles, with a mean lifetime of 295 femto-seconds, the mean decay-length in the laboratory frame is about a millimeter (depending on the $\tau$ momentum). Because of the internal structure of the ECC Bricks, only about 40% of the $\tau$ decays can be directly seen in the emulsions. These are the so called long decays. They are detected measuring the angle difference of the $\tau$ and the daughter track (see Fig. 3.11).

If the $\tau$ decays in the same plate where the interaction occurred, the kink can not be seen. However some short decays can be recovered using the Impact Parameter (IP) method. The Impact Parameter is defined as the 3D distance between the supposed daughter track of the $\tau$ and the primary vertex as shown on Fig. 3.12. Due to the good resolution of the vertex position, tracks with an IP of a few microns can be separated from the primary vertex.

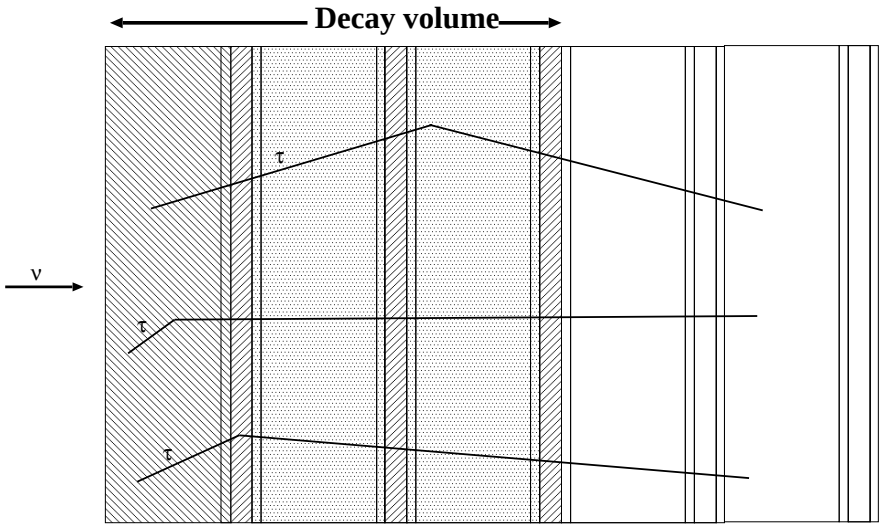


Figure 3.10: Definition of long- and short decays in the ECC Brick

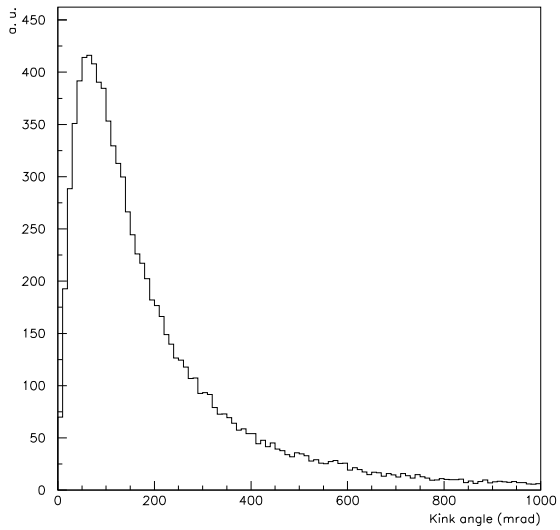


Figure 3.11: Kink angle in $\tau$-decays

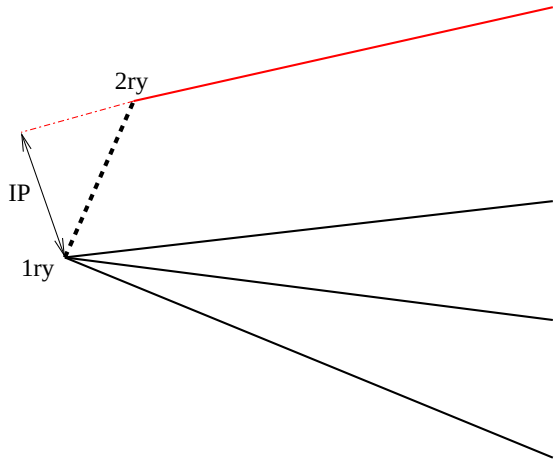


Figure 3.12: Definition of the Impact Parameter. The IP can be calculated for all the tracks attached to the vertex in a similar way

For $\tau$ search all possible decay modes are considered:

$$\begin{aligned} \tau^- &\rightarrow e^-\nu_\tau\bar{\nu_e} \\ \tau^- &\rightarrow \mu^-\nu_\tau\bar{\nu_\mu} \\ \tau^- &\rightarrow h^-\nu_\tau(n\pi^0) \end{aligned}$$

Each of these decay channels needs specialized analysis and background suppression.

For the $\tau \rightarrow e$ channel a good electron identification algorithm is needed. At the present we can achieve about 90% efficiency above 3 GeV. To reduce the background from low energy electrons ($\gamma \rightarrow e^+e^-$) we require the $\tau$ daughter to have an energy above 1 GeV but not higher than 15 GeV. The 1 GeV cut is needed to remove soft gammas originating from some other interaction and the upper cut is needed to suppress background from $\nu_e$CC interaction, coming from beam contamination or $\nu_\mu \rightarrow \nu_e$ oscillation. To further reduce this background a 100 MeV cut is applied on the transverse momenta of the electron.

The most important background for the $\tau \rightarrow \mu$ channel comes from large angle scattering of a muon produced in $\nu_\mu$CC interactions. About 0.5% muons produced in $\nu_\mu$CC interactions show an apparent kink in the lead plate downstream of the vertex plate. A cut on the transverse momenta of 250 MeV is forseen to suppress it and in addition only muons with momenta in the range of 1 - 15 GeV are accepted. The lower cut in the momentum is needed because of poor muon identification below 1 GeV and the upper cut reduces the probability of muon scattering.

The $\tau \rightarrow h$ channel has the largest branching ratio but suffers from the background coming from the re-interaction of the hadrons from $\nu_\mu$NC events. Re-interacting hadrons from $\nu_\mu$NC and from $\nu_\mu$CC events with the muon not identified can mimic the $\tau$ kink. To suppress the background from hadronic re-interactions initially the

| Decay mode | DIS long (%) | QE long (%) | DIS short (%) | Total (%) |
|---|---|---|---|---|
| $\tau \rightarrow e$ | 2.7 | 2.3 | 1.2 | 3.4 |
| $\tau \rightarrow \mu$ | 2.4 | 2.5 | 0.7 | 2.8 |
| $\tau \rightarrow h$ | 2.8 | 3.5 | - | 2.9 |
| Total | 8.0 | 8.3 | 1.9 | 9.1 |

Table 3.1: $\tau$ detection efficiency for different $\tau$ decay modes, topologies and type of events (source [33]).

| channel | $\Delta m^2(eV^2)$ | | | Background |
|---|---|---|---|---|
| | $1.6 \times 10^{-3}$ | $2.5 \times 10^{-3}$ | $4.0 \times 10^{-3}$ | |
| $\tau \rightarrow e$ long | 1.4 | 3.4 | 8.6 | 0.15 |
| $\tau \rightarrow \mu$ long | 1.3 | 3.2 | 8.1 | 0.29 |
| $\tau \rightarrow h$ long | 1.6 | 3.7 | 9.4 | 0.23 |
| $\tau \rightarrow e$ short | 0.4 | 1.0 | 2.5 | 0.03 |
| $\tau \rightarrow \mu$ short | 0.2 | 0.5 | 1.3 | 0.04 |
| Total | 4.9 | 11.8 | 30.0 | 0.74 |

Table 3.2: Expected numbers of $\tau$ events and background during a 5 year run for different $\Delta m^2$ values (source [33]).

following cuts were forseen: $P > 2\,\text{GeV}$, $P_t > 600\,\text{MeV}$. This background can be further reduced by applying cuts on the angle between the parent track and the showers momentum and the missing transverse momentum at the primary vertex. The effect of these cuts using a simulated interaction rate as a function of momenta is discussed in more detail in Chapter 5.

In addition, in Chapter 5. we study the detection efficiencies for the decay channels with neutral pions ($\tau \rightarrow \pi(n\pi^0)$) originally not considered in the experiment proposal [32]. Since the decay length of $\pi^0$'s is very short, they can be detected by tagging $\gamma$'s to the secondary vertex.

In table 3.1 we summarize the detection efficiencies for different topologies and event types. The total number of expected events during a 5 year run in the OPERA detector is given in table 3.2. This numbers are reevaluated continuously in function of changing parameters and improving analysis methods.

### 3.8.2 $\nu_\mu \rightarrow \nu_e$ search

Since the ECC Brick structure allows a very good electron identification, and because of the very low contamination with $\nu_e$'s of the beam, there is hope to measure the oscillation parameters for the $\nu_\mu \rightarrow \nu_e$ oscillation bellow the limit set up by the CHOOZ experiment.

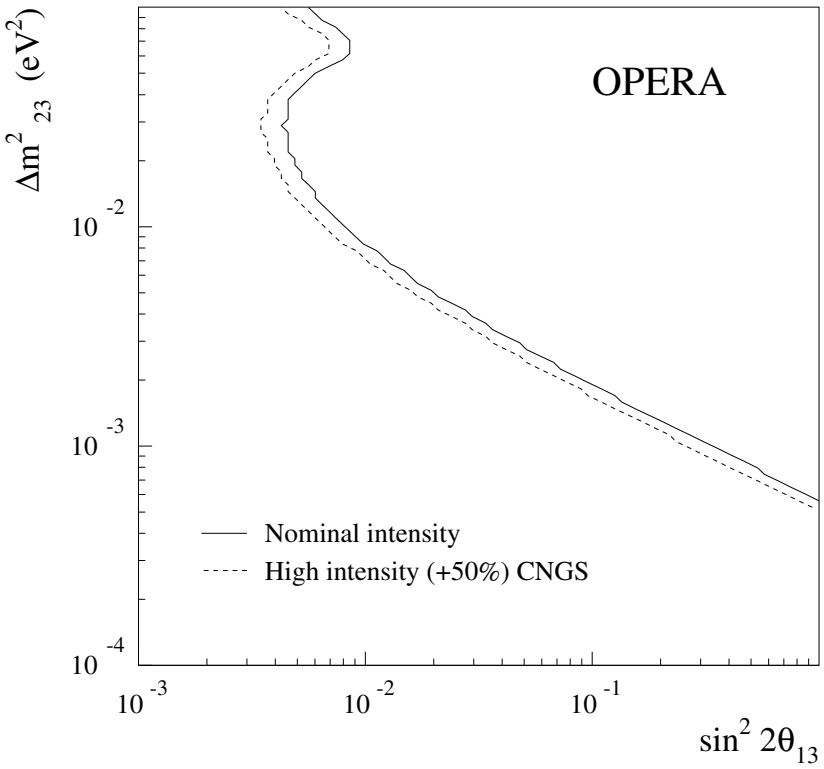


Figure 3.13: OPERA sensitivity for $\nu_\mu \rightarrow \nu_e$ oscillations

Background is mainly coming from $\nu_\mu$NC interactions where $\pi^0$'s are produced. $\pi^0$'s decay in $\gamma$'s. To suppress low energy gammas we will not accept events with the primary vertex momenta lover than 1 GeV. Similarly vertices with momenta higher than 20 GeV will be rejected to suppress the signal of $\nu_e$ coming from the beam. Figure 3.13 shows the preliminary estimate for OPERA sensitivity to $\nu_\mu \rightarrow \nu_e$ oscillation, evaluated in [35].

# Chapter 4

# Analysis tools and methods

Before proceeding with the analysis, it is necessary to present the software tools developed specifically for OPERA. I will also review briefly some of the methods the analysis algorithms are based on.

## 4.1 Track Reconstruction

Once the emulsion plates are scanned, the data is converted into ROOT files containing the so-called "Edb" data structure. The raw data containing micro-tracks is processed with the help of a software library called FEDRA developed by the Naples group [44, 45]. FEDRA stands for Framework for Emulsion Data Reconstruction and Analysis and is based on the ROOT analysis framework.

The reconstruction of the tracks is done in the following steps (see [45]):

- Micro-track linking: A micro-track is defined by a series of clusters. The connection of the clusters is done by the scanning software SYSAL. Micro-tracks found in the top and bottom layer of the emulsion sheets have to be connected. The two micro-tracks are fitted with a line and form a base-track. To achieve $\mu m$ resolution the off-line reconstruction has to correct for shrinkage and distortion. Shrinkage is due to the reduction of the thickness of the emulsion after the development process. The shrinkage factor is given by the ratio of $\frac{microtrack\,angle}{basetrack\,angle}$. Correction is applied to the $z$ thickness of the emulsion layer until the ratio is close to 1.
  Distortions are local deformations of the emulsion and can smear the angle of a micro-track up to several mrad (see Fig. 4.2). Fortunately, the plastic base is practically free of distortions. Hence defining the base-track angle with the two closest point on the two sides of the base, we can achieve a resolution between 1 and 2 mrad. In the further steps of the analysis only these base-tracks are used.

- Alignment of the emulsion sheets: emulsion sheets are aligned two-by-two using

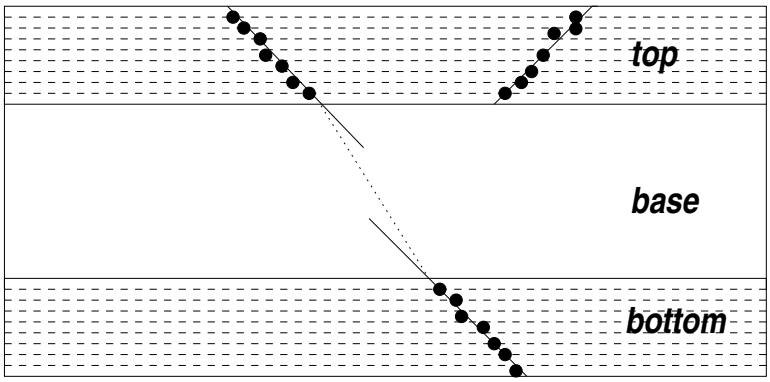


Figure 4.1: Base-track reconstruction starting with grains found in tomographic layers seen by the microscope. The difference between the micro-track angles and base-track angle shows the effect of the shrinkage.

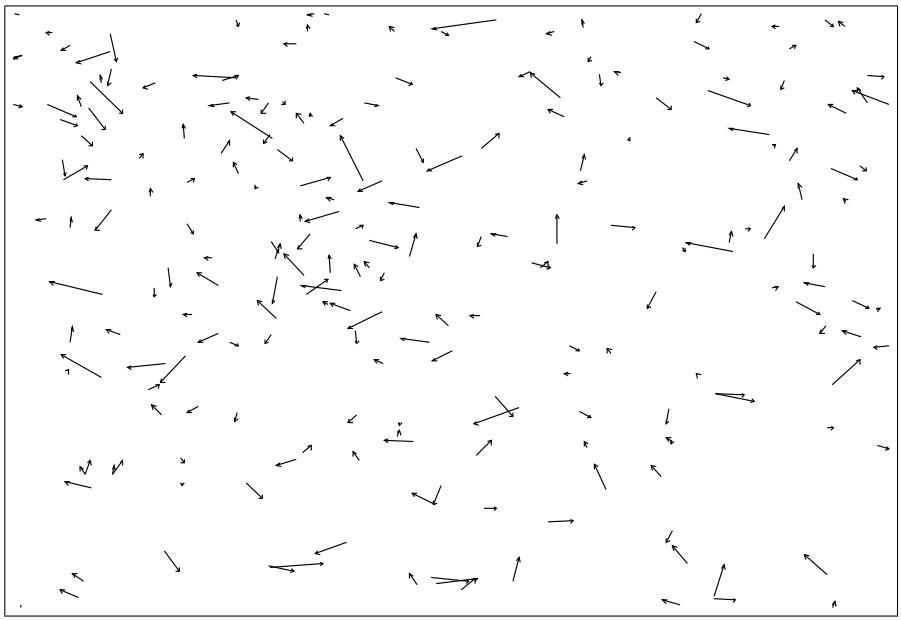

Figure 4.2: Typical distortion map of an emulsion. The arrows represent the difference between the micro-track and the base-track angle. This particular emulsion comes from a 2004 CERN test-beam Brick

the base-tracks. The alignment procedure returns an affine transformation (a rotation and a translation) for each sheet. The transformation is parameterized in the following way:

$$\begin{pmatrix} X' \\ Y' \end{pmatrix} = \begin{pmatrix} a_{11} & a_{12} \\ a_{21} & a_{22} \end{pmatrix} \begin{pmatrix} X \\ Y \end{pmatrix} + \begin{pmatrix} b_1 \\ b_2 \end{pmatrix}$$

- Track linking: base-tracks are connected to form a volume-track. Base-tracks are grouped according to angular and position acceptance. From many possible connections, the tracks are selected based on a $\chi^2$ cut. These collection of base-tracks serves as trigger for starting the track fitting with the Kalman filter (see Section 4.4).

- Track propagation: due to a scanning efficiency inferior to 100%, we have to reconstruct tracks with missing base-tracks as well. Tracks are followed through one ore more plates (usually up to three) and if base-tracks or tracks are found they are merged with the original track. After, the Kalman filter is used for smoothing.

After tracks are successfully reconstructed, we can proceed with the kinematical analysis of the interactions.

## 4.2 Monte-Carlo Simulation

For tuning and testing the analysis tools we developed a simulation tool, based on Geant4 [42]. The advantage of using Geant4 (over Geant3) is the possibility to use new hadronic models and the C++ language with Object Oriented design, which makes it easy to interface with ROOT [43] the standard analysis framework.

The simulated geometry consists of only one ECC Brick, since this is the part of the OPERA detector where most of the interactions take place. We can use the simulation in single particle mode for test-beam simulations or interfaced with the NEGN neutrino generator [48]. NEGN was derived from the event generator developed for the NOMAD experiment. It is based on JETSET 7.4 and produces a simple text output. The interface developed in Neuchâtel reads in the output of NEGN, transforms Geant3 particle codes in the Geant4 (PDG) standard and generates the particles from the neutrino interaction in the standard UserPrimaryGeneratorAction class of Geant4.

The generated output can be used directly for analysis or is processed with a simple ROOT script to generate base-tracks for FEDRA reconstruction. Angle dependent Gaussian smearing is added to the base-tracks to reproduce the effect of the measurement error. Later, the simulation was updated to produce the required input for the

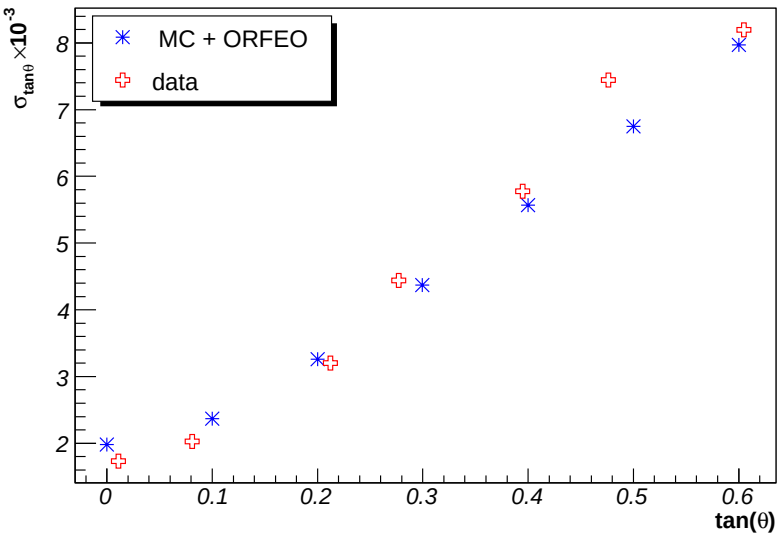


Figure 4.3: Measurement error on the angle in function of the track angle in MC smeared with ORFEO versus real data (errorbars are smaller than the points)

ORFEO package [47]. ORFEO simulates the measurement error in one plate and the error of the alignment as well. Adding background from real data is also possible. Simulated events with smearing added and after the standard reconstruction can be hardly distinguished from real data. The scanning efficiency is simulated as well by removing some of the base-tracks.

One important feature of the real data is that the measurement error depends on the angle of the incident particles. This is a problem related to the optical microscope and cannot be avoided. The angular dependence is simulated by ORFEO, smearing the z coordinates of the micro-track. To reproduce exactly the properties of the real data I tuned the parameters of ORFEO until the angle dependence of the angular resolution matches the real data (see Fig. 4.3) .

The simulation tool is available on our web-page:
http://www.unine.ch/phys/corpus/OPERA/opera.html.

## 4.3 Momentum measurement

The indispensable ingredient of the kinematical analysis is the momentum measurement. The momentum of a charged particle can be estimated from its multiple scattering. Due to Multiple Coulomb Scattering (MCS) a particle traversing a medium with thickness $x$ will be deflected by many small-angle scatters. The distribution of the scattering angle is given by the Moliére distribution. If we consider only small an-

gle deflections, the distribution can be approximated by a Gaussian. The RMS of the scattering angle can be expressed in terms of particle momentum $P$, radiation length $X_0$ and thickness of the traversed material $x$ with the formula:

$$\theta_0 = \frac{13.6\,MeV}{\beta cp}\sqrt{\frac{x}{X_0}}\left(1 + 0.038\ln\left(\frac{x}{X_0}\right)\right) \tag{4.1}$$

were $\theta_0$ is the RMS of the scattering angle in one plane projection

$$\theta_0 = \theta_{plane}^{rms} = \frac{1}{\sqrt{2}}\theta_{space}^{rms}$$

According to [9], the Gaussian approximation is accurate to 11% or better for $10^{-3} < x/X_0 < 100$.

Measuring the momentum of a particle with MCS is possible with two methods: position and the angle method. In the position method we calculate the scattering angle $\theta_M$ from the positions of consecutive base-tracks:

$$\theta_M = \frac{\Delta x}{L}$$

where $\Delta x$ is the displacement over a cell length $L = 1300\,\mu m$. This method depends strongly on the alignment accuracy of the emulsion sheets which makes it difficult to use.

The second method is the angle method: we calculate the scattering angle from the difference of two consecutive base-track angles, which is independent of the alignment error (see fig 4.4). The maximal momentum that can be measured with the angle method can be estimated from the intrinsic resolution of the emulsions. According to [32], the intrinsic angular resolution of an emulsion sheet is $\delta\theta = 0.4$ mrad (0.8 mrad is the maximal error on the difference of two base-tracks). Using the formula 4.1 one can easily calculate that the highest momentum that can be measured by this method is about 7 GeV/c. Furthermore, assuming a more realistic angular resolution of 2 mrad we get $P_{max} < 3$ GeV. Measurements of the angular resolution on test-beam data give a resolution of 1.7 mrad for small angle tracks and up to 8 mrad for large angles (see Fig. 4.3). This means in the best case a limit of 3.4 GeV for the maximal momenta that can be achieved with the simple method. In the light of this numbers the measurements of high energy particles above 4 GeV seems unrealistic, even when increasing the number of measurements (see below).

The brick consist of 56 emulsion layers. That means 110 independent measurement for passing through tracks (x and y projections we assume to be independent) which is usually not the case. Normally, we have to deal with shorter tracks and tracks containing holes (missing base-tracks). It is important to have the highest number of independent measurements possible to extract the maximum amount of information. To do this we will use the $ncell$ method described in [54, 55] and [56]. The scattering angle is measured from the difference of angles of two base-tracks separated not by

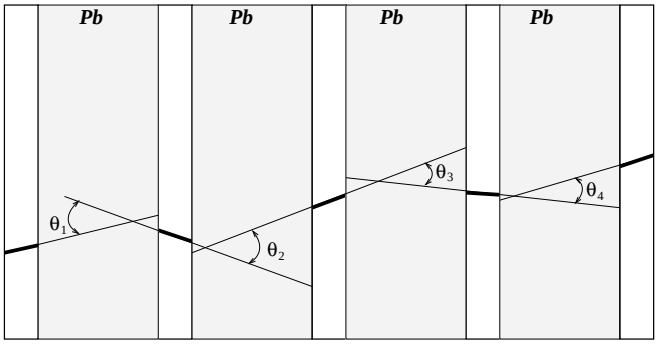


Figure 4.4: Calculating the scattering angle for the angle method

only one but up to several lead plates. All these measurements are not independent and this may cause problems when dealing with real data. Starting with the formula 4.1 we can safely neglect the log term (adds a correction of about ~3% ). Substituting $x = ncell \times 1\,\text{mm}$, $\beta \simeq 1$, $\theta_m^2 = \theta_0^2 + 2\delta\theta^2$ , where $\theta_m$ is the measured scattering angle, $\delta\theta$ the measurement error of the angle of one base-track, the formula becomes:

$$\theta_m = \sqrt{\frac{13.6^2 ncell}{X_0 P^2} + 2\delta\theta^2} \tag{4.2}$$

where $X_0 = 5.6\,\text{mm}$ the radiation length for lead.

The validity of the method first was tested with a Geant4 simulation. I simulated a test-beam situation, shooting pions at several energies in a Brick. To the simulated pion tracks, an angle dependent smearing was added, 1.7 mrad at 0 and increasing according to a function fitted to real data measurements (see Fig. 4.3).

The method described in [54, 55] consist in fitting the square-root function 4.2 to the scattering angle in function of $ncell$, the distance between the base-tracks. An example with a simulated pion track is shown on fig 4.5. In the first approach, the points are fitted with the standard $\chi^2$ method of ROOT where for minimization the MINUIT package is used. The first problem encountered is the convergence: if the points are scattered too much, the algorithm will not converge in about 5% of the cases for Monte-Carlo and can be up to 50% in the case of real data including short tracks with many holes (short tracks are the tracks with less than 25 segments).

Two different methods were compared: first the measurement error is a free parameter, in the second method, the measurement error is set by hand to some fixed value. The results for different momentum can be seen on Fig. 4.6. The obtained resolution with the measurement error as a free parameter is worst than when is fixed. Setting the measurement error to $\delta\theta = 2$ mrad and redoing the fit with only one free parameter, the obtained momentum resolution is in full agreement with [53, 54] but the mean of the momenta is systematically underestimated starting from 5 GeV. Tuning the value of $\delta\theta^2$ one can obtain a slightly underestimated momentum and an acceptable resolu-

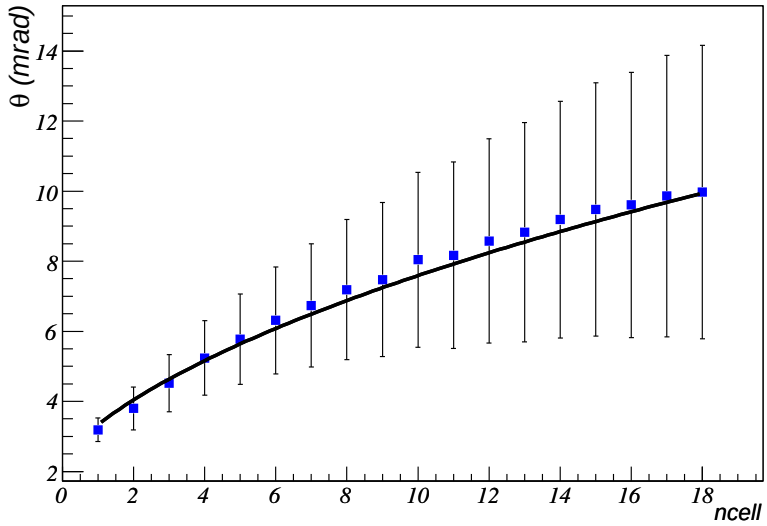


Figure 4.5: Mean base-track-angle difference in function of the number of lead plates crossed, for a simulated 2GeV pion track, fitted with the function 4.2

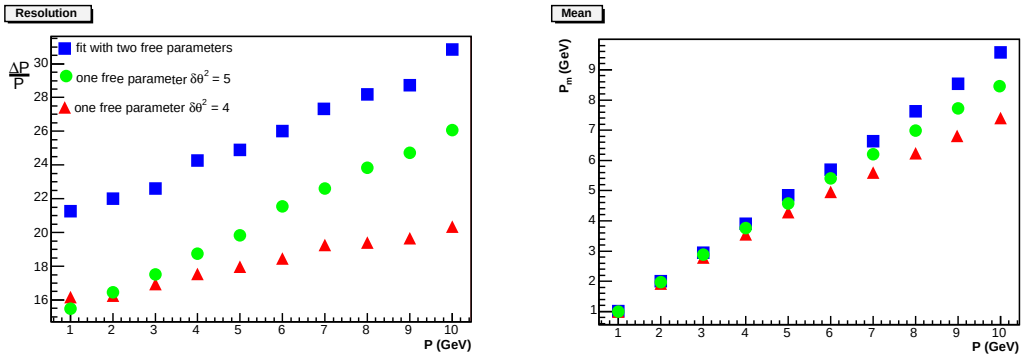


Figure 4.6: Momentum measurement of MC tracks with the $ncell$ method. Left: resolution, right: mean value of the estimated momenta

tion. Obtaining both a correct mean and the resolution claimed in [53, 54], it seems impossible to achieve. Estimating the resolution for each Brick, is not feasible since in OPERA conditions, the data contains only a few tracks with unknown momenta. In addition, the angular resolution is affected by local distortions (see section 7.2.1) and the resolution measured with one track in the most general case cannot be used for another track if they are more than 1 cm apart from each other. We will have to rely on general assumptions for the resolution. By consequence, the fit with two free parameters (momentum and measurement error) restricting the parameters to an interval, excluding non-physical results, it seems a practical solution. For the momentum the range is between 0.1 and 15 GeV and for the error 1 to 5 mrad. With good starting values the fit always converges and never returns non-physical values. For results with real data see section 6.5.

The plots shown above were done with MC data. In the case of real data, the obtained mean value for the momenta is much worst: for the 8 GeV test-beam data (see 7.13) the maximum probability value of the distribution is at 6 GeV only. Knowing that at 8 GeV the effect of MCS is much smaller than the measurement error (about 0.7 mrad for 1 mm lead), the maximal measurable momentum: $P_{max} < 6$ GeV. Performing the calculation backward, we get an angular resolution of 1.1 mrad, which shows clearly, that the ncell method exceeded the theoretical limit of the simple method but higher momentum tracks cannot be measured by this method.

## 4.4 Kalman filter

The Kalman filter is a set of mathematical equations that implement a predictor-corrector type estimator that is optimal in the sense that it minimizes the estimated covariance. The advantage of the Kalman filter over the usual least squares estimator is that there is no need to invert the covariance matrix with the dimension of the global state vector (which in the general case is non diagonal). Instead we have to invert matrices only with the dimension of the local state vector (the measurement vector). Track fitting is a quite similar problem to autonomous navigation: each track segment corresponds to a position measurement in time. Following the track, the Kalman filter predicts the next segment and calculates the error of the prediction. The application of the Kalman filter for track fitting is treated in references [49, 50, 51].

The Kalman filter is mathematically equivalent to the global fit when there is no multiple scattering or energy loss. The natural iterativeness of this procedure allows tracks to be fitted in pieces, track elements can be merged without redoing the whole fit. The Kalman filter uses all the information and cannot give worst track parameters by adding more measurements. For example, adding a point far from the vertex of a low energy track will have a small contribution because the multiple scattering error is large. By consequence, the Kalman filter (in this particular situation) is good at calculating track parameters at the beginning of the track and is less performant predicting the next hit.

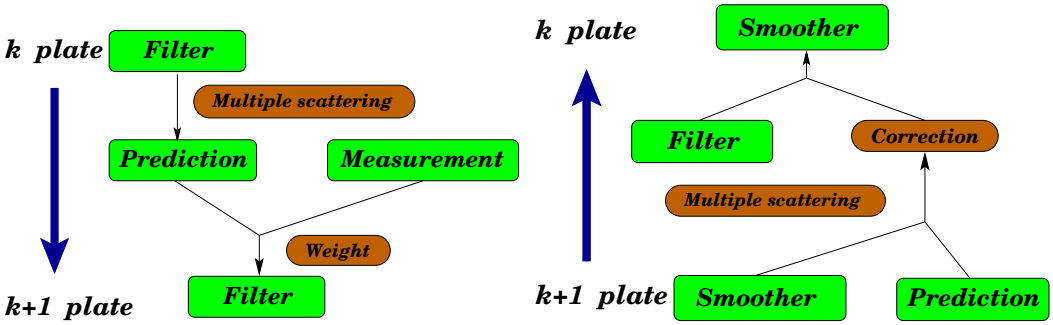


Figure 4.7: Kalman filter as used for track fitting and for smoothing

Accounting for multiple scattering can also be a disadvantage, because the fitted track parameters depend strongly on the momentum hypothesis. Overestimating the momenta of low energy tracks can give bad results.

There are different ways of using the Kalman filter:

- FILTERING is the estimation of the "present" state vector, based upon "past" measurements
- PREDICTION is the estimation of the present state vector at a "future" time.
- SMOOTHING is the estimation of the state vector at some time in the "past" based on all measurements taken up to the present time.

In our case (OPERA) the time parameter is replaced by the plate index. The state vector looks like: $\vec{x}_k = (X, Y, Z, TX, TY, P)$ , it's covariance matrix is $C_k$.

In the first step we make a prediction of the state vector at the position $k$ based on the state vector at $k-1$. The prediction equations are:

$$\vec{x}_k^{k-1} = F_k \vec{x}_{k-1} \qquad C_k^{k-1} = F_k C_{k-1} F_k^T + Q_k$$

were $F_k$ describes the propagation of the track parameters from the $k-1$ position to $k$. $Q_k$ is the process noise (multiple scattering in our case). The estimated residual

$$\vec{r}_k^{k-1} = \vec{m}_k - H_k \vec{x}_k^{k-1} \qquad R_k^{k-1} = V_k + H_k C_k^{k-1} H_k^T$$

were $H_k$ is the projection matrix, $\vec{m}_k$ the measured coordinates. The filter equations are:

$$\begin{aligned} K_k &= C_k^{k-1} H^T \left(V_k + H_k C_k^{k-1} H_k^T\right)^{-1} \\ \vec{x}_k &= \vec{x}_k^{k-1} + K_k \left(\vec{m}_k - H_k \vec{x}_k^{k-1}\right) \\ C_k &= \left(1 - K_k H_k\right) C_k^{k-1} \end{aligned}$$

with the filtered residuals

$$\vec{r}_k = \left(1 - K_k H_k\right) \vec{r}_k^{k-1} \qquad R_k = \left(1 - K_k H_k\right) V_k$$

$K_k$ is often called the gain matrix. The $\chi^2$ contribution of the filtered point is given by:

$$\chi^2_{k,F} = \vec{r}^T_k R^{-1}_k \vec{r}_k$$

The system state vector at the last filtered point contains the full information from all points. If one needs the full state vector at every point of the trajectory, the new information has to be passed upstream with the smoother equations

$$\begin{aligned} A_k &= C_k F^T_{k+1} \left(C^k_{k+1}\right)^{-1} \\ \vec{x}^n_k &= \vec{x}_k + A_k \left(\vec{x}^n_{k+1} - \vec{x}^k_{k+1}\right) \\ C^n_k &= C_k + A_k \left(C^n_{k+1} - C^k_{k+1}\right) \\ \vec{r}^n_k &= \vec{m}_k + H_k \vec{x}^n_k \\ R^n_k &= R_k - H_k A_k \left(C^n_{k+1} - C^k_{k+1}\right) A^T_k H^T_k \end{aligned}$$

In the current implementation in OPERA (Vt++ [46]), the full potential of the Kalman filter is not exploited. It is used only for track fitting but not for track finding (selecting base-tracks belonging to a track).

Using the Kalman filter for vertex fitting is based on the same principles as the track fitting: the vertex position is updated with each track added to the vertex. Again, in the simplest case it is the same as the least squares method. The real advantage of using the Kalman filter for vertex fitting is that momentum information can be added and the $\chi^2$ contribution of each track is directly known. On Fig. 4.8 the comparison between the Kalman filter and the least squares fit is shown, in the case when the momentum of the tracks is known.

### 4.4.1 Short decay search

Since the $\chi^2$ contribution of each track is known, the software implementation we use (Vt++), returns the track with the highest $\chi^2$ value. Redoing the fit with the remaining tracks, we can calculate the Impact Parameter of the removed track. Therefore the Kalman filter could be used, for example to find short decays or secondary vertices when they cannot be seen otherwise.

On Fig. 4.9 the Impact Parameter of the muon track in the $\tau \rightarrow \mu$ decay following a $\nu_\tau$ interaction is shown. From the total amount of $\tau \rightarrow \mu$ short decays 35% had $\chi^2 > 4$ (99.5% probability). These are the potential candidates for a short decay. I assume that the track with the highest $\chi^2$ contribution is the muon track. Only 10% cases happened that not the muon track was removed from the vertex. Therefore, with this method we can detect short decays with about 31% efficiency even when it is not possible to separate them based on the Impact Parameter.

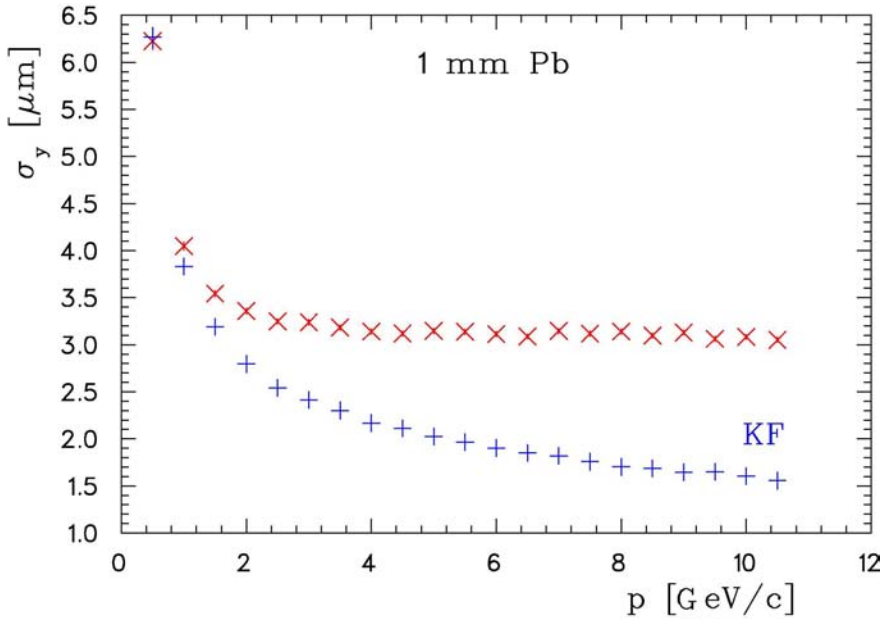


Figure 4.8: The comparison of the vertex position resolution with the Kalman filter and with the shortest distance method in the function of the momentum of the tracks.

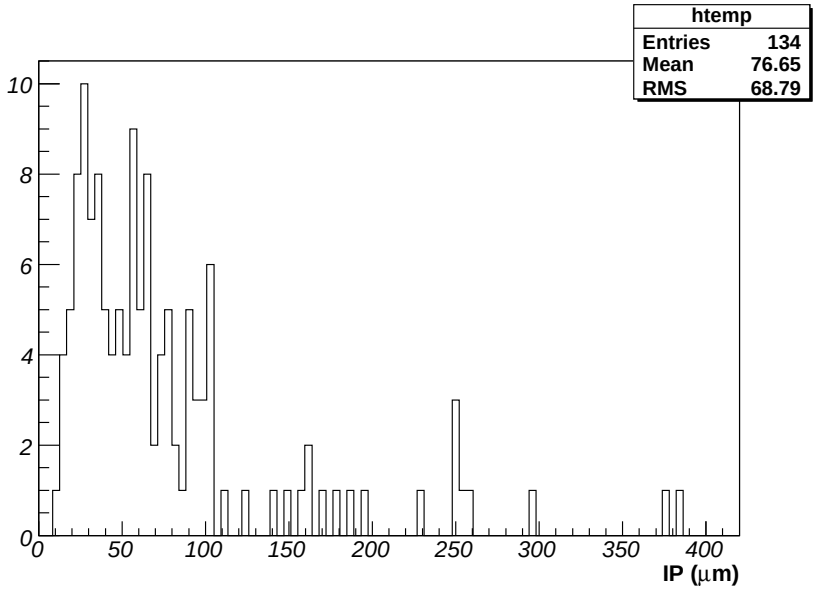


Figure 4.9: Impact Parameter relative to the primary vertex of muons from $\tau \rightarrow \mu$ short decays

## 4.5 Interactive display tool

For testing vertex finding algorithms it is inevitable to verify the results "by-hand", going through some events one-by-one, visually checking if the found events are real. I started writing a display tool that allows the visual and interactive analysis of interactions inside an ECC Brick. It is based on the ROOT graphical library and uses the FEDRA file format, therefore is a natural extension of the existing analysis tools. As shown on Fig. 4.10 one can select a file to be analyzed in the file-selector by clicking with the mouse. The content of the *tracks* tree is displayed using 3 projections x-z, y-z and x-y. The tracks are represented as a line defined by the base-track coordinates. Holding down the left mouse button one can zoom in one of the three panes and each zoom is automatically propagated to the other two projections ( a zoom in x-z implies a zoom of the z axis on the y-z projection and the zoom of the x axis on the x-y projection). A geometrical volume can be selected by specifying the coordinate region on the right-bottom pane.

Selecting some tracks with the right mouse button and clicking on the *Vertex* button one can directly see the parameters of the fitted vertex in a terminal window. Fitted vertices with the tracks attached will be automatically saved exiting the program. The output file contains the same *tracks* tree as the input with additional variables like the vertex coordinates, $\chi^2$ and a vertex ID. Files already containing the vertex ID or files with an *EdbPVRec*[1] object can be opened for event-by-event analysis.

During the development of vertex finding algorithms this simple application was extremely useful. It can be downloaded from the same web page as the simulation tool: http://www.unine.ch/phys/corpus/OPERA/opera.html.

## 4.6 Vertex reconstruction

The vertex search in OPERA is slightly different from the general problem. Which tracks to be attached to a vertex are usually a priori known. They are the tracks followed by the scan-back or the beam-tracks in the test-beam data. The problem is rather to search for a vertex at the extremities of a track than finding all possible combination of tracks that can form a vertex.

The FEDRA package provides a tool that combines all the tracks two by two and checks if they form a vertex. After, the two track vertices are checked for common tracks. The vertices with common tracks are combined in higher multiplicity vertices.

From the very beginning I was working on a different strategy. For the real neutrino events, tracks can be grouped based on geometrical criteria (they all should start in a relatively small volume), but because real data are only available from test-beam exposure, the algorithm starts with an already selected track (a beam-track). Because of scanning inefficiency, we have to search for vertices were the tracks don't necessary start in the same plate, we have to allow a few "holes". For this reason the algorithm

[1] EdbPVRec is the container class of all track and vertex parameters in FEDRA

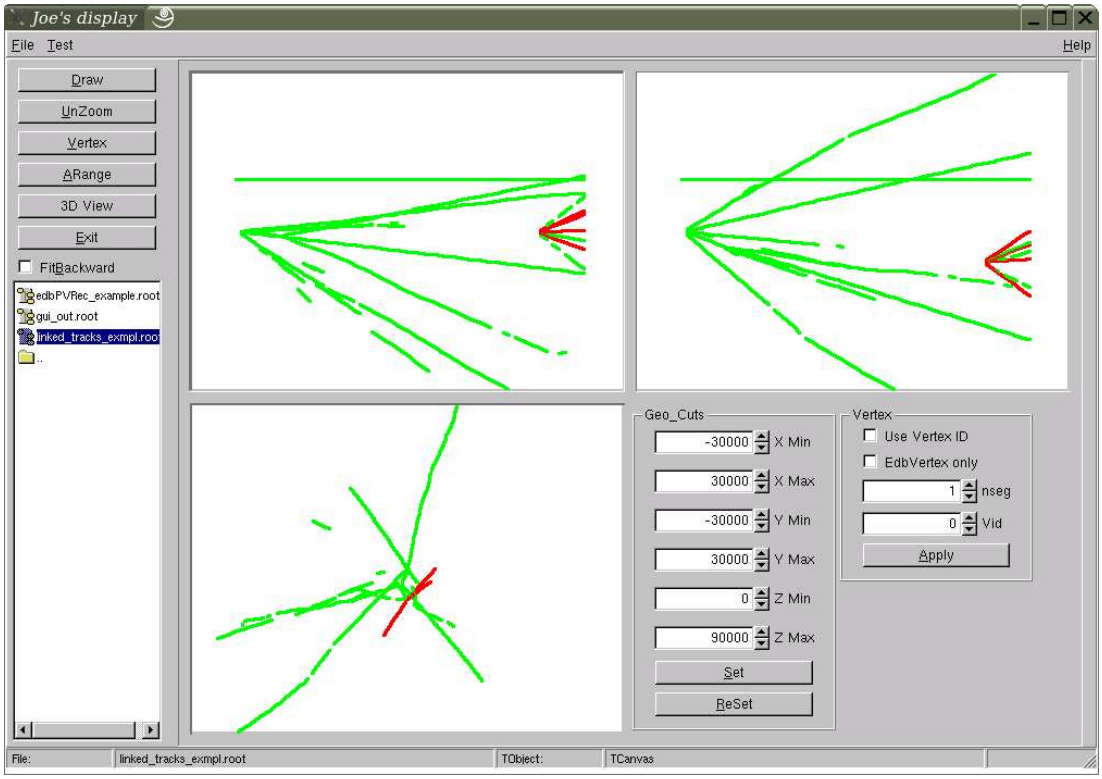



Figure 4.10: Event display showing a simulated $\nu_\mu$CC interaction. The tracks in red are selected for vertex fitting. The parameters of the fitted vertex ($\chi^2$, x,y,z coordinates) are displayed in the terminal window (below).

searches for candidate tracks starting usually up to 3 segments apart from the endpoint of the track.

Each time backscattered tracks are searched for. This way the same algorithm can be used for "V" search as well ( V's are vertices without incoming track) which is useful for neutrino event, gamma conversion and neutral decay search.

The algorithm that searches for vertices at the extremities of the tracks can be used repeatedly for the tracks attached to a vertex. Saving the tracks with a common event ID, a full event reconstruction is done, starting from any of the tracks belonging to the vertex.

Another possible application is the reconstruction of low momentum tracks. Large angle scattering further reduces the base-track finding efficiency, adding so many holes that the standard reconstruction fails. Applying the vertex finding in an iterative way to all the fragments we can reconstruct tracks once considered lost. Examples for event reconstruction and low momentum track reconstruction are shown on Fig. 4.11. On the first image of Fig. 4.11 a primary interaction and a secondary vertex reconstructed as one event can be seen. The second image shows a low momentum track broken up in many small fragments (also reconstructed as one event).

The performance of this tools is best shown in Chapter 7, where results with real data are presented.

The software realization of the algorithm is based on standard ROOT and FEDRA classes and it was designed with the idea to preserve compatibility with FEDRA tools, extensions added only when inevitable.

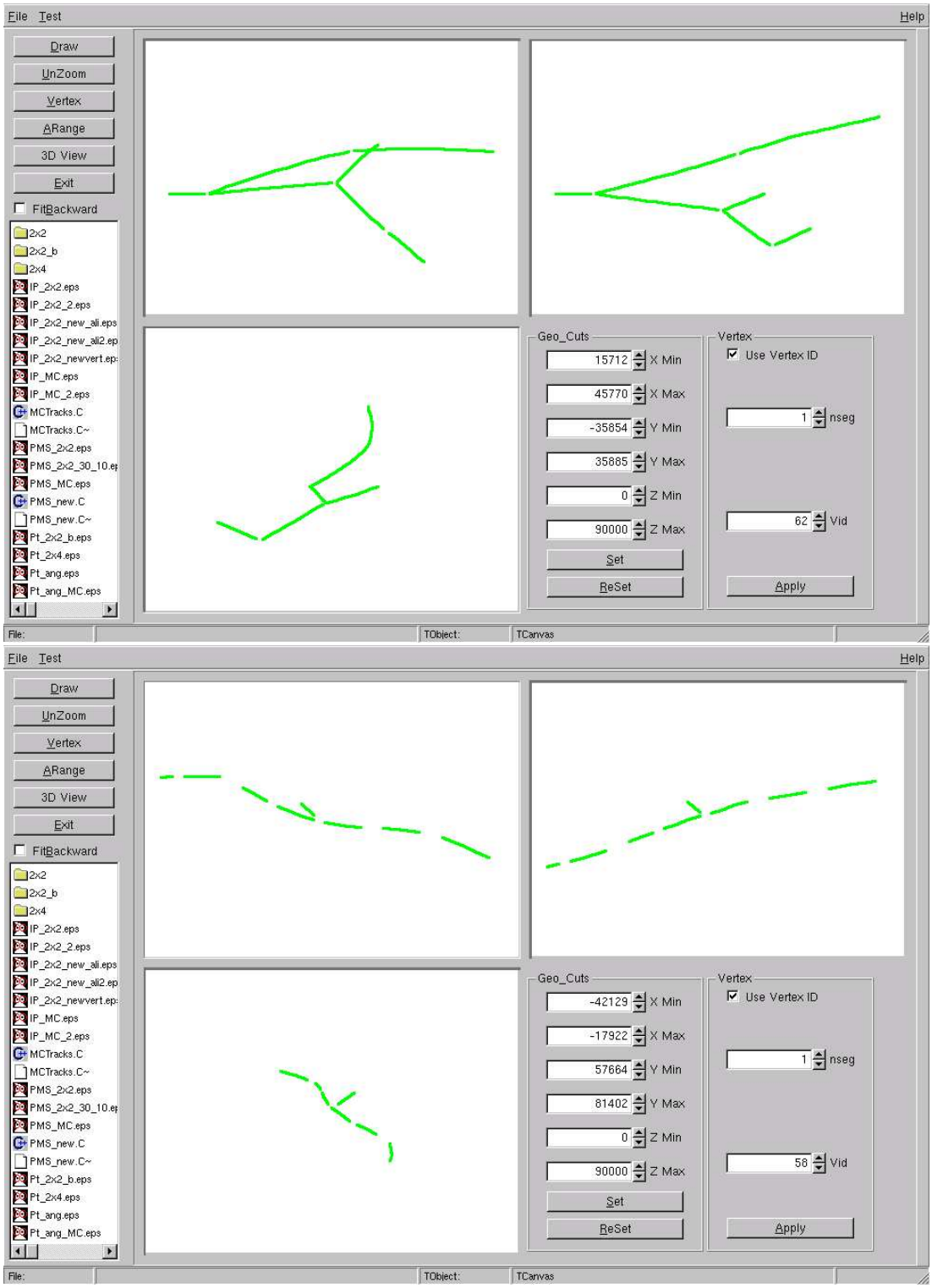


Figure 4.11: Event and track reconstruction using vertex finding tools

# Chapter 5

# Background estimation

The content of this chapter was published in [59]. Since then the study was refined and some corrections were made.

## 5.1 Hadronic background

One important background for the $\tau$ search is the re-interacting hadron originating from some other interaction, like $\nu_\mu$NC or $\nu_\mu$CC interactions. A hadronic interaction, when only one charged particle escapes from the lead, looks very similar to the $\tau$ decay. Real $\tau$ events can be distinguished from background events only by the different kinematics of the interaction. Using a simple simulation and analysis methods described in [32] one can try to estimate the hadronic background.

### 5.1.1 Definition of the kinematical parameters

In the real experiment we can not measure the momentum of the $\tau$ because of it's short decay length. To reduce the background we have to apply cuts on the other kinematical variables. The definition of kinematical parameters are given on Fig. 5.1. $P_\tau$ is the momentum of the $\tau$, $P_{had}$ is obtained by summing up the momenta of all other particles attached to the primary vertex and $P^T$ is the transverse component of the momenta. Using momentum conservation with the angles defined on Fig. 5.1, we can express the momentum of the $\nu$ and the momentum of the hadrons as:

$$P_\nu = P_\tau \cos\theta + P_{had} \cos\varphi$$

$$P_{had} \sin\varphi = P_\tau \sin\theta$$

In the experiment we will measure only $P_{had}$, $\varphi$ and $\theta$. From these variables it is possible to extract $P_\tau$ and $P_\nu$

$$P_\tau = \frac{P_{had} \sin\varphi}{\sin\theta}$$

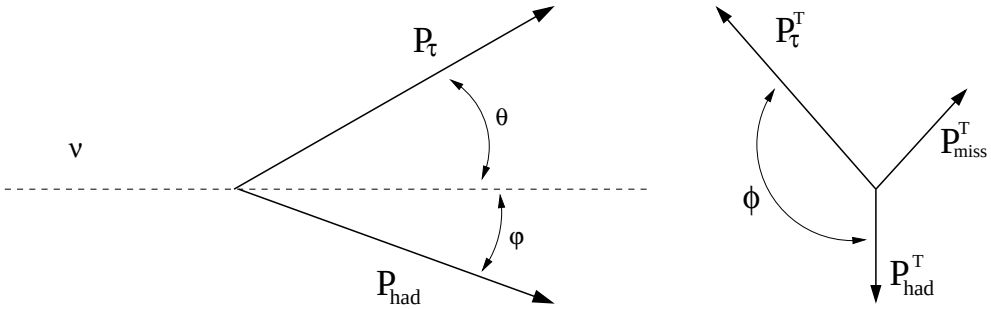


Figure 5.1: Definition of kinematical variables for the $\nu_\tau$ interaction. Left: side view of a $\nu_\tau$ interaction, right: front view showing the transverse projection of the particle momenta. For background events $P_\tau$ is replaced with $P_h$.

$$P_\nu \;=\; P_{had}\left(\cos\varphi + \frac{\sin\varphi}{\tan\theta}\right)$$

We also have to define the missing transverse momentum:

$$P^T_{miss} = |P^T_\tau - P^T_{had}|$$

Another important kinematical parameter is the angle between the transversal component of the $\tau$ momentum and the transverse momentum of the hadrons denoted with $\phi$ (see Fig. 5.1). The definition of the kinematical parameters is the same for all background events except that the $\tau$ is replaced with a misidentified hadron. The momentum of the re-interacting hadron mimicking the $\tau$ decay will be denoted with $P_h$. How well can be separated the signal and the background with this kinematic parameters can be seen on Fig. 5.2. While the $P^T_{miss}$ is similar for signal and background, there is a clear difference in the distribution of $\phi$.

Another kinematic variable that can be useful in distinguishing $\nu_\tau$ events is the isolation variable $Q_T$. $Q_T$ is defined as the momentum component of the $\tau$ perpendicular to the hadronic shower's momentum (see Fig. 5.3). The distribution of $Q_T$ for real $\nu_\tau$ events and background is shown on Fig. 5.4. In the case of background events the $\tau$ is replaced with one of the hadrons from the shower and the momentum of the shower is calculated summing up the momenta of all the other hadrons.

### 5.1.2 Simulation of the re-interaction rate

To estimate the re-interaction rate we used a simple Geant4 simulation. The geometry was a 1 mm thick lead plate (like one plate from the ECC Brick) and we simulated pion beams at different energies. A schematic drawing of the setup is shown on Fig. 5.5. We looked at the transverse momentum distribution of the outgoing particles. For comparison, this simulation was repeated using FLUKA by the Bologna group.

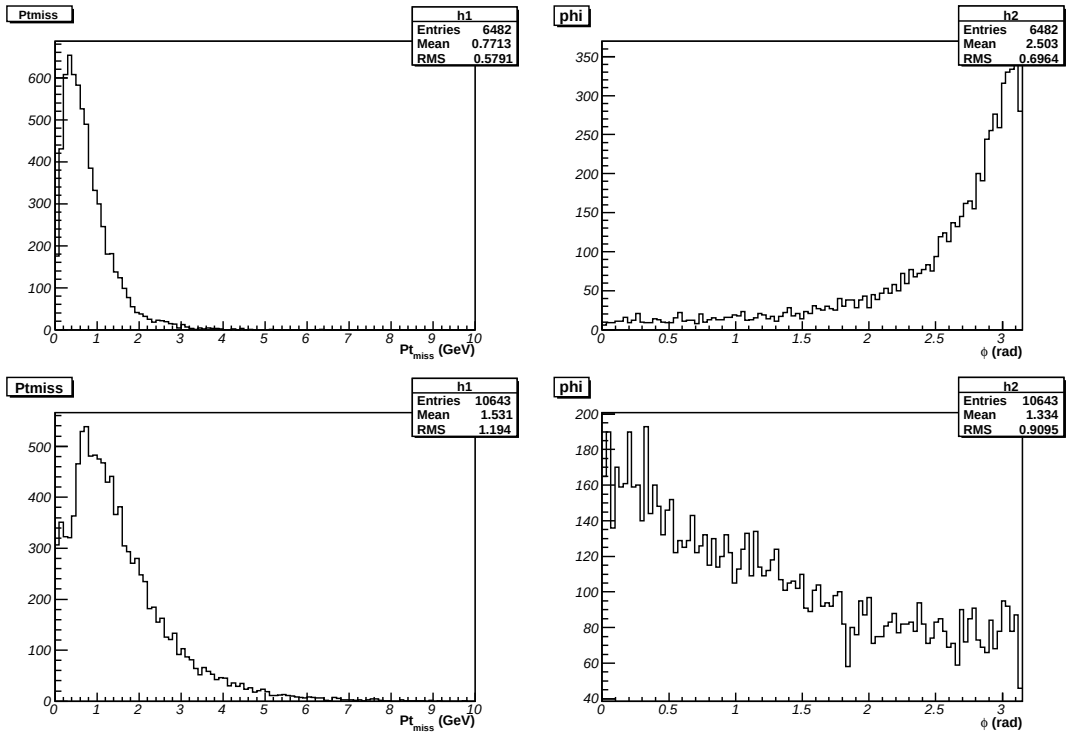


Figure 5.2: $P^T_{miss}$ and $\phi$ for $\nu_\tau$ (signal) events and below, for $\nu_\mu$NC (background) events

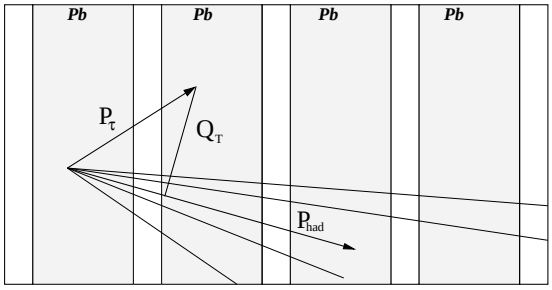


Figure 5.3: Definition of the isolation variable $Q_T$

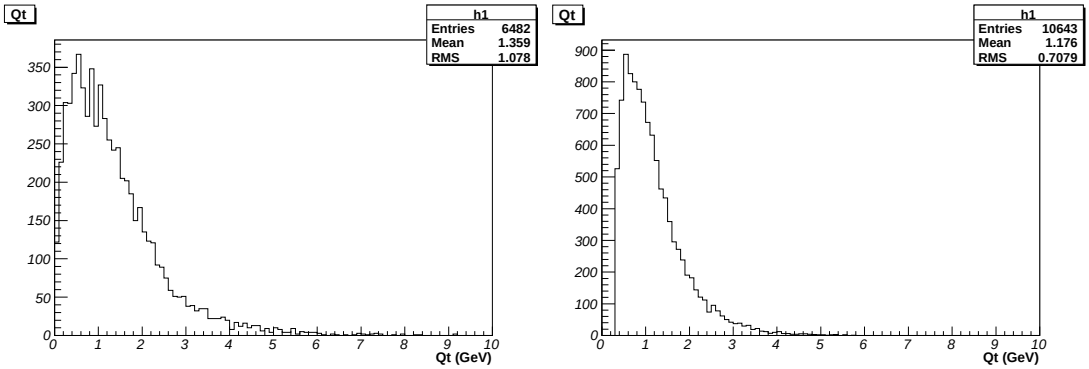


Figure 5.4: Qt for signal ($\nu_\tau$) and for background ($\nu_\nu$NC)

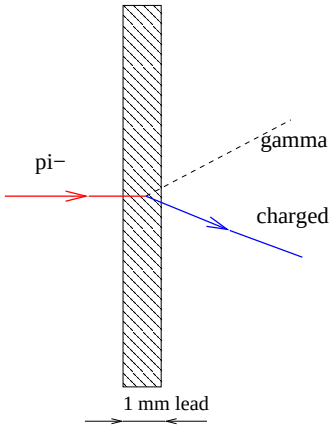


Figure 5.5: Simulation for background estimation

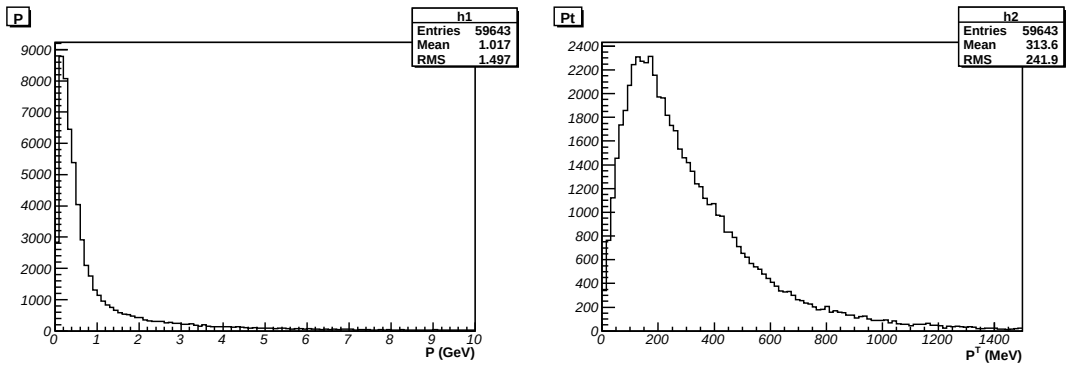


Figure 5.6: $P$ and $P^T$ distribution of hadrons from $\nu_\mu$NC events. The distributions for $\nu_\mu$CC events look quite similar

From all the interactions we keep only events where only one non-leptonic charged particle exits the lead and no $\gamma$'s point to the vertex. These are the hadronic interactions that can be mistaken for a $\tau$ decay. The exiting hadron must have a momentum above 1 or 2 GeV depending on the decay channel studied and has to pass cuts on the transverse momentum from 250 to 600 MeV. The choice of the $P$ and $P^T$ cuts are justified by the momentum distribution of the pion coming from the $\tau$ decay shown on Fig. 6.2.

To estimate the background for the $\tau \rightarrow \pi^-(n\pi^0)\nu_\tau$ decay channel, we also investigated the situation where more than one gamma can be attached to the vertex.

## 5.2 Background for the $\tau \rightarrow \mu + \nu_\mu + \nu_\tau$ channel

This background originates from $\nu_\mu$NC events with a hadron identified as a muon, as well from $\nu_\mu$CC events with the primary muon not identified and a hadron identified as a muon. A similar background originates from the large angle scattering of muons from $\nu_\mu$CC interaction, which we will not discuss here. To mimic the $\tau$ kink, a hadron must interact in the lead and pass the cuts used for this channel selection: $1\text{ GeV} < P_\mu < 15\text{ GeV}$ and the transverse momentum with respect to the $\tau$ direction: $P_\mu^T > 250$ MeV. The reason for chosing these cuts can be understood from the figure 5.6.

To simulate this background we estimated the interaction rate with $10^7$ pions for each energy. We kept only events where one non-leptonic charged particle exits the lead and no gammas can be attached to the vertex. We don't check for other neutral particles (mainly neutrons). We also require that the escaping hadron has $P^T > 250$ MeV. The transverse momentum is relative to the direction of the incoming hadron. The rate obtained is $3 - 4 \times 10^{-4}$ (see Fig. 5.8). To estimate the rate in the simulated $\nu_\mu$NC and $\nu_\mu$CC events, we use a rough fit as a weight function.

The fitted function for the Geant4 simulation is:

$$\text{rate} = (3.8 - 0.40 \times P + 0.07 \times P^2 - 0.0034 \times P^3) \times 10^{-4} \qquad (5.1)$$

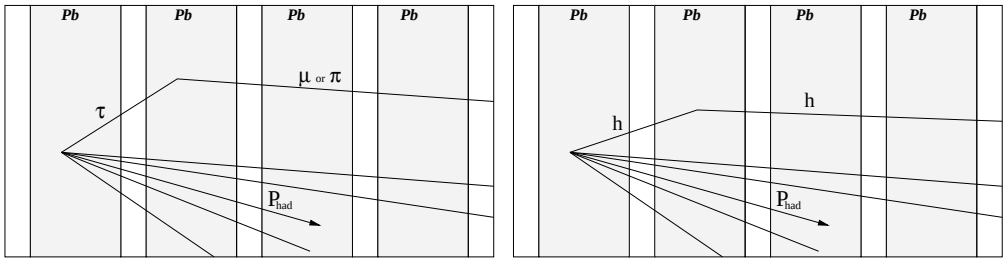


Figure 5.7: Topology of the signal (left) and background events (right). In the signal event the $\tau$ decays in a muon or a pion depending on the decay channel. In the background event a hadron coming from a different type of interaction, mimics the $\tau$ kink

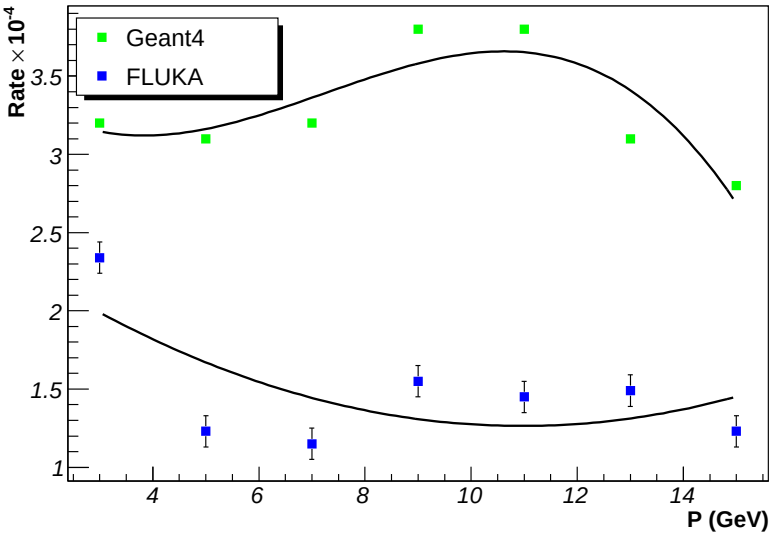


Figure 5.8: Interaction rate for $\pi$'s in 1 mm lead as function of the momentum. We keep events with only one charged hadron exiting the lead and with no gammas pointing to the vertex. $P_t > 250$ MeV

and for the Fluka simulation:

$$\text{rate} = (2.6 - 0.25 \times P + 0.0114 \times P^2) \times 10^{-4}$$

### 5.2.1 Background from $\nu_\mu$NC events

In a $\nu_\mu$NC interaction, a hadron can be misidentified as a muon. These type of events have no primary muon and the charged particles are mainly hadrons. For each hadron from the shower satisfying the momentum and $P^T$ cuts, the contribution is given by the rate equation 5.1 which has to be multiplied with the probability of hadron to muon misidentification (6%).

Since the hadron is embedded in the shower, the background could be reduced using $Q_T, \phi$ and $P^T_{miss}$ cuts. In table 5.1 we summarize the background rate for different cuts. In the table the cuts are applied subsequently: first $P$ and $P^T$ and after $\phi$, $Q_T$ and $P^T_{miss}$, in this order. The reason for this is that $P$ and $P^T$ cuts will be applied anyway and $P^T_{miss}$ would reduce the signal by the same amount, even if the other cuts have not been applied before. $Q_T$ has only a small effect on signal and background. The last colum of the table shows the total number of expected interactions for the five year run of the OPERA experiment.

### 5.2.2 Background from $\nu_\mu$CC events

This background originates from $\nu_\mu$CC events with the primary muon not identified and a hadron misidentified as a muon. According to [32], the probability to not identify a muon is 6.5%. We apply the same cuts as for $\nu_\mu$NC events and we multiply the obtained rate with the probability that the muon is not identified (6.5%) and the probability that a hadron is misidentified as a muon (6%). The estimated rate with different $Q_T, \phi$ and $P^T_{miss}$ cuts is shown in table 5.1.

## 5.3 Background for the $\tau \rightarrow \pi + \nu_\tau$ channel

The background originates from $\nu_\mu$NC events and from $\nu_\mu$CC events with the primary muon not identified. Topologically the problem is similar to the previous case: a re-interacting hadron mimics the $\tau$ kink. In addition the cuts for selecting the $\tau \rightarrow \pi$ decay channel must be satisfied:

- At the primary vertex:
  $P^T_{miss} < 1$ GeV
  $\phi > \frac{\pi}{2}$

- At the $\tau$ vertex
  $P^T_\pi > 600$ MeV with respect to the $\tau$ direction
  $P_\pi > 2$ GeV

| Cuts | Background from $\nu_\mu$NC Rate $\times 10^{-6}$ | Background from $\nu_\mu$CC Rate $\times 10^{-6}$ | Signal efficiency | Bckg. OPERA 9810 $\nu_\mu$NC+ 32620 $\nu_\mu$CC |
|---|---|---|---|---|
| $P_\pi > 1$ GeV & $P_\pi^T > 250$ MeV | 21.82 | 2.31 | 100% | 0.29 |
| FLUGG | 11.21 | 1.15 | | 0.15 |
| $\phi > \frac{\pi}{2}$ | 8.45 | 1.32 | 89.78% | 0.12 |
| FLUGG | 4.36 | 0.64 | | 0.06 |
| $Q_T > 0.4$ GeV | 7.74 | 1.24 | 79.73% | 0.12 |
| FLUGG | 3.93 | 0.60 | | 0.05 |
| $P_{miss}^T < 1$ GeV | 5.39 | 1.03 | 60.91% | 0.08 |
| FLUGG | 2.83 | 0.50 | | 0.04 |

Table 5.1: Background rates for $\tau \rightarrow \mu + \nu_\mu + \nu_\tau$ channel (DIS long decay). The cuts are always applied in addition to the previous one.

The rate shown on Fig. 5.9, is estimated with the same Geant4 simulation as before. We require that the escaping hadron has $P > 2$ GeV and $P^T > 600$ MeV. The fitted interaction rate as a function of momentum for the Geant4 simulation is:

$$\text{rate} = (0.0197 + 0.0788 \times P - 0.00432 \times P^2) \times 10^{-4} \tag{5.2}$$

and for the FLUKA simulation:

$$\text{rate} = (0.24 - 0.0039 \times P) \times 10^{-4}$$

### 5.3.1 Background from $\nu_\mu$NC events

The background originates from re-interacting hadrons that mimic the $\tau$ decay. For each hadron from the primary vertex with $P > 2$ GeV and $P^T > 600$ MeV, the contribution is given by the rate equation 5.2. Only events with at least 2 tracks are taken. In addition we apply $\phi > \frac{\pi}{2}$ , $Q_T > 0.4$ GeV and $P_{miss}^T < 1$GeV cuts. The results are summarized in table 5.2 applying the cuts one after each other exactly like in table 5.1.

### 5.3.2 Background from $\nu_\mu$CC events

$\nu_\mu$CC events with the primary muon not identified contribute to this background. We apply the same procedure as in the previous case, except that the rate is multiplied by 6.5%, the probability that a muon is not identified. The results are shown in table 5.2.

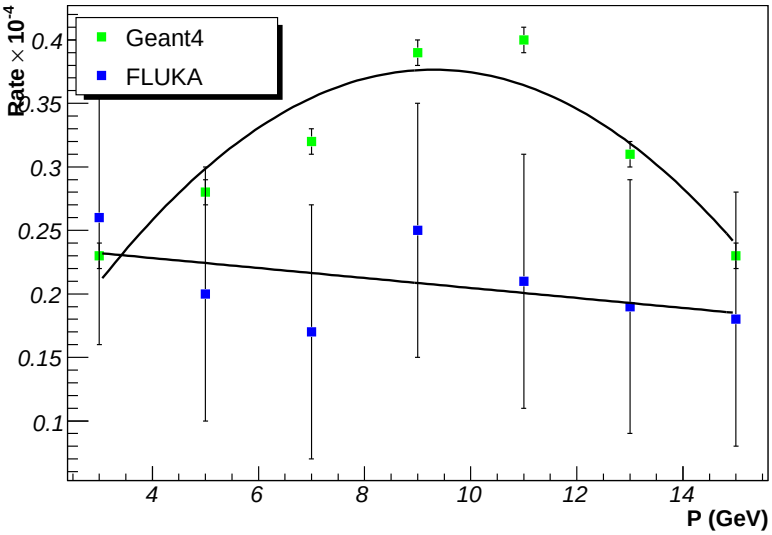


Figure 5.9: Interaction rate for $\pi$ in 1 mm lead as function of the momentum. We keep events with only one charged hadron exiting the lead and with no gammas pointing to the vertex. $P_t > 600$ MeV

| Cuts | Background from $\nu_\mu$NC Rate $\times 10^{-6}$ | Background from $\nu_\mu$CC Rate $\times 10^{-6}$ | Signal efficiency | Bckg. OPERA 9810 $\nu_\mu$NC+ 32620 $\nu_\mu$CC |
|---|---|---|---|---|
| $P_\pi > 2$ GeV & $P_\pi^T > 600$ MeV | 22.24 | 1.51 | 100% | 0.267 |
| FLUGG | 15.78 | 1.08 | | 0.190 |
| $\phi > \frac{\pi}{2}$ | 8.31 | 0.55 | 88.89% | 0.099 |
| FLUGG | 5.88 | 0.39 | | 0.070 |
| $Q_T > 0.4$ GeV | 8.31 | 0.55 | 78.48% | 0.099 |
| FLUGG | 5.88 | 0.39 | | 0.070 |
| $P_{miss}^T < 1$ GeV | 4.9 | 0.32 | 60.22% | 0.062 |
| FLUGG | 3.55 | 0.24 | | 0.042 |

Table 5.2: Background for $\tau \rightarrow \pi + \nu_\tau$ channel (DIS long decay). The cuts are always applied in addition to the previous one.

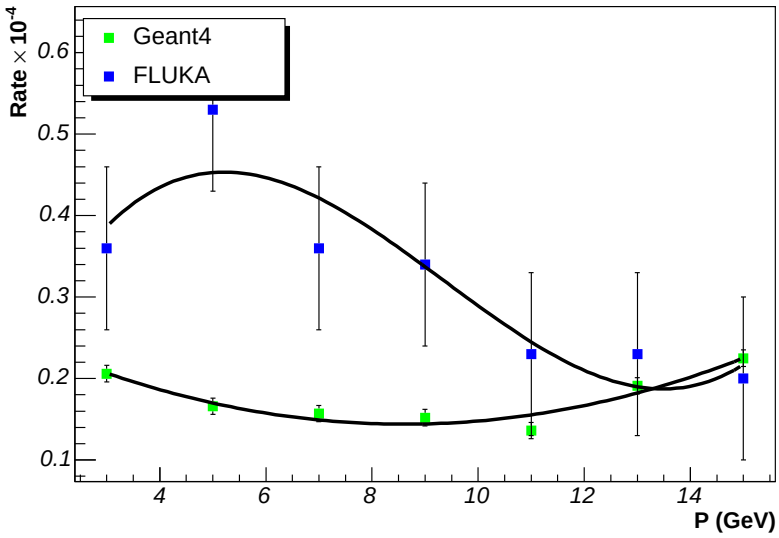


Figure 5.10: $P_t > 300$ MeV and more than one gamma pointing to the vertex

## 5.4 Background for $\tau \longrightarrow \pi^-(n\pi^0)\nu_\tau$ channel

For this decay channel we expect a significant improvement in detection efficiency by attaching $\gamma$'s from the $\pi^0$ decay to the secondary vertex (see Fig. 6.4). A possible background originates from a re-interacting hadron that after mimicking the $\tau$ kink produces high energy $\gamma$'s that can be interpreted as decaying $\pi^0$'s. When $\gamma$'s are attached to the secondary vertex, the cuts which are normally used in the case of the $\tau \longrightarrow \pi$ channel, are reduced to $P_\pi > 1$ GeV and $P_t > 300$ MeV (see 5.7.2 and 5.7.3). The interaction rate is simulated as before. In addition to the cuts applied to the exiting hadron, we require to have at least two $\gamma$'s attached to the vertex with kinetic energy higher than 500 MeV. The rate for different energies is shown on Fig. 5.10. The fitted rate equation for the Geant4 simulation is:

$$\text{rate} = (0.291 - 0.0342 \times P + 0.002 \times P^2) \times 10^{-4} \tag{5.3}$$

respectively for the FLUKA simulation:

$$\text{rate} = (0.0048 + 0.197 \times P - 0.0262 \times P^2 + 0.00093 \times P^3) \times 10^{-4}$$

The estimation is done for hadrons originating from $\nu_\mu$NC and $\nu_\mu$CC events as before, multiplying by the probability of muon misidentification the rate obtained with $\nu_\mu$CC events. The resulting rates are shown in table 5.3.

It is interesting to see, that this time, the FLUKA simulation gives a higher background rate than Geant4.

| Cuts | Background from $\nu_\mu$NC Rate $\times 10^{-6}$ | Background from $\nu_\mu$CC Rate $\times 10^{-6}$ | Signal efficiency | Bckg. OPERA 9810 $\nu_\mu$NC+ 32620 $\nu_\mu$CC |
|---|---|---|---|---|
| $P_\pi > 1$ GeV & $P_\pi^T > 300$ MeV | 20.05 | 1.35 | 100% | 0.24 |
| FLUGG | 37.09 | 2.50 | | 0.44 |
| $\phi > \frac{\pi}{2}$ | 7.72 | 0.50 | 89.63% | 0.09 |
| FLUGG | 14.24 | 0.94 | | 0.17 |
| $Q_T > 0.4$ GeV | 7.21 | 0.47 | 80.02% | 0.08 |
| FLUGG | 13.54 | 0.90 | | 0.16 |
| $P_{miss}^T < 1$ GeV | 5.16 | 0.33 | 61.18% | 0.06 |
| FLUGG | 9.42 | 0.62 | | 0.11 |

Table 5.3: Background rates for the $\tau \rightarrow \pi^-(n\pi^0)\nu_\tau$ channel. The cuts are always applied in addition to the previous one.

## 5.5 Summary of background estimations

In this chapter we computed the background rates originating from hadronic re-interactions, for the $\tau \rightarrow \mu + \nu_\mu + \nu_\tau$ , $\tau \rightarrow \pi + \nu_\tau$ and $\tau \rightarrow \pi^-(n\pi^0)\nu_\tau$ DIS long decays. The hadron re-interaction rate was estimated with Geant4 and a comparison is done with a similar FLUKA simulation.

After the $\phi > \frac{\pi}{2}$ cut we found that the total background rate for a five year run of the OPERA experiment (shown in the last colum of table 5.1, 5.2 and 5.3) is 0.12 for the $\tau \rightarrow \mu + \nu_\mu + \nu_\tau$ channel, 0.09 for the $\tau \rightarrow \pi + \nu_\tau$ channel and 0.09 for the $\tau \rightarrow \pi^-(n\pi^0)\nu_\tau$ channel. Apparently the $Q_T$ cut has little effect and the $P_{miss}^T$ cut removes a significant part of the signal. Since the background rate without these cuts it is already about 0.1 events in five years, we suggest that this cuts could be omitted to increase detection efficiency.

# Chapter 6

# Detection efficiency for the $\tau \longrightarrow h$ channel

In this chapter we estimate detection efficiencies for the $\tau \rightarrow \pi\nu_\tau$ and $\tau \rightarrow \pi(n\pi^0)\nu_\tau$ decay channels. The neutrino events were generated with the official neutrino generator of OPERA and the resulting particles propagated in Geant4. The numbers obtained are compatible with previous estimations published in [32, 33].

## 6.1 $\tau$ energy distribution

The starting point of our simulation was the neutrino events generated with the NEGN [48] neutrino event generator[1]. The $\nu_\tau$ events were generated with the same neutrino energy spectrum as the $\nu_\mu$ spectrum of the CNGS. For this reason, at the end, each result was weighted with the oscillation probability for $\Delta m^2 = 0.002$ eV$^2$. The analysis is done for each hadronic decay channel separately for DIS and QE events as well.

### 6.1.1 Long and short decay

The $\nu_\tau$ interactions were simulated in the center of the first lead plate in the x-y plane, randomly distributed along the z-axis. Since the identification of the $\tau$ decays occurring in the same lead plate where the neutrino interaction takes place (short decay) is extremely difficult, we concentrate only on long decays. We found that the number of the $\tau$'s decaying in the first lead plate is 55.4% DIS and 57.0% QE, which is in good agreement with [32] (56.3%). The remaining 44.59% DIS and 42.91% QE decay after the first lead plate and **42.97%** DIS and **41.54%** QE decay between the end of the first and the end of the third plate (which corresponds to the definition of a long decay according to [32]).

[1] /afs/cern.ch/exp/opera/may2001evegen/tauh1.beamfile & tauhqe1.beamfile

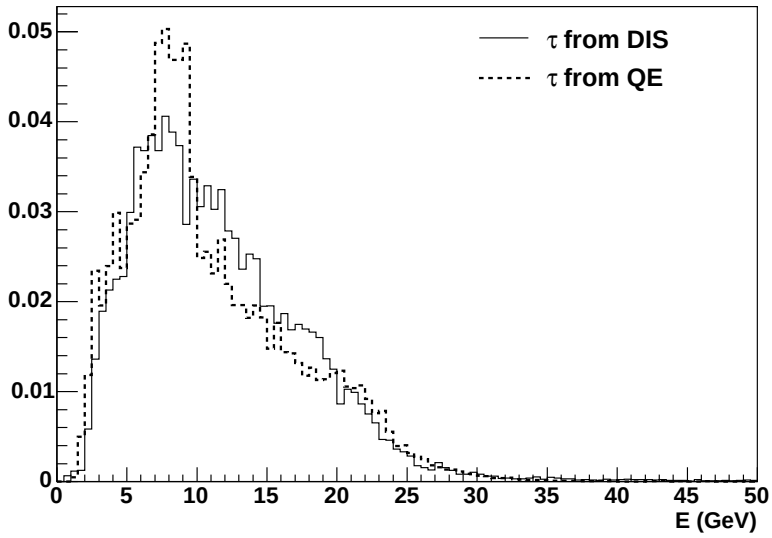


Figure 6.1: $\tau$ energy distribution from $\Delta m^2 = 0.002$ eV$^2$ oscillated neutrinos

### 6.1.2 Energy distribution of the hadron

Fig 6.2 shows the momentum and $P_t$ distributions of the $\pi^-$ from the $\tau$ decay (DIS) for 10.000 generated events. The decay branching ratios according to [9] are: $11.06 \pm 0.11$ ($\tau \rightarrow \pi^-$), $25.41 \pm 0.14$ ($\tau \rightarrow \pi^-\pi^0$), and $9.39 \pm 0.14$ ($\tau \rightarrow \pi^-\pi^0\pi^0$). The number of $\pi^-$ surviving $P_t$ cuts of 250, 300 & 600 MeV and 1 and 2 GeV in total momenta are shown in table 6.1 for DIS and table 6.2 for QE events. These cuts are suggested by [32] and comparing the distributions shown on Fig. 5.6 and Fig. 6.2 they seem to be a natural choice.

It is worse to mention that the total momentum, $P$ and $P_t$ are not independent variables. E.g. in table 6.1, for $1\pi^-$, 71.21% pions survive the 600 MeV $P_t$ cut and 78.11% the 2 GeV $P$ cut, which would result in the probability of $\varepsilon_E \times \varepsilon_{P_t} = 55.62\%$ if they were independent. This is less than $61.8\%$, the number of those which survive $P \,\&\, P_t$ cuts. Hence, in the calculation of the overall efficiency the latter cuts are applied.

## 6.2 Vertex location using gammas

The cuts on momentum and $P_t$ can be reduced using $\gamma$'s from $\pi_0$ decays to identify the secondary vertex. A $\gamma$ is assigned to the secondary vertex, if it points to the vertex within the error of the measurement and if it can be clearly distinguished from a $\gamma$ originating from the primary vertex. The vertex assignment depends on the $\tau$ and $\pi^0$ decay length, of which the decay length distribution is shown in Fig. 6.3.

The vertex assignment has been done with the impact parameter (IP) method described in [35]. The IP associated to the primary and secondary vertices are shown in

| $P_t(MeV/c)$ | 0 | 250 | 300 | 600 |
|---|---|---|---|---|
| $1\pi^-$ | 100% | 95.13% | 93.4% | 71.21% |
| $1\pi^0$ | 100% | 79.88% | 73.13% | 27.61% |
| $2\pi^0$ | 100% | 67.67% | 58.36% | 9.48% |
| $1\pi^-$P>1GeV | 90.32% | 88.15% | 87.32% | 70.54% |
| $1\pi^0$P>1GeV | 80.62% | 70.49% | **65.66%** | 27.19% |
| $2\pi^0$P>1GeV | 77.27% | 59.66% | **52.23%** | 9.48% |
| $1\pi^-$P>2GeV | 78.11% | 75.96% | 75.12% | **61.81%** |
| $1\pi^0$P>2GeV | 63.17% | 56.11% | 52.74% | 24.21% |
| $2\pi^0$P>2GeV | 51.82% | 41.54% | 37.76% | 8.35% |

Table 6.1: Number of events surviving $P_t$ and $P$ cuts for DIS events. The boldface numbers show the effect of the cuts used in the efficiency estimations.

| $P_t(MeV/c)$ | 0 | 250 | 300 | 600 |
|---|---|---|---|---|
| $1\pi^-$ | 100% | 94.67% | 93.55% | 73.9% |
| $1\pi^0$ | 100% | 80.08% | 74.01% | 28.22% |
| $2\pi^0$ | 100% | 61.72% | 52.03% | 9.85% |
| $1\pi^-$P>1GeV | 89.86% | 86.73% | 86.36% | 72.46% |
| $1\pi^0$P>1GeV | 81.35% | 70.20% | 65.93% | 27.64% |
| $2\pi^0$P>1GeV | 74.61% | 54.87% | 47.18% | 9.85% |
| $1\pi^-$P>2GeV | 78.07% | 74.94% | 74.57% | 63.68% |
| $1\pi^0$P>2GeV | 61.94% | 55.15% | 51.82% | 24.07% |
| $2\pi^0$P>2GeV | 50.60% | 39.07% | 34.93% | 8.91% |

Table 6.2: Number of events surviving $P_t$ and $P$ cuts for QE events

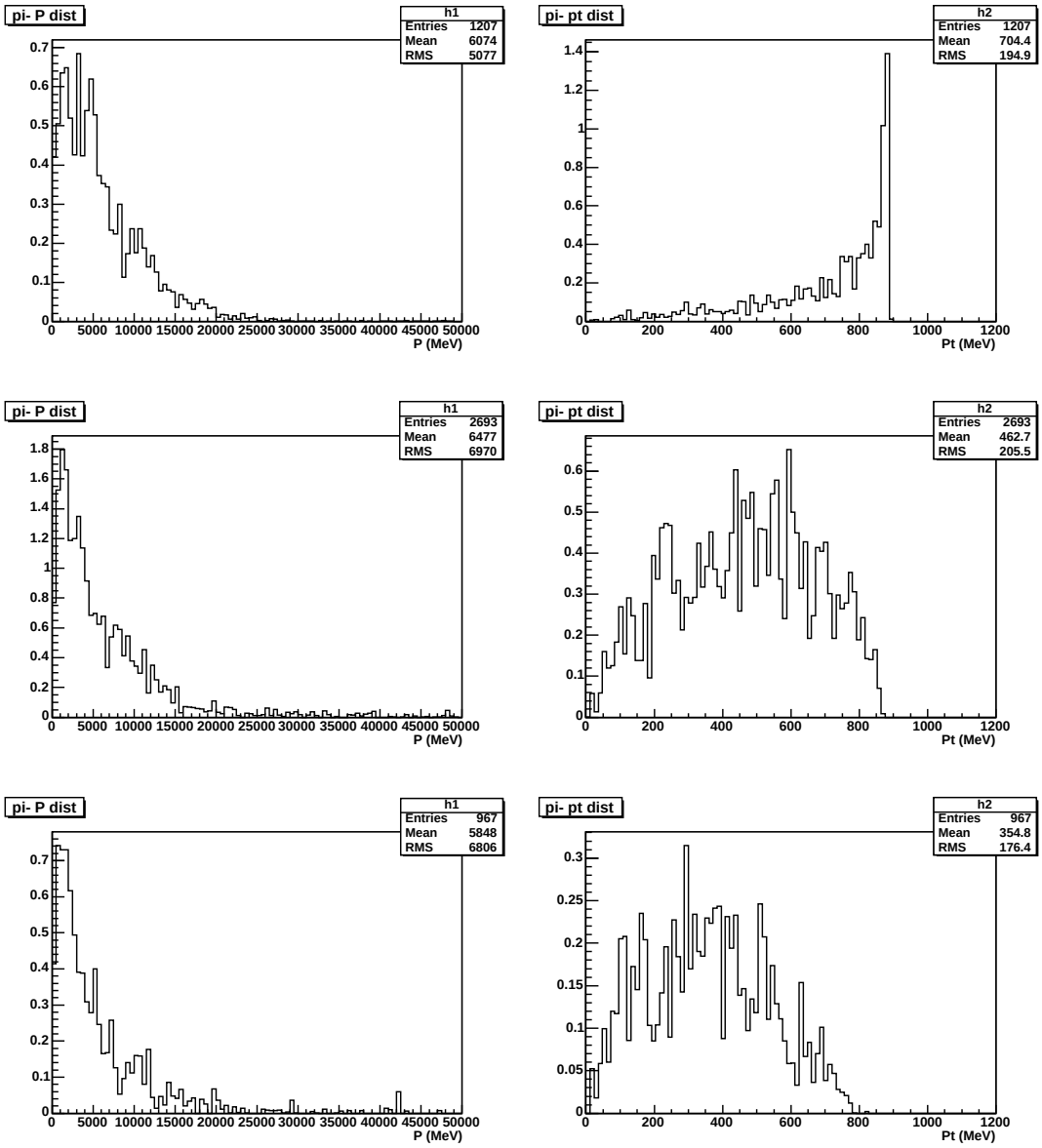


Figure 6.2: $\pi^-$ momentum and $P_t$ distributions. From top to bottom: $\tau \rightarrow \pi^-$, $\tau \rightarrow \pi^-\pi^0$ and $\tau \rightarrow \pi^-\pi^0\pi^0$ channels.

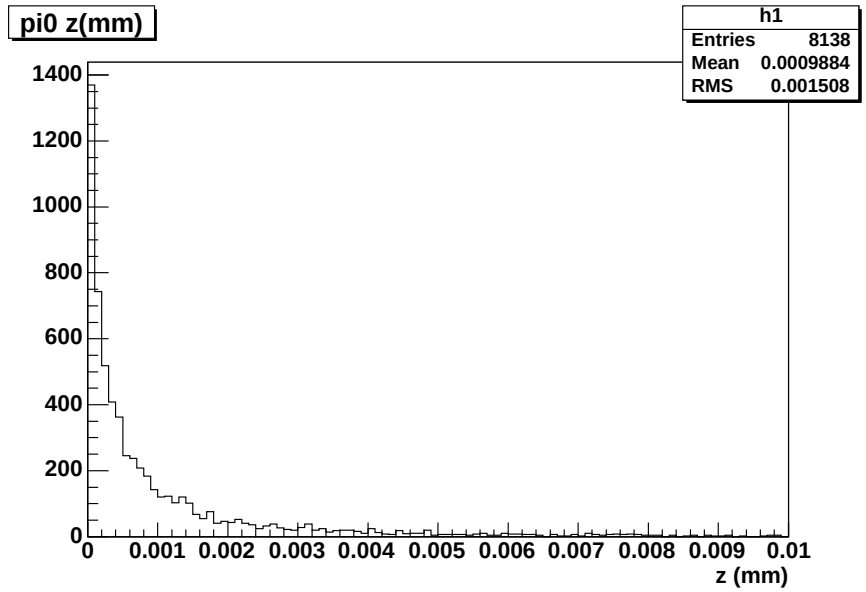


Figure 6.3: Decay length of $\pi^0$'s originating from $\tau$-decays

| $\gamma$ | IP2<$2\sigma$ & IP1>$2\sigma$ | |
|---|---|---|
| | $1\pi^0$ | $2\pi^0$ |
| DIS | **57.35%** | **53.15%** |
| QE | **56.87%** | **56.53%** |

Table 6.3: Percentage of $\gamma$'s correctly assigned to the secondary vertex with 30% energy measurement error

figure 6.4 for a typical event topology. Due to multiple scattering of the electrons, the direction of the $\gamma$ can be measured with an error of:

$$\sigma = \sqrt{\frac{\left(0.0136/(E_\gamma[\text{GeV}]/2)\sqrt{1/5.6}\right)^2 + 0.001^2}{2}}$$

.

The analysis is done only for long decays. $\gamma$'s with an energy below 500 MeV are rejected. $\gamma$'s are assigned to the secondary vertex if the following criteria are satisfied: IP2 < $2\sigma$ & IP1 > $2\sigma$. The rates are shown in table 6.3, assuming a 30% measurement error on $E_\gamma$ ([35]), which does not change the rate much.

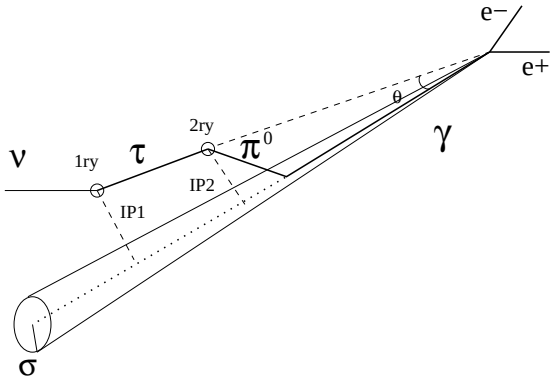


Figure 6.4: Definition of the impact parameters (IP) for the 1ry and the 2ry vertex

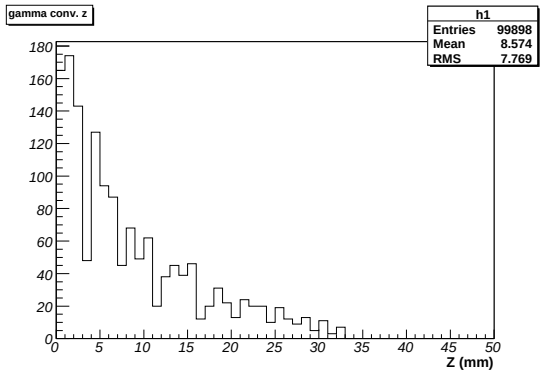


Figure 6.5: Distribution of converted $\gamma$'s in function of the z position

### 6.2.1 Gamma conversion in the Brick

In the simulation 100000 $\gamma$'s were shot into the Brick with an energy randomly distributed between 0 and 20 GeV. The cross section is almost independent of the energy. 99.88% of the $\gamma$'s convert in the Brick: 74.61% of the gammas convert in the first 10 plates and 93.47% in the first 20 plates of the brick (see [32] page 162). The number of converted $\gamma$'s as a function of z position can be seen in Fig. 6.5.

The probability that a $\gamma$ is converted and can be used to identify $\tau$ events is 60.7% which is the number of converted $\gamma$'s times the probability that the primary interaction takes place within the first 34 plates of the Brick (56-20 and -2 because of the long decay).

## 6.3 Overall efficiencies

The detection efficiency is calculated with:

$$\varepsilon_\tau = \varepsilon_{trig} \times \varepsilon_{Brick} \times \varepsilon_{Geom} \times \varepsilon_{vtx} \times (1 - \varepsilon_{fakelep}) \times \varepsilon_{long} \times \varepsilon_{kink} \times \varepsilon_{B2B} \times \varepsilon_E \times \varepsilon_{P_t} \times \varepsilon' \times BR$$

were: $\varepsilon_{trig}$ is the trigger efficiency, $\varepsilon_{Brick}$ the Brick finding efficiency, $\varepsilon_{Geom}$ the geometrical efficiency, $\varepsilon_{vtx}$ is the vertex location efficiency, $\varepsilon_{fakelep}$ the lepton misidentification probability, $\varepsilon_{long}$ the probability of a long decay, $\varepsilon_{kink}$ the probability of seeing a kink, $\varepsilon_{B2B}$ the efficiency of following an event in another Brick, $\varepsilon_E$ and $\varepsilon_{P_t}$ are the efficiencies corresponding to energy and $P_t$ cuts and $BR$ is the branching ratio of the respective decay channel.

To calculate the overall efficiency channel by channel, the efficiencies from [32] and presentations made at collaboration meetings are used except $\varepsilon_E$, $\varepsilon_{P_t}$, $\varepsilon_{long}$, $BR$ and additional factors for the channels with $\pi^0$.

### 6.3.1 $\tau \longrightarrow \pi\nu_\tau$ channel

Applying $P_\pi > 2\,GeV$ and $P_t > 600\,MeV$ cuts, 61.81% of the particles from DIS interactions and 63.68% from QE survive. 42.97% of DIS and 41.54% of QE interactions are long decays and taking into account the branching ratio of 11%, one obtains:

$$\varepsilon_\tau = 1.12\% \text{ DIS} \qquad \varepsilon_\tau = 1.22\% \text{ QE}$$

### 6.3.2 $\tau \longrightarrow \pi^-\pi^0\nu_\tau$ channel

For cuts of $P_\pi > 2\,GeV$, $P_t > 600\,MeV$ and no $\gamma$ information, the total efficiencies are: 1.01% for DIS and 1.07% for QE events. If a $\gamma$ is associated to the secondary vertex, the cuts are lowered to $P_t > 300MeV$ and $P_\pi > 1GeV$. From that, the overall efficiency is calculated with: $\varepsilon_\tau = \varepsilon_{trig} \times \varepsilon_{Brick} \times \varepsilon_{Geom} \times \varepsilon_{vtx} \times (1 - \varepsilon_{fakelep}) \times \varepsilon_{long} \times \varepsilon_{kink} \times \varepsilon_{B2B} \times \varepsilon_{E\&P_t} \times \varepsilon_{\gamma\,conv} \times \varepsilon_{\gamma\,tag} \times \varepsilon' \times BR$. resulting in:

$$\varepsilon_\tau = 0.89\% \text{ DIS} \qquad \varepsilon_\tau = 0.94\% \text{ QE}$$

This is true if only one $\gamma$ is assigned to the vertex. Since there are always two in the decay of the $\pi^0$, the probability that at least one $\gamma$ can be assigned, is $1 - (1 - \varepsilon_{\gamma\,tag})^2$, which increases the efficiency to:

$$\varepsilon_\tau = 1.27\% \text{ DIS} \qquad \varepsilon_\tau = 1.35\% \text{ QE}$$

### 6.3.3 $\tau \longrightarrow \pi^-2\pi^0\nu_\tau$ channel

In the case of $P_\pi > 2\,GeV$ and $P_t > 600\,MeV$, the total efficiencies are:

$$\varepsilon_\tau = 0.12\% \text{ DIS} \qquad \varepsilon_\tau = 0.14\% \text{ QE}$$

The probability that at least one $\gamma$ is assigned to the vertex is: $1-(1-\varepsilon_{\gamma\, tag})^4$. With the lowered cuts ($P_t > 300MeV$ and $P > 1GeV$) for the efficiencies we get:

$$\varepsilon_\tau = 0.43\% \text{ DIS} \qquad \varepsilon_\tau = 0.42\% \text{ QE}$$

## 6.4 Summary of efficiency estimations

Summing up the estimated efficiencies per channel, the overall efficiencies for the hadronic channel are: $\varepsilon_\tau = \mathbf{2.82\%}$ for DIS and $\varepsilon_\tau = \mathbf{2.99\%}$ for QE.

Without gamma tagging the efficiencies are smaller: $\varepsilon_\tau = 2.13\%$ (DIS) and $\varepsilon_\tau = 2.43\%$ (QE). Hence a significant improvement can be obtained tagging the $\gamma$. For the 1 $\pi^0$channel, an improvement of 20% for DIS and 40% for QE events can be achieved. For the $2\pi^0$ channel, the improvement is a factor 3 for DIS and QE. In table 6.4 we summarize our estimation based on Geant4 simulation and the numbers from the Proposal [32, 33].

| | $1\pi^-$ | $1\pi^- + 1\pi^0$ | $1\pi^- + 2\pi^0$ | Total | Proposal |
|---|---|---|---|---|---|
| No $\gamma$ tagging | 1.12(1.22) | 1.01(1.07) | 0.12(0.14) | 2.13(2.43) | 2.2(2.8) |
| With $\gamma$ tagging | 1.12(1.22) | 1.27(1.35) | 0.43(0.42) | 2.82(2.99) | 2.8(3.5) |

Table 6.4: Comparison of efficiency estimations (DIS). In parenthesis the estimation for QE interactions.

Despite the fact that in [32] the efficiencies are calculated with a total 50% branching ratio (in our case only 45%), our numbers are compatible, which means that a small gain was achieved.

# Chapter 7

# Experimental results

At the moment of writing this document the OPERA detector did not start taking data. For tuning of the scanning stations and developing analysis algorithms we had to rely on Monte Carlo and test-beam data. The role of the simulation in the analysis procedure was presented in the previous chapter. Here I will summarize our results with experimental data.

## 7.1 Test-beams

During the preparation time of the experiment several test-beam exposures were performed. The ones that we were involved in, are: pion test-beam at CERN, electron test-beam at DESY and neutrino test-beam at Fermi-lab. In these experiments ECC Bricks similar to the final OPERA Bricks were used, sometimes with a reduced number of emulsion sheets, to reduce the cost. The emulsion sheets were exposed and developed in various places in various conditions, therefore the data quality shows large fluctuations. Despite of the problems with the data quality, in most of the cases we acquired enough data to perform the track and vertex reconstruction and we could come close to our physics goals.

## 7.2 8 GeV pion test-beam

This test-beam exposure was performed at CERN in November 2004 with multiple goals in mind: to study Changeable Sheet (CS) to Brick connection, vertex location studies, pion - electron identification and tests of Bricks made with the Brick Assembly Machine (BAM), at that time under development.

Both Neuchâtel and Bern groups received one ECC brick with a CS exposed to a low intensity 8 GeV pion beam. The incident angle of the beam was +50 mrad in the x-z plane and close to 0 in the y-z plane. The beam intensity was chosen in such a way, that the number of accumulated pion tracks is about 10 pion-track/cm$^2$. The beam contains a significant muon contamination of about 20%. The exact numbers recorded by

scintillator counters are shown in table 1. The full volume of both bricks was scanned. We acquired an unprecedented (at the time of writing) quantity of experimental data, that put to stress all the hardware and software involved in data processing.

| Brick ID | Pions | Muons | Cosmic ray exposure |
|---|---|---|---|
| #1 Neuchâtel | 1139 | 220 | 6h |
| #6 Bern | 1142 | 150 | 6h |

Table 7.1: Scintillator triggers

Once the emulsions are scanned and aligned, we can search for the pion tracks. In the first step we want to be sure that the number of tracks is consistent with the data recorded by the electronic counters. To estimate the number of passing through pion tracks I used interaction and collision length given by the PDG book. The observed number of events in a fixed target taking into account the beam attenuation can be given as:

$$N_{obs} = N_b \frac{l\rho}{\Lambda_I} \int_0^l \exp(-\frac{x}{\Lambda_I}) dx$$

Where $N_b$ - is the number of beam particles, $l$ - the target thickness, $\rho$ - the target density, $\Lambda_I$ the interaction length, $\Lambda_I = 194\,\mathrm{g/cm^2}$ for lead. Unfortunately, because of limited angular acceptance we loose some of the elastic collisions, therefore the number of passing through particles is somewhere between the one calculated with the inelastic cross-section and the one calculated with the total cross-section. By practical reasons related to the hardware and to reduce the scanning time, we restrict ourself to a fiducial volume defined by only 80 $\mathrm{cm^2}$ from the total 120 $\mathrm{cm^2}$ surface of the emulsion sheet. As a consequence, the effective number of beam particles is about 760 in each Brick (assuming homogeneous distribution). We expect to see between 400 and 550 tracks. Because the scanning efficiency is not better than 90% we can not require that the tracks contain more than 50 segments (from 56). A comparison with a Geant4 simulation with reconstruction (ORFEO) predicts about 430 passing through tracks. On Fig. 7.1 we see the distribution of passing through tracks with more than 50 segments within an angular acceptance of $\pm 0.2$ mrad around the peak. The 487 tracks found, in the Brick Nb.6 are within the expectations, since we have no exact knowledge of the beam profile, position and detector efficiency in general.

In the next step we concentrate on finding pion interactions. This means inelastic and elastic interactions where the scattering angle is bigger than the acceptance for track reconstruction. With the help of the vertex finding algorithm described in section 4.6, I found a considerable number of pion interactions. The expected number of inelastic interactions is about 210.

The vertex-finding algorithm reconstructs vertices with at least one beam-track with at least three segments. Vertices with up to 7 tracks attached to the vertex were

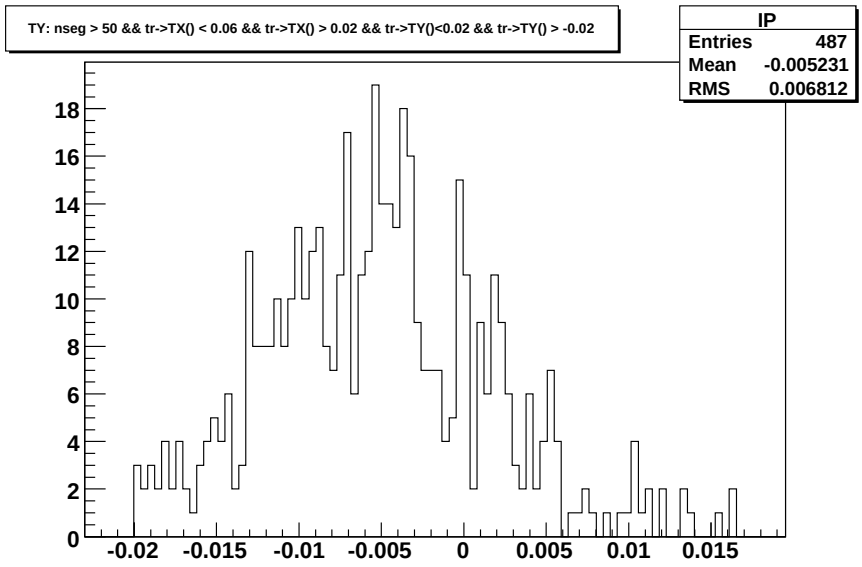


Figure 7.1: Angular distribution of passing through pions in the 8 GeV test-beam data

found with backscattered particles included. One example of a high multiplicity vertex can be seen on Fig. 7.2

The number of vertices found in the data is comparable with the one found in simulated events. On the first two plots one can see a comparison of vertex multiplicities for the vertices found in Brick Nb.6 and Geant4 simulation with 760 pions and reconstructed with ORFEO (Fig. 7.3). The number of vertices is roughly the same except a small difference due to the background from cosmic-rays and muons from the accelerator. In real data, these produce interactions as well.

Figure 7.4, shows the Impact Parameter (IP) of the tracks to the fitted vertex point. We can clearly see that the IP of tracks in the real data is better than in the case of simulation. This is due to smearing, which reproduces only roughly the measurement error. The relative error of two base-tracks close to each other is expected to be smaller than the error that we measure globaly (local distortions affect them in the same way). When treating MC data, the smearing is done independently for each base-track and this results in worst spatial resolution in the simulation.

On Fig. 7.5 we can see the missing transverse momentum (Pt) in the vertices found. Despite the good results, we shouldn't be too confident with these data. After the studies presented in this document about momentum measurement, we know that we can measure the momentum only within a restricted range, much lower than in MC. The technical diffculties are increased by the presence of short tracks an many missing segments. As a consequence the measured missing Pt is pushed towards the origin, in the real data.

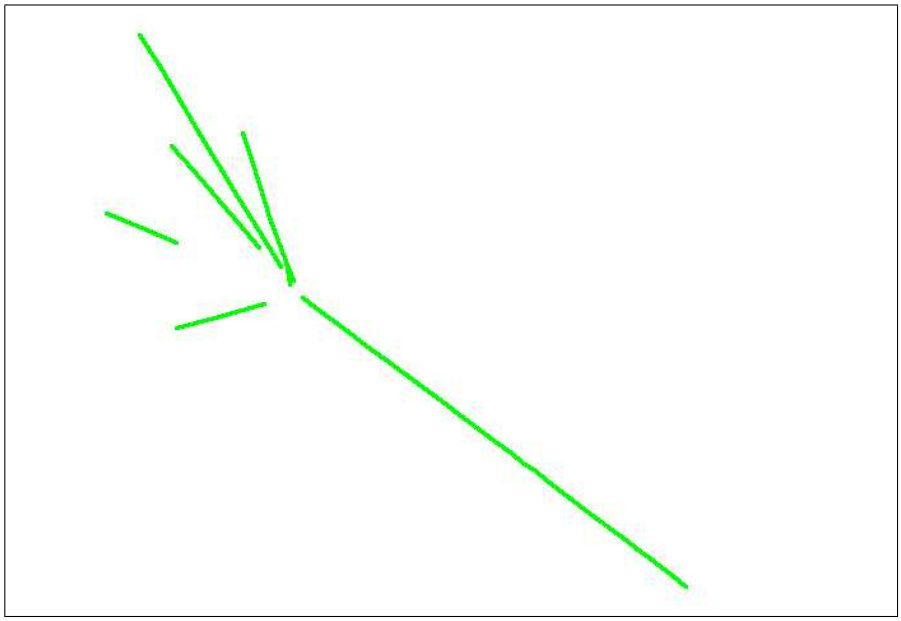

Figure 7.2: Reconstructed pion vertex in the 8 GeV test-beam data

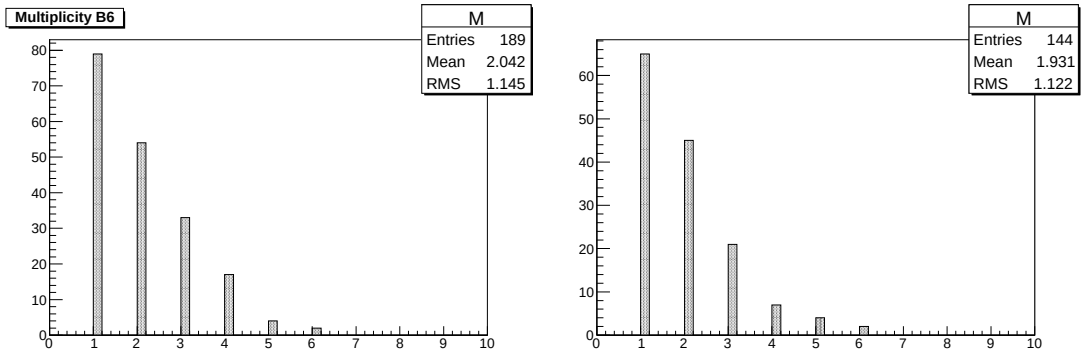


Figure 7.3: Vertex multiplicity in the 8 GeV pion data (left) and Geant4 simulation (right)

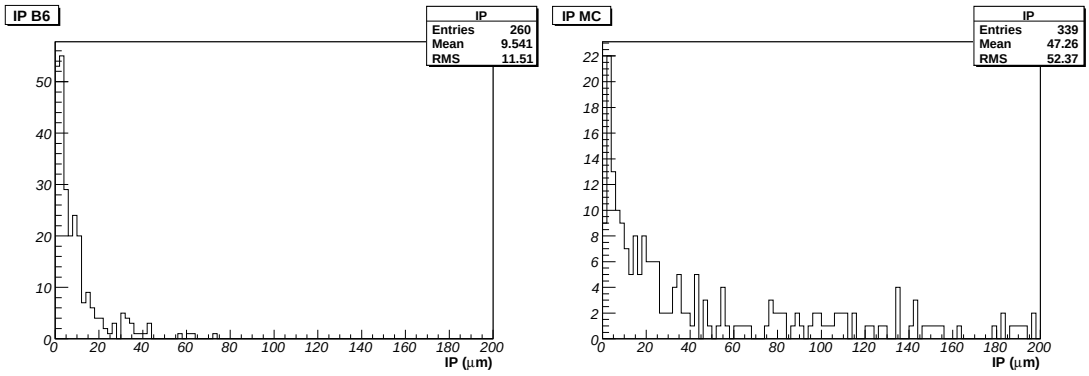


Figure 7.4: Impact Parameter of tracks attached to a vertex in the 8 GeV pion data (left) and a Geant4 simulation reconstructed with ORFEO (right)

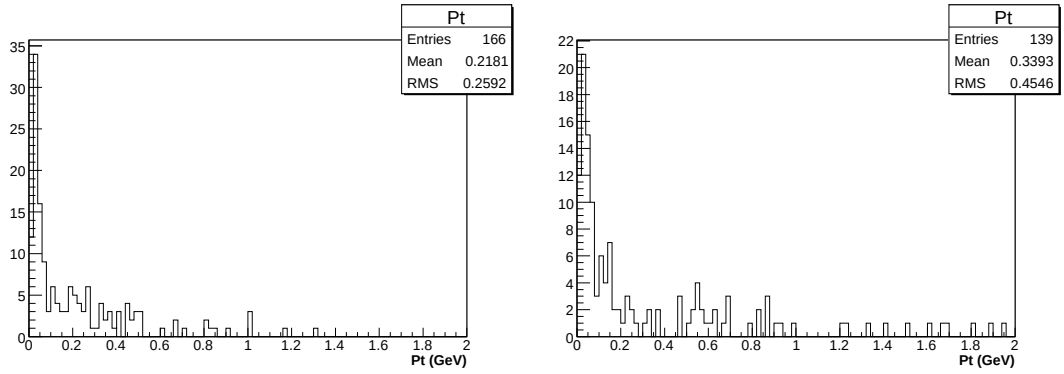


Figure 7.5: Missing Transverse Momenta of reconstructed vertices in the 8 GeV pion data (left) and Geant4 simulation (right)

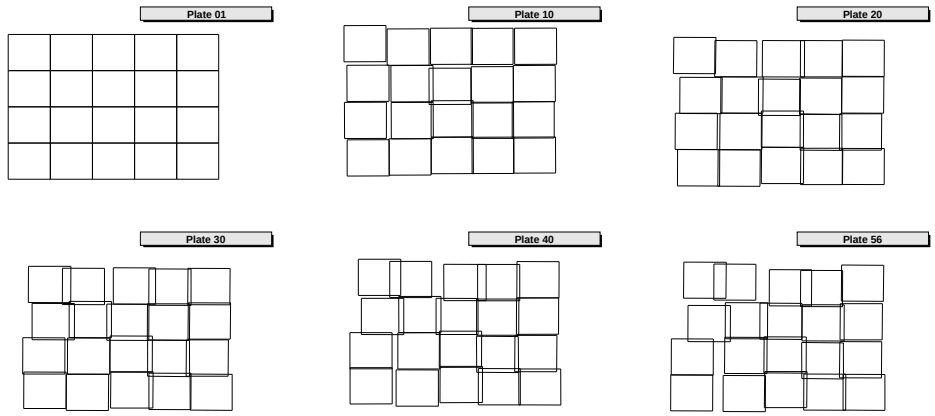


Figure 7.6: 80 $cm^2$ scanned surface aligned by 4 $cm^2$ pieces in the reference frame of the first emulsion sheet. The displacement is magnified 10x compared to the size of the squares.

### 7.2.1 Distortions in the Brick

The first problem encountered during the analysis of the B6 Brick was that a very low number of vertices was found. Apparently aligning the sheets using the whole 80 cm$^2$ scanned surface is not a good choice. Large distortions in the Brick are suspected that could make the alignment of the whole surface impossible within an acceptable error.

To check the idea, I divided the data into 20, 2 cm$\times$2 cm pieces and I applied the alignment procedure with each 4 cm$^2$ surface separately. To visualize the results I draw a grid of 5x4 boxes each one representing a 4 cm$^2$ area of the data and I apply the affine transformations to each one of them.

One can see on Fig. 7.6, the displacement between separately aligned areas on the 56'th plate in the reference frame of the first sheet can be up to 600 $\mu m$. To remedy this problem, I started the alignment in the middle of the Brick in this case I choose the plate number 31, and I aligned the plates in the reference frame of this plate (Fig. 7.7). In this case the maximum (apparent) displacement between the 4 cm$^2$ pieces is only 200 $\mu m$. For further analysis I used this alignment.

The differences in the alignment can be explained with the quality of the Brick assembly. The Bricks prepared for this test-beam, were assembled by hand using the newly developed "spider" technique: the emulsions are hold together by a cage-like structure cut out of an aluminum sheet. The distortions can be caused by the fact that the extremities of the spider are bent with a hammer.

This study shows that the alignment is a very sensitive point of the reconstruction. Doing the alignment with tracks spread over a surface of more than a few cm$^2$ can lead to efficiency problems. It also has consequences for the scan back technique suggesting that the alignment has to be done locally to achieve better results. The observed effect depends strongly on the quality of the Brick. We hope that in the

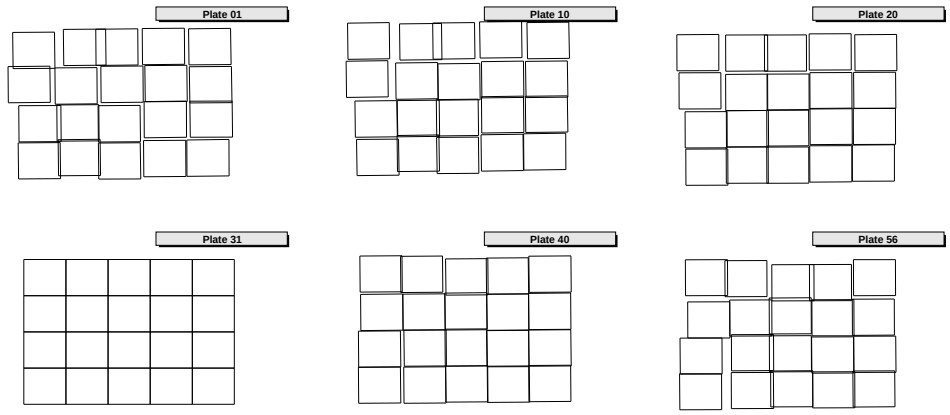


Figure 7.7: 80 cm$^2$ scanned surface aligned by 4 cm$^2$ pieces in the reference frame of the 31'th emulsion sheet. The displacement is magnified 10x compared to the size of the squares.

future we will see only small distortions in the Bricks assembled with the BAM (Brick Assembly Machine).

### 7.2.2 Search for neutrals

In the interactions we see in the Brick there are many neutral particles produced. These particles mainly escape from the Brick, but some of them will interact and will produce secondary interactions. The neutrals are mainly neutrons, gammas and shortlived particles like $\pi^0$'s or $K^0$'s. If we could attach tracks from a secondary vertex, it would provide us with additional information about the primary interaction.

In the first step I try to find vertices with no incoming tracks ("V" shaped vertices). If this vertices are pointing in the direction of a vertex, we can assume that these are neutrals originating from the primary vertex. On figure 7.8 we can see two events resembling to a secondary interaction. The V's were attached only by geometrical considerations. Detailed analysis and estimation of the combinatorial background remains to be done. To attach gammas to the vertex, the study has to be completed with electron-showers as well.

## 7.3 6 GeV electron test-beam

This test-beam exposure was performed at DESY, Hamburg in July 2004. The Bricks were prepared and developed after the experiment at CERN. The goal of the experiment was to develop an electron identification algorithm, measure the energy deposited in the shower and identify $\gamma$'s if possible. The DESY electron beam was running with different energy settings for the experiment: we used the beam with 1, 3 and 6 GeV

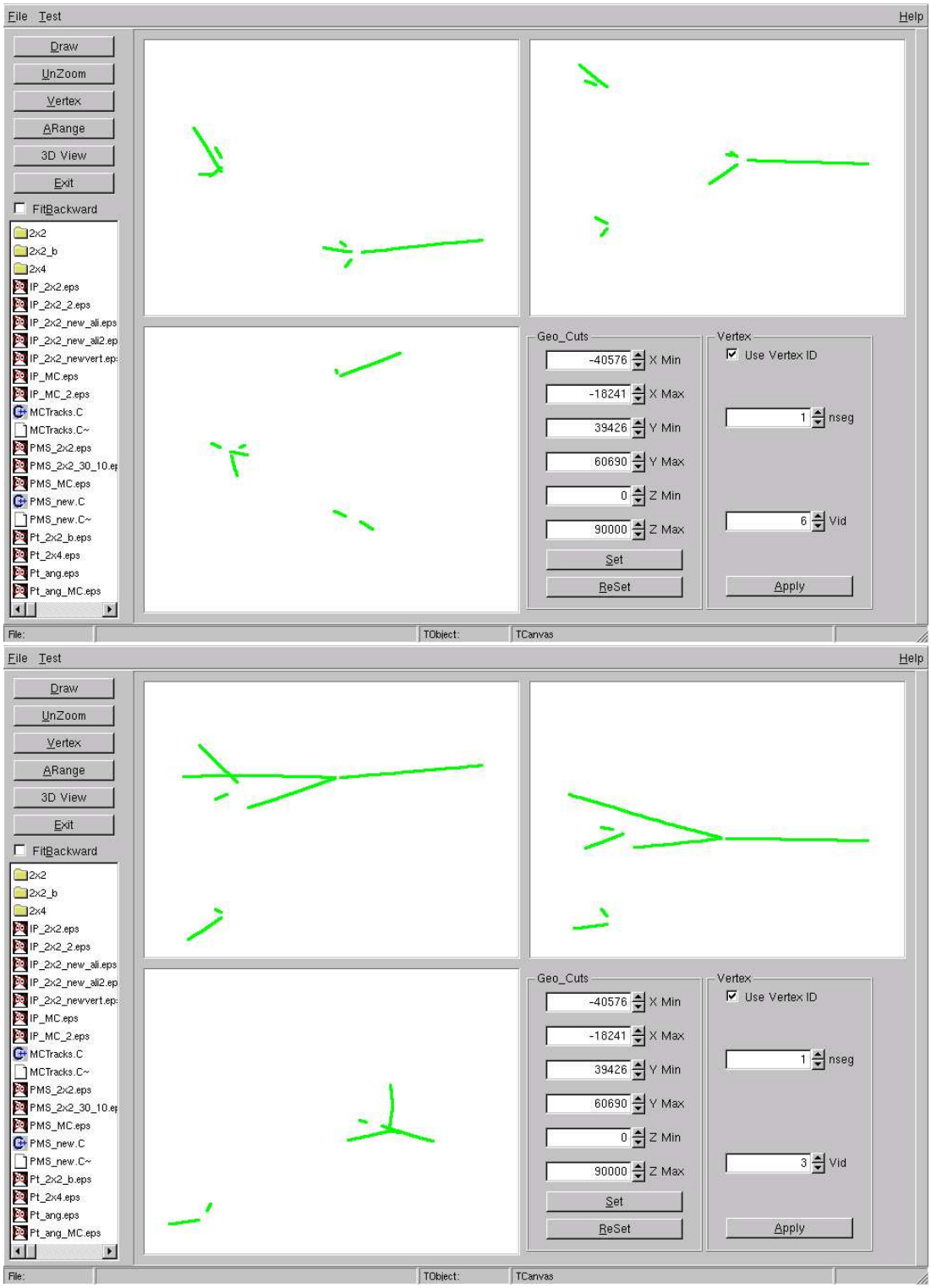


Figure 7.8: Secondary interaction candidates

Figure 7.9: Electron shower. A 6 GeV electron is coming from the left upper corner and inducing a shower. Track reconstruction with FEDRA gives a bunch of interconnected tracks sharing common base-tracks

momentum. Two types of exposures were done: low density 1/cm$^2$ and high density 100/cm$^2$ . The Brick scanned in Neuchâtel contained 20 emulsion sheets and was exposed to the high intensity beam. The beam had a spot diameter of 1.4 cm. The Brick was exposed 12 times, by shifting it horizontally and vertically a few centimeters each time. This way we have 12 beam-spots in the Brick. Their distribution is shown in table 7.2.

| Y/X | -46 mm | -15 mm | 15 mm | 46 mm |
|---|---|---|---|---|
| 34 mm | 440 | 394 | 373 | 422 |
| 0 mm | 416 | 420 | 441 | 390 |
| -34 mm | 355 | 412 | 349 | 404 |

Table 7.2: beam-spots

For cosmic ray exposure the bricks were left in horizontal position for 24 hours. This, and the fact that they were developed one month later, is a source of the very high background level observed during the scanning.

In Neuchâtel we scanned a 10 cm$^2$ surface of the Brick which includes two beam-spots. In the beam-spots we can easily identify the electromagnetic showers by eye. One example is given on Fig. 7.9, the shower in the reconstruction appears as a bunch of interconnected tracks.

In the attempt to find the electrons, first we reconstruct the tracks with FEDRA in the usual way. The beam direction known, I select tracks starting in the first emulsion

sheet in the beam direction with an acceptance of 200 mrad. Then we look how many tracks start in a 200x200 micron parallelepipedon around the incoming track. Asking at least for 5 tracks to start inside the volume, 359 were found from the expected 441 (539 tracks in the beam direction), for the other beam-spot 265 were found and 390 expected (390 tracks in the beam direction). Asking for 3 tracks only 397 were found with 471 tracks pointing in the beam direction (441 expected).

We can conclude that electrons can be identified with 90% efficiency (at 6 GeV) even without additional information ($\frac{dE}{dx}$ for example). From simulation with reconstruction I achieved 97%, without simulating the background.

## 7.4 Neutrino test-beam (PEANUT)

The Neuchâtel and Bern groups were actively involved in this test-beam performed at Fermilab, Chicago, US. A detailed description of the experiment is given in [36]. The main goal of the experiment is to have ECC bricks exposed to a neutrino beam before the OPERA experiment starts. Real neutrino events allow us to test scanning strategies, reconstruction and analysis methods necessary to deal with the real OPERA data and to cross-check physics performance estimated with Monte-Carlo.

The experimental setup consist of maximum 64 bricks piled up in 4 mini-walls with Silicon Fiber Trackers in between. The whole setup is placed in the NuMI beam just before the MINOS near detector (see [36]). The setup was prepared by the Nagoya University recycling old Fiber Trackers used in the DONUT detector. Emulsions were transported to Fermilab by plane after being refreshed in the Tono mine. Packing the Bricks and the development were done on the site.

The NuMI beam can run in several configurations. Changing the target and horn configuration the peak of the energy distribution can be shifted towards higher energies. During the test exposure the beam was running in low energy configuration, see Fig. 7.10 With the given beam intensity we expected 4-12 interactions per Brick per day.

For a comparison I made a simulation with the NuMI beam profile plugged in the NEGN neutrino generator. The particles created in the neutrino interaction were propagated with Geant4 in the ECC Brick geometry and the usual reconstruction and vertex finding were done. The results for vertex multiplicity are shown on Fig. 7.11

## 7.5 Momentum measurement in real data

From test-beam exposures we have 4 different datasets good enough to measure momenta: 2 and 4 GeV pions scanned in Naples from the July 2003 test-beam[1], a 6 GeV dataset scanned in Bologna[2] and 8 GeV pions scanned in Bern from the Nov.2004

[1] http://ntslab01.na.infn.it/public/Pions/

[2] http://www.bo.infn.it/opera/RawRoot/

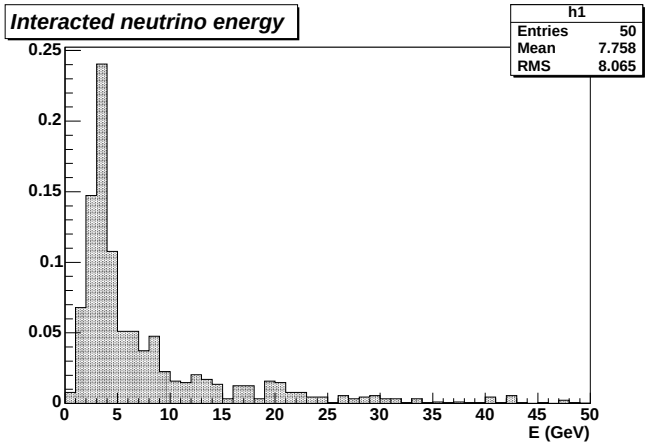


Figure 7.10: Energy distribution of interacted neutrinos coming from the NuMI beam

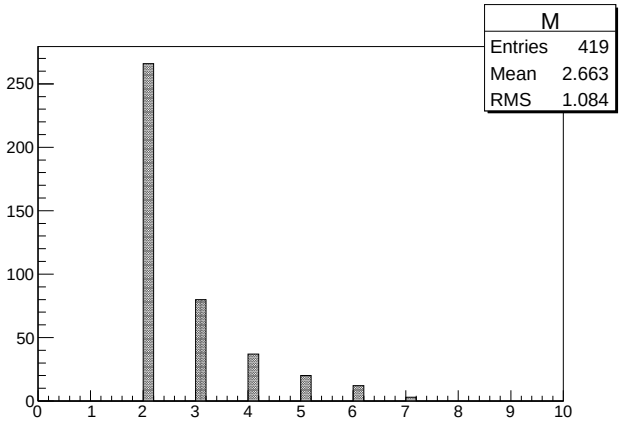


Figure 7.11: vertex multiplicity for $\nu_\mu CC$ simulated events

test-beam[3]. To avoid contamination from the background-tracks, for all these measurements I select only beam-tracks with at least 40 segments. For the momentum measurement we use the $ncell$ method described in Sec. 4.3 with the maximum number of lead-plates crossed: $ncell = 18$.

For the first try, I applied the method described in Sec. 4.3 with fixed measurement error. The results can be seen on Fig. 7.12. Since the distribution $\frac{1}{P}$ is Gaussian, the histogram showing the momentum distribution is fitted with

$$\frac{p0}{P^2} \exp\left( -\frac{\left(\frac{1}{P} - \frac{1}{p1}\right)^2}{(p2)^2} \right)$$

where $p0, p1$ and $p2$ are the fit parameters. The results show an acceptable resolution, in agreement with the simulation. Unfortunately above 4 GeV we see a strong bias, the mean of the momentum is very much underestimated at 6 and at 8 GeV. Apparently, the effect shown on Fig. 4.6 in real data is more accentuated and it happens at lower momentum values.

From Sec. 4.3, we already know that the fit with two free parameters gives a better estimate if we look only the mean value of the momentum distribution. Applied to real data, the results are shown on Fig. 7.13. We observe that the mean value obtained for the 6 GeV data is closer to the real value, but in the case of the 8 GeV data the mean momentum is still too much underestimated. We also notice that the resolutions are worst, in agreement with Fig. 4.6.

In order to understand the reason why the momentum is so much underestimated I made additional studies on the real data. For this, I plotted the angle difference of base-tracks separated by 1,2 ... 18 lead plates, like in the ncell method but here is done for the whole sample. The histogram I fitted with a Gaussian. The width of the distribution as a function of lead plates crossed is shown on Fig. 7.14.

The results can be used for momentum measurement like in the ideal case (infinitely long track or average over many tracks). Fitting with formula 4.2 the mean value of the momenta of all tracks can be obtained. To obtained "momentum" is in good agreement with the mean of the momentum measured one-by-one for the 2 and 4 GeV data. For the 6 and 8GeV data clearly shows that we are above the maximal momentum that can be measured by this method. From the fitted values we can conclude that the maximal momentum that can be measured experimentally: $P_{max} < 6$ GeV.

If formula 4.2 holds ($\delta\theta^2_{diff} = \delta\theta^2_{MCS} + 2\delta\theta^2_m$), we can simply subtract the effect of the MCS and we are left with the measurement error only. Unfortunately subtracting $\delta\theta^2_{MCS}$ do not give a flat distribution. We assume that the measurement error is independent of the position. At 8 GeV is even worse, as we can see on Fig. 7.15 that after the effect of MCS subtracted the "measurement error" is almost always bigger than the effect of MCS. This means that we are trying to measure an effect that is smaller

[3]http://lheppc46.unibe.ch/MICROSCOPE2/B6_AUTO_LARGE/

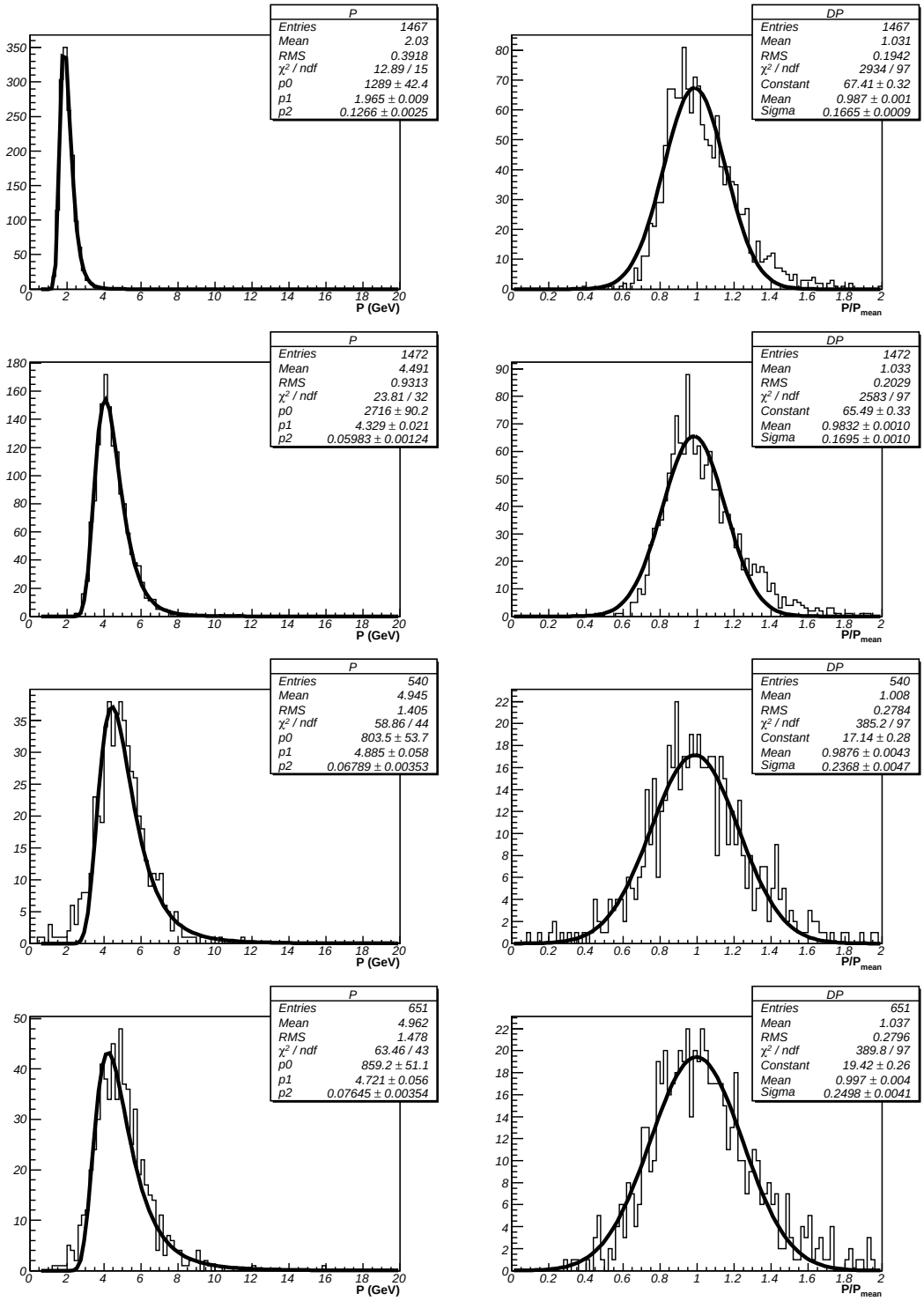


Figure 7.12: Momentum measurement with the ncell method with fixed measurement error ($2\delta\theta^2 = 5$). From top to bottom: 2,4,6 and 8 GeV data

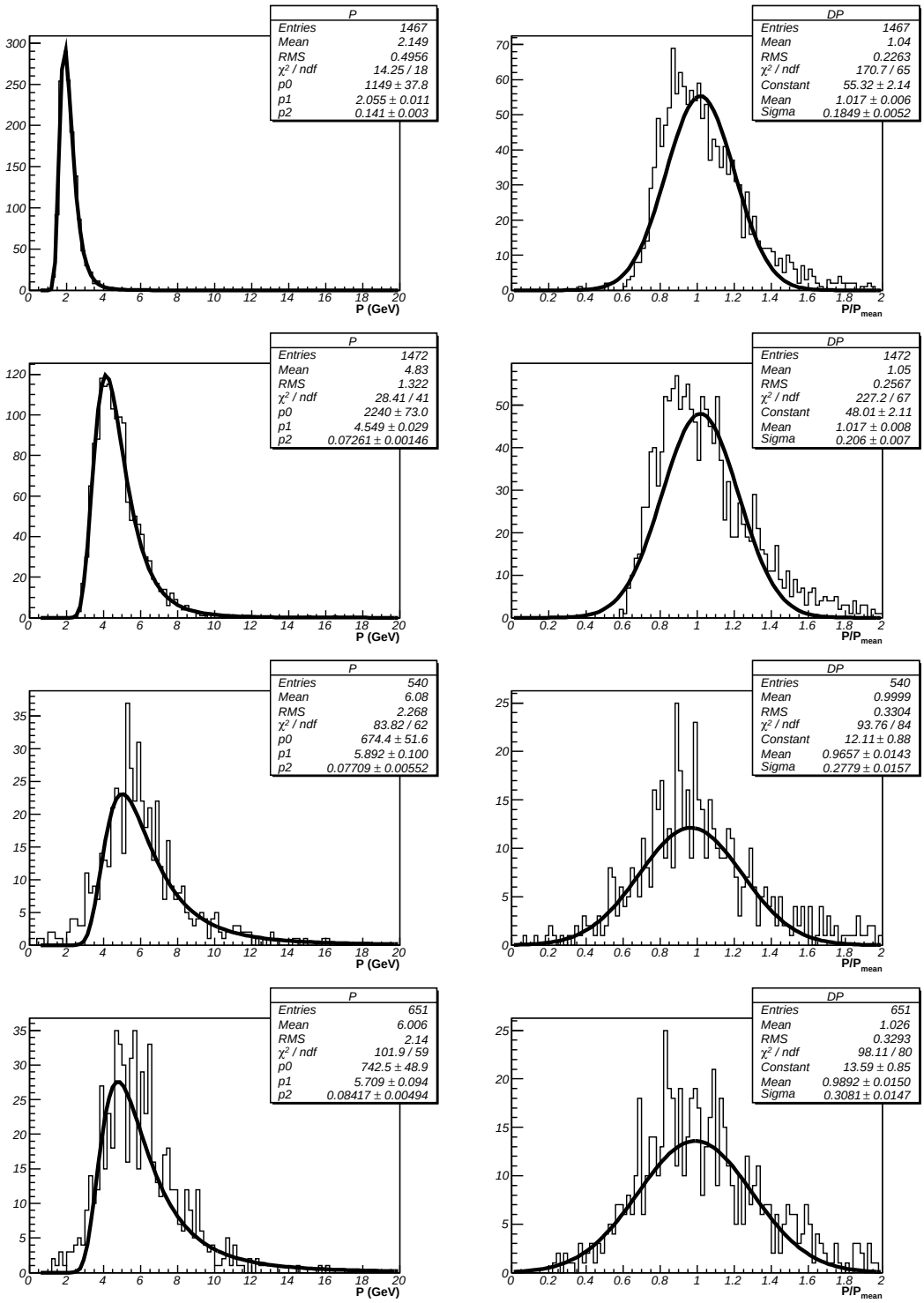


Figure 7.13: Momentum measurement with the ncell method with the measurement error as a free parameter. From top to bottom: 2,4,6 and 8 GeV data.

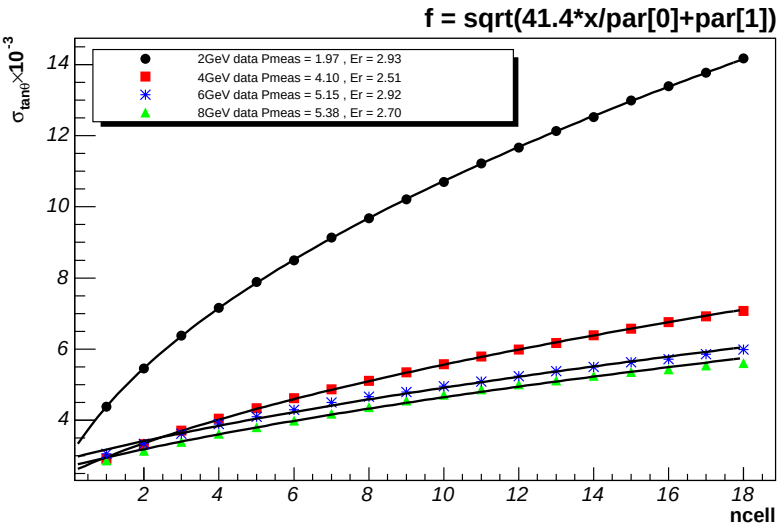


Figure 7.14: Width of the basetrack-angle difference distribution in function of the lead plates crossed. It can be considered as an average track for momentum measurement.

than the error. What is shown on Fig. 7.15 is an avarage over all the tracks. Individual measurements are worsened by the statistical fluctuation, in addition.

To explain the behavior of the measurement error I found two plausible explanations:

1. The validity of the formula $\frac{13.6\,MeV}{\beta cp}\sqrt{\frac{x}{X_0}}$ is limited to small angle scattering which also means high momenta. I was surprised to see the same behavior in data simulated with Geant4 until I found out that Geant4 uses the Lewis formalism instead of the Moliere theory to describe MCS. The subtraction of MCS calculated with $\frac{13.6}{P}\left(\frac{x}{X_0}\right)^{0.555}$ already gives smaller measurement error. The disagreement between the simple approximation and the complete Lewis theory will be bigger as the probability of large angle scattering is higher, at low energy. This can explain what we see in the case of the 2 GeV data.

2. The effect of systematic errors: the mean value of the angular error distribution for the four opposite corners of the Brick and the average for the whole surface is shown on Fig. 7.16. This is in full agreement with the distortions mentioned in section 6.2.1. Clearly if we measure the momentum of a track far from the center of the Brick, our resolution will be worsened by a possible systematic error, which unfortunately behaves in the same way as the “error” caused by the multiple scattering. The systematic errors will never cancel out because we sum up the angles quadratically. The amplitude of the systematic error is in agreement with the remnant error at high energies (8 GeV), see Fig. 7.15.

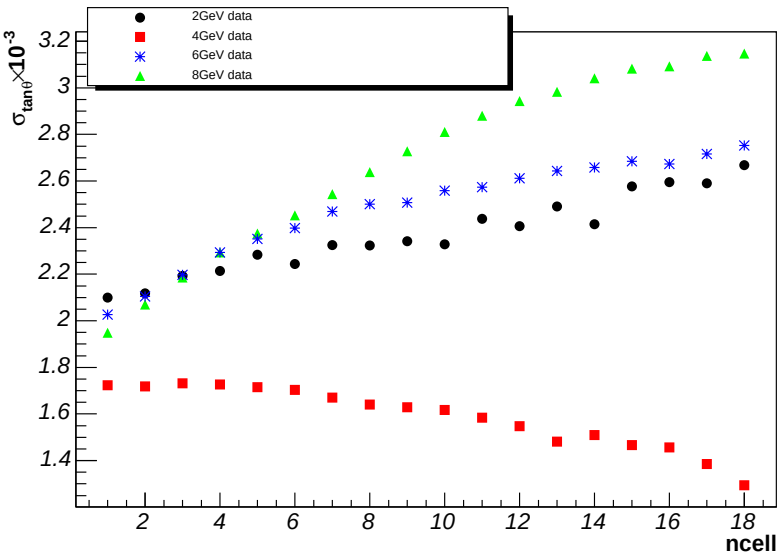


Figure 7.15: Width of the basetrack-angle difference distribution in function of the lead plates crossed with the effect of multiple scattering quadratically subtracted.

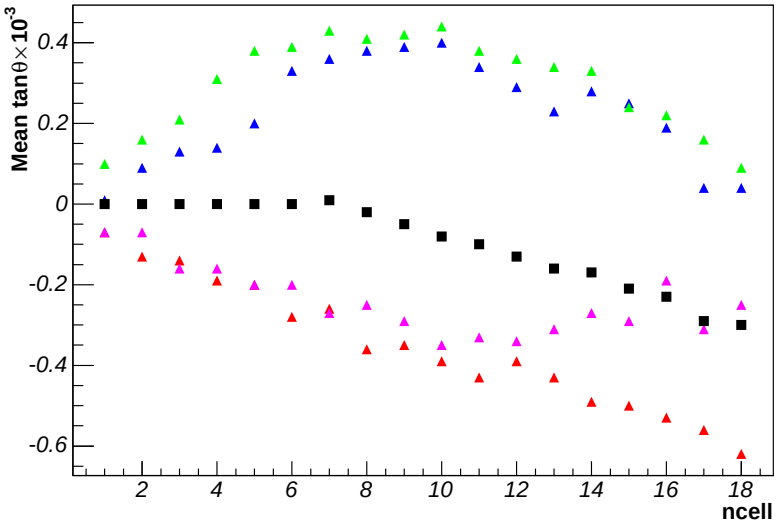


Figure 7.16: Mean of the angle difference distribution in function of plates crossed calculated for the four corners of the Brick using a 16 $cm^2$ surface and in the middle with black squares using the whole surface.

The remaining error, after the subtraction of the effect of multiple scattering has a different amplitude at different momentum. Another explanation would be the angular dependence of the measurement error. As mentioned in section 4.2, the measurement error is angle dependent and the mean scattering angle depends on the momentum, $\delta\theta \sim \delta\theta\left(\frac{1}{P}\sqrt{\frac{x}{X_0}}\right)$. For example at 2 GeV after 10 plates crossed the width of the Moliere distribution is 10 mrad. This fact gave the idea to try out a new method that preserves the momentum dependence of the measurement error.

Similar to reference [53] we can write the negative log likelihood function

$$\mathcal{L} = \frac{1}{2}\log\left(\det \mathbf{V}(P)\right) + \frac{1}{2}\chi^2(\theta_0, y_0, P)$$

were $\chi^2$ is originally the standard $\chi^2 = (\vec{y} - \theta_0\vec{z}_1 - y_0\vec{z}_0)\mathbf{V}^{-1}(P)(\vec{y} - \theta_0\vec{z}_1 - y_0\vec{z}_0)$ with $\theta_0$ the slope $\vec{y}$ and $\vec{z}_1$ the $N$ measured $y$, $z$ points, and $\vec{z}_0$ is an $N$ dimensional unit vector. $\mathbf{V}(P)$ is the momentum dependent covariance matrix. The $ncell$ method practically consist in replacing the $\chi^2$ function with

$$\sum_{i=0}^{N} \frac{\left(\theta^2_{meas,i} - \left(\frac{(13.6)^2 x_i}{P^2 X_0} + 2\delta\theta_0^2\right)\right)^2}{\sigma_i^2(x_i)}$$

were I denoted with $x_i$ the number of lead plates crossed in $i$th step. Minimizing this function is equivalent to the graphical fit method.

The main difference between the position and the angular method is that the scattering angle does not depend on the scattering angle in the previous step. Therefore, we can assume that the covariance matrix is diagonal and we can write the logarithmic term as:

$$\sum_{i=0}^{N} \sigma_i(x_i, P)$$

The main difficulty is finding a good formula for $\sigma_i$. Observing that the angular error in function of the angle can be fitted with a second order polynomial (see Fig. 4.3), $\sigma = 1.7 + \frac{C_1}{P^2}$ seems a reasonable approximation, where $1.7$ is the angular error at $0$ angle, $C_1$ and $P$ are fit parameters. Other formulas that preserve the $x_i$ dependence of the error did not gave better results. Finally the following formula for $\mathcal{L}$ was used:

$$\mathcal{L} = \sum_{i=1}^{N} \log(\sigma_i) + \sum_{i=1}^{N} \left( \frac{\theta_{meas,i} - \frac{13.6}{P}\sqrt{\frac{x_i}{X_0}}}{\sigma_i} \right)^2$$

After minimizing the function $\mathcal{L}$ the obtained momentum distribution is shown on Fig. 7.17.

The obtained resolution at 2 GeV is surprisingly good. It is comparable with the one obtained with simulated tracks without smearing. Until now the best published

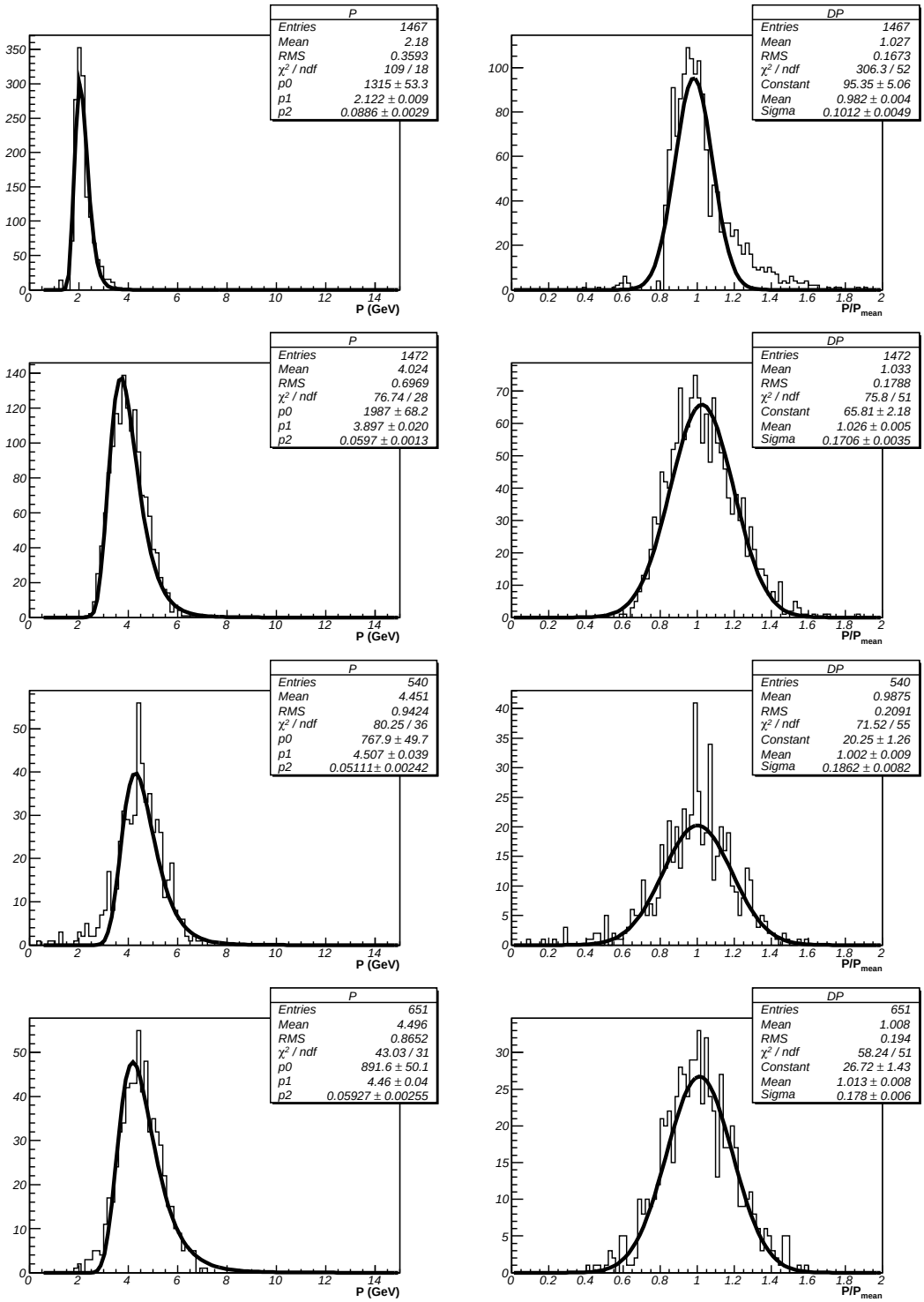


Figure 7.17: log likelihood method. From top to bottom: 2,4,6 and 8 GeV data.

results with real data showed about a 30% resolution. Interestingly, if the minimization converges the fit-parameter $C_1$ is almost zero. It means that the momentum dependence of the error was removed. Like every method this one also has it's draw back: the mean of measured distribution is strongly biased towards lower momenta. As we can see on Fig. 7.17 a 4GeV track is measured with a mean of 4 GeV but an 8 GeV track is measured only at 4.4-4.5 GeV. Apparently, with this method we can not exceed the limit when the measurement error and the effect of Multiple Scattering becomes equal, which happens around 4 GeV.

The methods presented above should not be considered as a final solution for the problem of the Momentum Measurement. For a practical solution one could choose the method with two free parameters (for minimum bias) and if the measured momentum is below 4 GeV redoing the fit with the log-likelihood method one could take advantage of minimum bias and good resolution in the same time.

Since for the kinematical analysis we assumed that the momentum measurement works up to 15 GeV, further studies have to be done to fully understand the behavior of the real data.

# Chapter 8

# Conclusions

The OPERA experiment starts taking data the summer of this year (2006), only a few month after finishing up this document. We expect to be able to scan and analyze the large amount of ECC Bricks extracted from the detector. While until the final analysis is a long way to go, most of the tools are already given and will be up to the next generation of Ph.D. students to use them at their full potential.

In this study we estimated the background originating from hadron re-interactions in the ECC Brick. The total background rate for the five year run of the OPERA experiment, after the suggested kinematical cuts, is estimated at 0.1 or below for each of the $\tau \rightarrow \mu + \nu_\mu + \nu_\tau$, $\tau \rightarrow \pi + \nu_\tau$ and $\tau \rightarrow \pi + n\pi^0 + \nu_\tau$ channels. The background for the $\tau \rightarrow \pi + n\pi^0 + \nu_\tau$ is estimated for the first time here. The results are consistent with another simulation done with FLUKA. This study is important for demonstrating that OPERA is a very low background experiment and the total number of background events will be below one for the five year run.

The detection efficiency for all $\tau$ decay channels of the OPERA detector is currently estimated at 9%. Hence a small gain in detection efficiency would be considered as a major improvement. Based on a Geant4 simulation, here we estimated the detection efficiency of the decay channels with one charged pion ($\tau^- \rightarrow \pi^- + (n\pi^0) + \nu_\tau$, $n = 0, 1, 2$). We exploited the possibility to identify the decay channels with neutral pions by attaching $\gamma$'s to the secondary vertex. The found overall efficiencies are $\varepsilon_\tau = 2.82$**%** for DIS and $\varepsilon_\tau = 2.99$**%** for QE interactions. These numbers are consistent with the ones published in [33].

Showing our results with data coming from test-beam exposures, we proved that we will be able to analize the data when the experiment starts. The number of pion interactions found in the November 2004 test-beam data is compatible with the number of interactions in simulated events. In general, the real-data and the simulated one shows a good agreement. A preliminary kinematical analysis shows the feasibility of using cuts on the transverse momentum and the impact parameter.

Studies of the momentum measurement showed much better resolution than ever published before [56]. We demonstrated that resolution below 20% is possible to achieve, up to 4 GeV momentum. With an alternative method we achieved resolu-

tion better than 15% at low momentum (2 GeV). Unfortunately we observed strong limitations in the maximal measurable momentum, not observed in Monte Carlo data. These studies has to be continued in order to fulfill the requirements of the kinematical analysis.

All this proves that tracking and vertex-finding methods are in the final stage of development, their application to neutrino events will be straight forward.

# Acknowledgment

I would like to express my gratitude to prof. Jean-Luc Vuilleumier for the opportunity to work in his group in Neuchâtel. Without his generosity and his confidence it would have been difficult to start a carrier in particle physics.

I would also like to thank my senior colleagues Frederic Juget and Markus Hauger for guiding me in my studies in neutrino physics, field completely unknown for me before. For creating a pleasant working enviroment I am greatfull to all other members of the group: Eric Baussan, Jose Busto, Zornitza Daraktchieva, Gordana Gerber, Leila Ounalli, Dominique Schenker, Damian Twerenbold, Jean-Michel Vuilleumier, Patrick Weber.

This work could not have been completed without the help of the members of the High Energy Physics group in Bern leaded by prof. Klaus Pretzl and later by prof. Antonio Ereditato. Much of the data used was provided by Igor Kreslo. Many thanks to Urs Moser, Nikolay Savvinov and Thomas Wälchli as well.

# Bibliography


[1] Winter Klaus, Neutrino Physics, Cambridge University Press, 1991

[2] Hughes I.S., Elementary Particles, Cambridge University Press, 1991

[3] Ryder L.H., Quantum Field Theory, Cambridge University Press, 1996

[4] Giunti C. Neutrino Mixing, arXiv:hep-ph/0310238, 2004

[5] Brunner J. Experimental Results on Neutrino Masses and Lepton Mixing, CERN-PPE/97-38, 1997

[6] Boehm F., Vogel P. Physics of Massive Neutrinos, Cambrige University Press, 1987

[7] Klapdor H.V. Neutrinos, Springer 1988

[8] Waltham C. Neutrino Oscillation for Dummies, arXiv:physics/0303116 2003

[9] Particle Data Group, Review of Particle Physics, Phys. Rev. D 66, 2002

[10] Wolfenstein L., Neutrino oscillations in matter, Phys. Rev. D 17, 1978

[11] Reines F., Cowan C.L., Detection of the Free Neutrino, Phys. Rev. 92, 1953

[12] Davis R., Solar Neutrinos. II. Experimental, Phys. Rev. Lett. 12, 1964

[13] Kodama K. et al., Observation of tau neutrino interactions, Phys. Lett. B 504, 2001

[14] Kodama K. et al., Detection and analysis of tau-neutrino interactions in DONUT emulsion target, N.I.M. A 493, 2002

[15] Shigeki Aoki, Tracking and vertex reconstruction in modern emulsion experiments, N.I.M. A 473, 2001

[16] Apollonio M. et al., Search for neutrino oscillations on a long base-line at the CHOOZ nuclear power station, Eur.Phys.J. C27, 2003

[17] Anselmann P. et al., Solar neutrinos observed by GALLEX at Gran Sasso, Phys. Lett. B285, 1992

[18] Fukuda, Y. et al., Atmospheric muon-neutrino / electron-neutrino ratio in the multiGeV energy range, Phys. Lett. B335, 1994

[19] Hosaka J. et al., Solar neutrino measurements in Super-Kamiokande-I, arXiv:hep-ex/0508053

[20] Ashie Y. et al., A Measurement of Atmospheric Neutrino Oscillation Parameters by Super-Kamiokande I, Phys. Rev. D71, 2005

[21] Fukuda Y. et al. (Super-Kamiokande), Evidence for oscillation of atmospheric neutrinos, Phys. Rev. Lett. 81 (1998) 1562-1567, hep-ex/9807003

[22] Berger Ch. et al., A Study of atmospheric neutrino oscillations in the Frejus experiment, Phys. Lett. B245, 1990

[23] Aglietta, M. et al., Experimental study of atmospheric neutrino flux in the NUSEX experiment, Europhys. Lett. 8, 1989

[24] Becker-Szendy R. et al., Search for muon neutrino oscillations with the Irvine-Michigan-Brookhaven detector, Phys. Rev. Lett. 69, 1992

[25] Anthony Mann W, New results on atmospheric neutrinos from Soudan 2, Nucl. Phys. Proc. Suppl. 91, 2000

[26] Ahmad Q.R. et al. (SNO Collaboration), Direct Evidence for Neutrino Flavor Transformation from Neutral-Current Interactions in the Sudbury Neutrino Observatory arXiv:nucl-ex/0204008, 2002

[27] Aharmim B. et al. (SNO Collaboration), Electron Energy Spectra, Fluxes, and Day-Night Asymmetries of $^8B$ Solar Neutrinos from the 391-Day Salt Phase SNO Data Set, arXiv:nucl-ex/0502021, 2005

[28] Eguchi K. et al. (The KamLAND Collaboration), First Results from KamLAND: Evidence for Reactor Anti-Neutrino Disapperarance, arXiv:hep-ex/0212021, 2002

[29] Araki T. et. al. (The KamLAND Collaboration), Measurement of Neutrino Oscillation with KamLAND: Evidence of Spectral Distortion, arXiv:hep-ex/0406035, 2004

[30] Klapdor-Kleingrothaus H.V. et al. Search For Neutrinoless Double Beta Decay With Enriched $^{76}$Ge 1990-2003 HEIDELBERG-MOSCOW Experiment arXiv:hep-ph/0404062, 2004

[31] Lattanzi M. et al., Joint constrains on the lepton asymmetry of the Universe and neutrino mass from the Wilkinson Microwave Anisotropy Probe, arXiv:astro-ph/0509079, 2005

[32] OPERA Proposal CERN/SPSC 2000-028, 2000

[33] Status Report on the OPERA Experiment CERN/SPSC 2001-025, 2001

[34] Kodama K. et al., The OPERA $\nu_\tau$ appearance experiment in the CERN-Gran Sasso neutrino beam, CERN/SPSC 98-25, 1998

[35] Komatsu M., Migliozzi P., Terranova F., Sensitivity to $\theta_{13}$ of the CERN to Gran Sasso neutrino beam, J. Phys. G: Nucl. Part. Phys. 29, 2003

[36] Kodama K. et al, Request for a Test Exposure of OPERA Targets in the NuMI Beam, 2004

[37] Taku Nakamura et al., The OPERA film: New nuclear emulsion for large-scale, high-precision experiments, N.I.M. A 556, 2006

[38] Armenise N. et al., High-speed particle tracking in nuclear emulsion by last-generation automatic microscopes, N.I.M. A 551, 2005

[39] Dracos M. et al., Plastic Scintillator Target Tracker Proposal (Baseline) and Studies done at Strasbourg, OPERA Internal Report, 2001

[40] Baldanza C. et al., The Bologna Emulsion Scanning Laboratory 2004 Report, OPERA Internal Report, 2004

[41] Damet J. et al., Status of the emulsion scanning station in Bern, OPERA Internal Report, 2003

[42] http://geant4.web.cern.ch/geant4/

[43] http://root.cern.ch/

[44] FEDRA homepage: http://ntslab01.na.infn.it/fedra/

[45] Tioukov V. et al., The FEDRA - Framework for emulsion data reconstruction and analysis in the OPERA experiment N.I.M. A 559, 2006

[46] Glebe Th., VT++ version 1.0, Hera-B Note 00-175, 2000

[47] ORFEO homepage: http://web.na.infn.it/index.php?id=527

[48] Autiero D., The OPERA event generator and the data tuning of nuclear reinteractions, Nucl. Phys. B. Proc. Suppl. 139, 2005

[49] Billoir P., Track Fitting with Multiple Scattering: A new Method, N.I.M. 225, 1984

[50] Billoir P., Frühwirth R., Regler M., Track Element Merging Strategy and Vertex Fitting in Complex Modular Detectors, N.I.M. A241, 1985

[51] Frühwirth R., Application of Kalman filtering to track and vertex fitting, N.I.M. A262, 1987

[52] Mankel R., Application of the Kalman Filter Technique in the HERA-B Track Reconstruction, HERA Note 95-239, 1995

[53] Bolton T., High Energy Muon Momentum Estimation from Multiple Coulomb Scattering in Dense Detectors, arXiv:hep-ex/9705007v1

[54] Duchesneau D., Lavy M., Study of momentum measurements with multiple Coulomb scattering (angle method), OPLAPP-1812-01, 2001

[55] Duchesneau D., Lavy M., Update of momentum measurements with multiple Coulomb scattering (angle method), OPLAPP-0412-02, 2002

[56] De Serio M. et al., Momentum measurement by the angular method in the Emulsion Cloud Chamber, N.I.M. A 512, 2003

[57] Lewis H.W., Multiple Scattering in an Infinite Medium, Phys. Rev. 78, 1950

[58] Bethe H.A., Molière Theory of Multiple Scattering, Phys. Rev. 89, 1953

[59] Juget F., Hauger M., Janicsko J., Detection Efficiency for Hadronic Channels and Background Estimation for Hadronic Reinteractions, Internal Report, 2003

[60] Study of electron identification in the Emulsion Cloud Chambers of the OPERA experiment, L.S. Esposito, thesis, Bologna 2005